Aalto University
School of Electrical
Engineering

Henry Lähteenmäki

Detection of Defects in Glass Fiber Reinforced Plastic by NDT Techniques

Master's Thesis
Espoo, November 9, 2015

Supervisor: Professor Harri Lipsanen
Instructor: Valtteri Myllymaa, MSc.Tech.

AALTO UNIVERSITY
SCHOOL OF ELECTRICAL ENGINEERING
http://www.aalto.fi

MASTER'S THESIS
ABSTRACT

Author:	Henry Lähteenmäki		
Title:	Detection of Defects in Glass Fiber Reinforced Plastic by NDT Techniques		
University:	Aalto University School of Electrical Engineering		
Degree Programme:	Electronics and Electrical Engineering		
Major:	Electrophysics	**Major code:**	S3014
Supervisor:	Professor Harri Lipsanen		
Instructor:	Valtteri Myllymaa, MSc.Tech.		

Composites are the most promising alternatives for replacing metals mainly due to their advanced structural properties. Visual, infrared thermographic, zero interface probe ultrasonic, phased array ultrasonic and digital radiographic testing are studied for NDT of glass fiber reinforced plastic. Test plates and pipes were made of E-glass and their matrix was vinyl ester. The theory part of this work introduces physical principles of used NDT techniques and the composition and typical defects of glass fiber reinforced plastic. The theory of NDT for glass fiber reinforced plastics recess the techniques used in this work.

The goal was to establish the compination of NDT techniques in order to make reproduciple, reliable and comprehensive inspections for glass fiber reinforced plastic. The advantages and disadvantages of the used NDT techniques are also discussed. Empirical research revealed that infrared thermography suits to localize and differ delamination and wall loss. Major cracks can also be detected. Zero interface probe ultrasonic testing may be used to quantify delamination and wall loss even for thick GRP product. Phased array ultrasonic testing suits for visualization and easier analyzation of test data. Digital radiography may be used to expose small defects and the severity of the delamination. Also accurate thickness measurements can be done. Visual testing can reveal many defect types and it should be included to every testing procedure.

Date:	November 9, 2015	**Number of pages:**	10 + 126
Language:	English		
Key words:	NDT, visual testing, zero interface probe, infrared thermography, phased array ultrasonic testing, digital radiographic testing, composites, glass fiber reinforced plastic		

AALTO-YLIOPISTO
SÄHKÖTEKNIIKAN KORKEAKOULU
http://www.aalto.fi

DIPLOMITYÖ
TIIVISTELMÄ

Tekijä:	Henry Lähteenmäki
Työn nimi:	Vikojen havaitseminen lasikuitulujitetusta muovista NDT-menetelmillä
Korkeakoulu:	Aalto-yliopisto Sähkötekniikan korkeakoulu
Tutkinto-ohjelma:	Elektroniikka ja sähkötekniikka
Pääaine:	Sähköfysiikka **Pääaineen koodi:** S3014
Valvoja:	Professori Harri Lipsanen
Ohjaaja:	DI Valtteri Myllymaa

Komposiitit ovat lupaavimpia vaihtoehtoja metallien korvaajiksi kehittyneiden rakenteellisten ominaisuuksien takia. Silmämääräis-, infrapunatermografia-, rajapinnattoman luotaimen ultraääni-, vaiheistettua ultraääni- ja digitaalista radiografitarkastusta tutkittiin lasikuitulujitetun muovin NDT-tarkastuksessa. Koekappaleet olivat E-lasikuitutyyppiä ja matriisi oli viinyliesteri. Teoriaosassa esitellään käytettyjen NDT-menetelmien fysikaaliset perusteet sekä lasikuitulujitetun muovin rakenne ja tyypilliset viat. Lasikuitulujitetun muovin NDT-tarkastuksien teoriassa syvennytään tässä työssä käytettyihin menetelmiin. Tavoite oli selvittää NDT-tekniikoiden yhdistelmä, jolla laskikuitulujitettua muovia voidaan tarkastaa toistettavasti, luotettavasti ja kattavasti. Käytettyjen NDT-menetelmien heikkouksia ja vahvuuksia pyrittiin myös selvittämään.

Tutkimustyössä selvisi, että infrapunatermografia sopii delaminaation ja oheneman paikantamiseen ja erottamiseen toisistaan. Suuret halkeamat voitiin myös havaita. Rajapinnattoman luotaimen ultraäänitarkastusta havaittiin delaminaatio, iskuvaurio ja ohenema. Vaiheistettu ultraäänitarkastus sopii tarkastusdatan visualisointiin ja analysointiin. Digitaalisella radiografialla voidaan tehdä tarkkoja paksuusmittauksia. Lisäksi se paljastaa pieniä vikoja sekä delaminaation vakavuuden. Silmämääräinen tarkastus paljastaa monia vikatyyppejä ja se tulisikin sisällyttää jokaisen NDT tarkastuksen yhteyteen.

Päivämäärä:	9. marraskuuta 2015	**Sivumäärä:**	10 + 126
Kieli:	Englanti		
Avainsanat:	NDT, visuaalinen tarkastus, ZIP-tarkastus, infrapunatermografia, vaiheistettu ultraäänitarkastus, digitaalinen radiografia, komposiittirakenne, lasikuitulujitettu muovi		

Preface

First and foremost, I would like to thank Inspecta Oy for the opportunity to write my Master's Thesis for them. Inspecta offered me an excellent research environment to perform empirical research and deepen my knowledge on nondestructive testing for composites. I am grateful to my manager Mr. Jouni Koivumäki for assigning me such a interesting and intriguing research subject. I would like to thank my Master's Thesis supervisor Professor Harri Lipsanen expertise guidance during this work. My sincere thanks go to my instructor Mr. Valtteri Myllymaa, MSc.Tech. for being always open to discussion and ideas.

The experimental results were obtained in close collaboration with my collegues Mr. Ari Kaarnalehto, Mr. Ari Takkunen, Mr. Erkki Sallinen and Mr. Petri Reiman. I am grateful for their excellent guidance to the practical aspects of testing glass fibre reinforced plastic with NDT techniques.

Finally, I wish to express my profound gratitude for my family and Alejandra. Without you this would not have been possible.

Espoo, November 9, 2015

Henry Lähteenmäki

Contents

Nomenclature

Abbreviations

DRT	Digital Radiographic Testing
DT	Destructive Testing
GRP	Glass fiber Reinforced Plastic
IRT	Infrared Thermography
MWT	Microwave Testing
NDT	Nondestructive Testing
PA	Phased Array
PAUT	Phased Array Ultrasonic Testing
PSK	The Processing Industry Standards Association
RT	Radiographic Testing
SFS	The Finnish Standards Association
UT	Ultrasonic Testing
VT	Visual Testing
ZIP	Zero Interface Probe

Symbols

α	Angle of incidence $[^\circ]$
α_I	First critical angle $[^\circ]$
α_II	Second critical angle $[^\circ]$
α_λ	Absorptivity
γ	Angle of refraction $[^\circ]$
$\Delta\mathrm{dB}$	Attenuation $[\mathrm{dB}]$
ΔG	Transmission loss $[\mathrm{dB}]$
ΔR	Reflection loss $[\mathrm{dB}]$
ε	Emissivity
θ	Opening angle $[\mathrm{rad}]$
λ	Wavelength $[\mathrm{m}]$
μ	Linear absorption coefficient $[1/\mathrm{mm}]$
τ_λ	Transmissivity
ρ	Mass density $\left[\mathrm{kg/m^3}\right]$
ϕ_λ	Reflectivity
σ	Stefan-Boltzmann constant $\left[\frac{\mathrm{W}}{\mathrm{m^2K^4}}\right]$
σ_A	Total attenuation coefficient $[1/\mathrm{cm}]$
ω	Angular frequency $[\mathrm{rad/s}]$

A	Area $\left[\mathrm{m}^2\right]$
c	Speed of light $[\mathrm{m/s}]$
d	Wall thickness $[\mathrm{m}]$
D	Probe diameter $[\mathrm{m}]$
e	Elementary charge $[\mathrm{C}]$
E	Spectral irradiance $\left[\mathrm{W/m}^2\right]$
f	Frequency $[\mathrm{Hz}]$
h	Planck's constant $[\mathrm{J \cdot s}]$
h_S	Percent of the signal
H	Heat current $[\mathrm{J/s}]$
I	Intensity $\left[\mathrm{W/m}^2\right]$
$I(\lambda)$	Spectral emittance $\left[\mathrm{W/m}^3\right]$
k	Wavenumber $[1/\mathrm{m}]$
k_c	Thermal conductivity $\left[\frac{\mathrm{W}}{\mathrm{m \cdot K}}\right]$
$k_\square$	Near field correction factor
k_B	Boltzmann's constant $[\mathrm{J/K}]$
L	Lenght $[\mathrm{m}]$
n	Number of atoms per cubic centimeter
N_A	Avogadro's number $[1/\mathrm{mol}]$
p	Pressure of sound $\left[\mathrm{N/m}^2\right]$
$p(x,t)$	Pressure of sound of a wave function $\left[\mathrm{N/m}^2\right]$
$\vec{p}$	Momentum $\left[\mathrm{N/m}^2\right]$
P	Power $[\mathrm{W}]$
Q	Heat $[\mathrm{J}]$
R	Reflection coefficient
t	Time $[\mathrm{s}]$
T	Temperature $[\mathrm{K}]$ or $[^\circ\mathrm{C}]$
$T_{transmission}$	Transmission coefficient
v	Speed of sound $[\mathrm{m/s}]$
x	Displacement $[\mathrm{m}]$
Z	Acoustic impedance $\left[\frac{\mathrm{kg \cdot m}}{\mathrm{m}^3 \cdot \mathrm{s}}\right]$

1 Introduction

Nondestructive testing (NDT) techniques are used to examine and detect the defects of materials. The NDT techniques have typically been used for quality assurance of metal constructions. New, advances composite structures are becoming more and more common in variety of applications mainly due to their advanced structural properties such as lightness, stiffness and durability. The increasing need to inspect anisotropic composites is a major challenge for the traditional NDT. Glass fiber reinforced plastic (GRP) is the most common composite structure and its applications include many critical constructions, for example airframes.

This Master's Thesis describes the NDT procedure and results of visual testing (VT), infrared thermography (IRT), zero interface probe ultrasonic testing (ZIP UT), phased array ultrasonic testing (PAUT) and digital radiographic testing (DRT). Furthermore, optimal testing parameters are studied. The IRT is known to be a good technique for localizing different defects but the type of the defects often remains unknown. The ZIP-UT is used to overcome the loss of energy in the delay line–GRP interface. However, it is inconvenient for large surface areas. The PAUT is considered superior method for defect identification and visualization. However, the loss of energy in the delay line has been a problem before but a solution is proposed in this Master's Thesis. The DRT can be used to detect small defects because its good resolution. Hence, it might be most suitable for the detailed inspection of the critical components.

The results of this work are especially aimed for NDT-inspectors. The inspectors could use the theory and results of this research as a reference when determining and analysing possible defects in the GRP. Qualifications of inspectors are essential. Inspection and interpretation of the results of advanced composites like the GRP requires special skills. The inspectors must know the pros and cons of each NDT technique for in order to make reliable inspections.

The future looks bright for the NDT of composites. Composites and especially the GRP are continuously used more and more. Thus, the need for the NDT is ever increasing. A major part of research is done in the aviation industry but the capabilities of the NDT techniques for other branch of industries are not well known.

Objective of the Work

The objective of the Master's Thesis is to find out the best combination of nondestructive testing techniques used to locate, identify and visualize the defect types both in new and used glass fiber reinforced plastic products. Comparing testing parameters between used and new GRP products is also studied. Finding optimal testing parameters for existing equipments is essential for commercialisation of the NDT

techniques for the GRP.

Overview of the Work

The Master's Thesis is organized as follows. Chapter 2 (see p. 3) introduces the GRP and its defects. Chapters 3 (see p. 10) 4 (see p. 12), 5 (see p. 21), 6 (see p. 40) and 7 (see p. 43) describe the physical principles of the VT, IRT, PAUT, ZIP UT and DRT, respectively. Moreover, the NDT techniques used in this work are discussed from the GRP point of view. Chapter 8 (see p. 53) introduces equipment, test plates, pipes and testing methods. Chapter 9 (see p. 61) explains NDT results. Concluding remarks and perspectives are given in Chapter 10 (see p. 65).

Results are further expanded to image banks that include all inspection images from the actual NDT. The image banks are the most useful part of this Master's Thesis for the inspectors. The image banks can be used as a reference when determining defect types with different NDT techniques. Visual testing image bank is presented in Appendix A (see p. 70). Infrared thermography image bank is shown in Appendix B (see p. 78). Appendix C (see p. 97) contains the visual data of the phased array ultrasonic testing. Zero interface probe ultrasonic testing image bank is presented in Appendix D (see p. 102). Digital radiographic testing image bank is shown in Appendix E (see p. 108). Finally, an overview figures of each studied defect types is presented in Appendix F (see p. 119).

2 Glass Fiber Reinforced Plastic

All dielectrics and composites exhibit different properties. Therefore, the generalization under the terms such as *dielectrics* or *composites* is misleading. The character of the interfacial bond, relative strengths and stiffness of the fiber-matrix combination, environmental conditions and distribution of the fibers vary even among different types of glass fiber reinforced plastics (Harris, 1983). Comprehensive introduction to dielectrics and composites, their NDT testing techniques and especially their microwave testing (MWT) is given in my Special Assignment in Electrophysics -research project (Lähteenmäki, 2015).

Section 2.1 (see p. 3) gives insight into a composition of the GRP. Normally, the complete GRP is a compination of three main components - the *matrix*, *fibers* and *additives* - working together. Moreover, different glass types and forms are discussed. Typical manufacturing and in-service defects of the GRP are tabulated and shown in Section 2.2 (see p. 5). Section 2.3 (see p. 7) discusses the challenges of the GRP inspection in general. Finally, an inspection plan proposal for the NDT of the GRP is presented in Section 2.4 (see p. 7). It can be used when planning the inspection frequency of critical and general GRP components.

2.1 Composition

A composition is a combination of two or more materials, where the materials interact without being dissolved or fused. The combination is formed by *fiber reinforcement*, a *matrix* and possibly *additives*. The fibers are used to enhance the mechanical characteristics and integrity of the GRP product. The matrix tie the combination together. Widely used matrices are polyester resin, epoxy resin, ceramic materials and carbon. A complete GRP composition consist of glass fiber reinforcement layers and matrix layers, known as *laminates*. The advantages of the GRP are its relatively great strength characteristics, lightness, corrosion resistance, chemical resistance and long lifetime. The disadvantages are that the quality of the GRP might by hard to inspect and in some cases the strength of the matrix may be poor (Saarela et al., 2007).

Glass fiber is the most commonly used reinforcement. 95 % of reinforcements are glass fiber. It is used especially in applications that require simultaneous strength, stiffness and lightness. E-glass (*Electrical glass*) is widely used glass type. E-glass contains only a few alkaline, so its chemical resistance is good. Moreover, it has good mechanical and electrical properties. Other commonly used glass types are C-glass (*Chemically resistant glass*) and S-glass (*high Strength glass*). S-glass is mainly used in the aviation industry. Each glass type differs from others in properties such as chemical composition, diameter , engineering and density of the fibers (Lähteenmäki,

2011).

Glass fiber appears in the GRP products as roving, chopped strand, weave or mat. Roving is formed when one or many tows are combined together. Mats may be composed of either chipped or continuous fibers. fibers are bonded together chemically or mechanically. Weaves are plane surfaces that are formed when lengthwise wraps and crosswise fills are stacked. A weave is even-sided or aligned. In the even-sided weave reinforcement is equally distributed in both directions. In contrast, in the aligned weave reinforcement the weave is aligned more to the other direction. The length of the chopped strands is defined according to the application, usually being $1 \cdots 100$ mm (Saarela et al., 2007). The structure of glass fiber reinforced plastic is isotropic in a macroscopic scale if it is reinforced with short, even-sided fibers. Aligned fibers always lead to *anisotropy*. However, when examined in cross-level, the properties of the GRP are not direction dependent. This *plane isotropic* structure is important especially in ultrasonic testing. The ultrasonic testing is often thought to be complex for completely anisotropic materials.

The structure of a corrosion resistant GRP pipe is shown in Figure 2.1. It consists of an *inner surface*, a *barrier layer*, a *support layer* and an *outer surface*. The inner surface needs to endure the effect of streaming chemicals. The thickness of the inner surface shall be $0.25 \ldots 0.5$ mm. The concentration of the reinforcement fibers shall be smaller than 20 percent by weight. The barrier layer prevents the penetration of chemicals into the support layer. The chemical resistant barrier layer consists of at least two chopped strand mats which have fiber length of 10-50 mm. The concentration of the reinforcement fibers shall be 20-30 weight percentage. The protective layer is formed by the inner surface and the barrier layer. The support layer is engineered to endure loads due to mechanical forces and temperature changes. Concentration of reinforcement fibers shall be 35-75 weight percentage. The outer surface protects the pipe from external corrosion. fibers shall be coated completely by the resin. The thickness of the outer surface shall be at least 0.25 mm (SFS 5162). Sudden changes in the concentration of reinforcement fibers in the barrier–support layer -interface is usually detectable by ultrasonic testing due to changes in acoustic impedances.

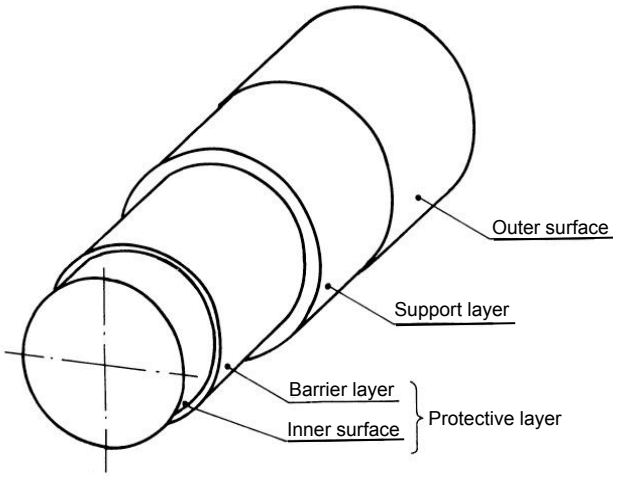

Figure 2.1: Pipe structure (SFS 5162, 2000).

2.2 Typical Defects

For the assessment of the severity of specific defects it is necessary to make relevant standard calibration plates (see Section 8.1 on p. 53) containing flat-bottom drilled holes of various depths and diameters. It is vital that before any NDT technique is used, that it is calibrated in relation to the particular type of composite which is to be inspected. Hence, the limitations and resolution of the techniques are completely known. Above all, the interpretation of inspection results cannot be based on experience with conventional homogenous materials (Harris, 1983).

Manufacturing Defects – Occurrence of manufacturing defects may be due to slight negligence, exceeding in resin processing time, malfunction of winding equipment or incorrect manufacturing parameters (Kakkonen, 2011). Manufacturing defects are listed in Table 2.1.

Table 2.1: Manufacturing defects in reinforced fiber structures (Harris, 1983).

Incorrect fiber volume fraction
Misaligned or broken fibers
Non-uniform distribution of fibers
Matrix-rich region
Imperfectly wetted fibers by the matrix
Pore or void in matrix-rich region
Delamination
Air bubble
Incorrected state of cure resin
Resin crack or ply crack due to thermal stress

Any defect presented in Table 2.1 may result in reduction in strength below the required design stress. Under load the manufacturing defects also tend to grow and they may initiate fatigue damage or crack. Initial reference NDT inspection is as important as the monitoring of the service damages because the inspection results can be compared with the results of the reference inspection(Harris, 1983).

Service Defects – Occurrence of service and testing defects are due to surroundings or mechanical loads.Service defects are listed in Table 2.2.

Table 2.2: Service defects in reinforced fiber structures (Harris, 1983; Kakkonen, 2011).

Fractured fiber
Resin crack
Fiber-resin debond
Transverse ply cracking
Interlaminar cracking
Loss in wall thickness
Impact damage
Delaminations
Erosion
Corrosion
Osmosis bubble
Fracture

2.3 Nondestructive Testing

No single NDT technique can provide a complete picture of the quality of the composite materials. The most common limitation is poor resolution.

The main reason why composite structures are considered to be more difficult for the NDT is because of their nature of being anisotropic and being a combination of two or more materials with highly disparate characteristics. Furthermore, the effects of long term exposure to load and environment are not completely known. *Damage mechanisms* of composite structures vary significantly from damages due to manufacturing methods to damages during loading or when used in an in-service. Naturally, the uncertainty of these defects accumulate and spread is reflecting in design standards and codes of practise. Safety factors as high as 20 are not uncommon for critical applications. The advantage of weight-to-strength ratio is clearly waisted (Harris, 1983).

Inspection objectives are divided into two groups; objectives prior to commissioning and objectives during service. The purpose of inspection prior to commissioning is to form a basis data for corrective actions (i.e. reference measurement) and identify initial defects from specifications or functional requirements. During service, the NDT should assure high levels of safety and regularity (OLF Guideline, 1997).

An engineer faces *three* main problems when analysing the inspection results of composites. The first is to know the tolerated size and distribution of manufacturing defects in material prior to proof-testing. The second is to know the levels of damages introduced by given proof or service loads. The third is to know what effect the defects have on the residual load-bearing ability of the material. Composites are anisotropic and inhomogeneous, and they accumulate defects in a *general* rather than a localized fashion like in metals (Harris, 1983).

2.4 Inspection Intervals

Selection of an inspection program shall be based on a throughout evaluation of the consequences of failure. Assessment of the likelihood and severity of failure can be based on previous experience, material properties, design of process units, operating process conditions, etc. This sample inspection program includes the use of destructive testing of material samples to characterize long-term material degradation under the most aggressive operating conditions, and as a means to extend the GRP structure past its rated life. Such material samples should be representative of the equipment in-service, i.e. by testing a pipe sample removed from service, or by testing coupons which have been exposed to the same media and stress levels that are seen in service. When the initial materials engineering evaluation indicates that destructive

tests are required, the same test methods as those used to pre-qualify the material should be used. It should be noted that even in the chemical industry this level of inspection is seldom required, since suppliers and other users often have extensive experience with the GRP product in similar applications (OLF Guideline, 1997).

The Norwegian Oil Industry Association (OLF) defines the inspection program into four categories: A, B, C and D according to Table 2.4

Table 2.3: Inspection program (OLF Guideline, 1997)

Equipment class	Likelihood and severity of failure		
	High	Medium	Low
Critical	A	B	C
General	C	C	D

Inspection intervals are shown in Table 2.4. Intervals are based on selected insection program.

Table 2.4: Inspection intervals (OLF Guideline, 1997)

	Inspection program and interval			
	A	B	C	D
First inpection (yrs)[1]	0,5-1	0,5-1	1-2	1-2
Inspection interval (yrs)	1-2	2-3	0,2·service life	0,3·service life

(1) after start of service

Recommended NDT techniques based on selected inspection program according to Table 2.5 (see p. 9).

Table 2.5: Recommended NDT techniques (OLF Guideline, 1997)

	Inspection program			
	A	B	C	D
Inspection methods	VT[1] NDT[2] DT[3]	VT[1] NDT[2] DT[3]	VT[1] NDT[2] DT[3]	VT[1]
comments	•Inspection interval shall be reduced if results show severe degradation •All inspection methods listed shall be applied during every inspection •Inspection program B can be applied when sufficient confidence in the material and construction performance has been gained. However, At the earliest, after 5 years service.	•Inspection interval shall be reduced if results show severe degradation •All inspection methods listed shall be applied during first inspection, while the following can alternate between NDT and DT •Inspection program C can be applied when sufficient confidence in the material and construction performance has been gained. However, At the earliest, after 3 years service.	•Inspection interval shall be reduced if results show severe degradation •DT is required if the service life has extended beyond the originally estimated lifetime •Inspection program D can be applied to process equipment classified as "General" when sufficient confidence in the material and construction performance has been gained. However, At the earliest, after 5 years service.	•DT is required if the service life has extended beyond the originally estimated lifetime.

(1) internal/external

(2) most suitable method for degradation mechanism

(3) material samples exposed to the actual process conditions

3 Visual Testing Theory

Basis of all NDT testing is the visual testing (VT). The VT should be done always before any other NDT technique is used, or simultaneously. Inspection results obtained by the VT is restricted to an information that revealed using bare eye sight. Naturally, different light sources, cameras, measuring devices, endoscopes, mirrors and magnifiers can be used as an aid to extend and overcome some limitations of the eye sight. Prior to becoming qualified VT inspector, proper eye sight shall be conformed and color blindness be excluded by doing color vision test. Some colors and shapes may hinder the VT of small objects. Strong contrast may cause restlessness and lead to rapid fatigue.

A huge positive aspect of the VT is the fact that nearly all structures can be inspected. The VT is normally easy to carry out in various stages of manufacture or in-service processes. The inspection objects can be divided into three groups. First group consists of secondary materials that are used to manufacture primary products (semi-finished products, components and base materials). Machined products (products while machining and finished products) form the second group. Finally, new or old products that have been damaged or defected form the third group.

The opacity of the inspection object limits the VT to the surface. Hence, merely surface defects or internal defects unfolded until the surface can be detected. The transparency of a material allows the full detection of internal defects. Poor resolution of an eye is one of the limiting factors in the inspection. Other limiting factors are the fatigue of the eye and because of that, the reduction of the inspection speed and accuracy. The VT is being criticizes due to its major human error effect. However, a profound and proficient VT is always an important first step even when considering carrying out the inspection with the other NDT techniques. If the inspection object does not pass the VT, there is no use applying other techniques.

Sufficient lighting is important factor when carrying out the VT. Distance, reflectivity, luminosity and contrast have effect on determining the sufficient lighting. Moreover, the cleanness, shape and roughness of the surface have their effect also. Minimum illuminance while inspecting shall be 350 lx but the inspection demanding special accuracy may demand illuminance up to 5000 lx. The simplest way to assure sufficient lightning is to keep both a lighting source and an eye close to the inspection object (Moore, 2010).

3.1 Inspection of GRP

In translucent GRP, visual testing reveals of multiple defect types. Standards SFS 3910 and PSK 6312 introduced below, shall be used in the visual testing of the GRP.

Standard SFS 3910 – *Reinforced thermosetting plastics. Visual inspection and classification of corrosion resistant laminates and joints* defines quality of the defects and acceptance levels for the GRP products as well as inspections required. According to SFS 3910 visually perceptive defects are chip, crack, delamination, dry spot, fracture, air bubble, burned area, pit, resin rich area, scratch and impact damage (SFS 3910, 1993).

Standard PSK 6312 – *Industrial Fibre-reinforced Plastic Products. Condition monitoring. Sensory Inspection* describes the visual testing procedure for the GRP and gives instructions for the selection of items to be inspected and analysis of test results. PSK 6312 gives informative examples about the defect types assumed to be found from the outer surface, inner surface, support layer and layer interface (PSK 6312, 2011).

4 Infrared Thermography Theory

Infrared thermography (IRT) is one of the most versatile NDT techniques available today. It offers real-time, fast response, two-dimensional measurements of varying target areas. Infrared image analysis is a diagnostic evaluation tool for defects in a wide range of applications (Walker, 2004). Basic physics understanding related to the IRT such as thermodynamics and electromagnetic radiation will prove invaluable successful for application of infrared thermography. Generally speaking, the IRT is based on the ability to detect small temperature variations. For example, a thinning of wall thickness is indicated as warmer temperature because thinner area warms up faster than wider, defectless area around it.

The goal of the first section 4.1 (see p. 12) is to familiarize terms such as *temperature*, *heat*. In Section 4.2 (see p. 13) the different *heat transfer mechamisms* are discussed. The IRT relies on laws of physics that relate to the transfer of thermal energy. It is good to emphasize that all forms of heat transfer are important in IRT, not only infrared radiation. Each heat transfer mechanism has the capability to influence surface temperatures and the amount of infrared radiation emitted from the surface. In Section 4.3 (see p. 14) an introduction is given for *infrared radiation*, *infrared spectrum* and *wavelength region* and the physical equations explaining IR radiation, namely *Planck's radiation law*, *Wien's displacement law* and *Stefan-Boltzmann law*. An important quantity of *emissivity* is introduced in Section 4.4 (see p. 17). Specific notes on the IRT for the GRP are given in the final Section 4.5 (see p. 20).

4.1 Temperature and Heat

Temperature is the most common measure to quantitatively define the concepts of hot and cold. It's also the most widely measured physical quantity in science and engineering. Physically, intense thermal vibration relates to high temperature and weak thermal vibration relates to low temperature. Furthermore, higher temperature of a body indicates greater capacity to transfer its heat to other bodies.

The two most commonly used temperature scales are the SI (System International) *Kelvin* (K) *scale* and *Celsius* (°C) *scale*. Kelvin scale is an absolute temperature scale, meaning that there is no thermal vibration at 0 K temperature. Consequently, it's the lowest attainable temperature. Kelvin scale is used in all of the SI-unit physical equations. Celsius scale's 0 °C is defined as the freezing point of water and 100 °C is defined as the boiling point of water under normal temperature and pressure condition. The relation between the Kelvin and the Celsius scale is

$$[\mathrm{K}] = [^{\circ}\mathrm{C}] + 273,15. \tag{4.1}$$

Although the scale is different, the interval remains the same $\Delta 1$ K=$\Delta 1$ °C.

Heat is the transfer of energy from one part of a material or substance to another, or from one body to another due to temperature difference. The second law of thermodynamics states that it is impossible for any process to have as its sole result the transfer of heat from a cooler body to a hotter one (Young and Freeman, 2008). As a result, the warmer body cools down and the cooler body heats up until thermal equilibrium is reached, resulting that the temperature of each body has equalised.

4.2 Mechanisms of Heat Transfer

Mechanisms of heat transfer are *conduction*, *convection* and *radiation*. Heat transfer occurs as a combination of mechanisms or as a single mechanism. These transfer mechanisms are responsible for a material receiving or losing thermal energy.

Conduction – Molecules vibrate more actively in hotter regions than cooler regions. The vibration of molecules of all materials is an outcome of heat transfer process. In all states of matter (*solids*, *liquids* and *gases*), each vibrating molecule interacts with its neighbouring molecules causing them to vibrate, and finally reach thermal equilibrium. This chain reaction cycle of vibrating molecules is termed conduction.

Conduction is the only way thermal energy can flow between or through solids in direct contact. *Thermal conductivity* of any given material and temperature difference give boundary conditions for the *speed of conduction* or *heat current* (Walker, 2004). Heat current (H) is the rate of a quantity of heat dQ transferred through a block in a time unit dt. Experiments show that heat current is proportional to the cross-sectional area A of the block and to the temperature difference ($T_H - T_C$) of the ends of the block and is inversely proportional to the length L of the block. Introducing thermal conductivity constant k_c, we have (Young and Freeman, 2008)

$$H = \frac{dQ}{dt} = k_c A \frac{T_H - T_C}{L}. \tag{4.2}$$

Convection – In convection, energy is removed from the surface molecules of a solid and transferred to a liquid, gas or rheid. Molecular bonding is non-existent compared to conduction, therefore heat is transferred both in molecular contact and in molecular displacement.

Natural convection occurs when liquid or gas molecules are thermally excited and confront surfaces of higher temperature. Molecular vibration causes the molecules to simultaneously expand, become less dense, rise and be displaced by denser cooler

molecules under the influence of gravity. Forced convection occurs due to any other method or force that creates movement (Walker, 2004).

Radiation – Infrared radiation is the basic heat transfer mechanism for the IRT. Understanding of infrared radiation requires knowledge of transfer of thermal energy by electromagnetic radiation. The rate of energy radiation from a surface is proportional to area A, emissivity ε, Stefan-Boltzmann constant σ and the fourth power of temperature T^4. Taking into account the temperature of surroundings T_S, the net heat current of radiation is (Young and Freeman, 2008)

$$H_{net} = A\varepsilon\sigma(T^4 - T_S^4). \tag{4.3}$$

The surface finishing of an object and the characteristics of the surface dictate the degree of emitted infrared radiation from the surface. Even emissivity can be slightly temperature dependant (Young and Freeman, 2008). Recognising these aspects is a vital part of the IRT-inspector's training. Hence, the next Section 4.3 has been devoted entirely to the subject of infrared radiation.

4.3 Infrared radiation

Infrared radiation is part of the electromagnetic radiation of continuous spectrum that all matter or body above absolute zero (0 K or -273,15 $^{\circ}\mathrm{C}$) emits or absorbs. Abnormal levels of emitted radiation from an object surface refers to defected area. Study of the infrared radiation have been the key reasons for development of infrared thermography.

Electromagnetic Spectrum – The wave nature of electromagnetic radiation is characterised by its *wavelength* (λ) and *frequency* (f). The speed of all electromagnetic radiation is equal to the speed of light ($c = 2,998 \cdot 10^{23}\ \frac{\mathrm{m}}{\mathrm{s}}$). Frequency is inversely proportional to wavelength as shown in Equation (4.4).

$$f = \frac{c}{\lambda}. \tag{4.4}$$

The vibration rate of exited electrons determines wavelength and frequency. Vibration is mainly governed by the inherent internal kinetic energy of the body (Walker, 2004).

The infrared wavelength region of the spectrum lies between 750 nm and 100 $\mu\mathrm{m}$. Infrared thermography makes use of wavelengths between 2 and 6 $\mu\mathrm{m}$, usually referred to as *middle infrared region* or *shortwave* (SW). The *far infrared region* (8 to 14

μm), usually referred as *longwave* (LW). Together the middle and far infrared regions are known as the *thermal infrared region* or the *thermographic range*. There are two reasons for splitting of the thermographic range. First, the atmosphere attenuates 6 to 8 μm wavelengths due to absorption by carbon dioxide (CO_2), water (H_2O) and ozone (O_3) (see Figure 4.1). Second, the transmission and detection characteristics of the IRT optics and detector are not optimized for the entire range of 2 to 14 μm. Wavelengths above 14 μm (extreme infrared region) have low energy and are usually unable to penetrate the atmosphere. Thus, the extreme infrared region is unimportant from the IRT point of view (Walker, 2004).

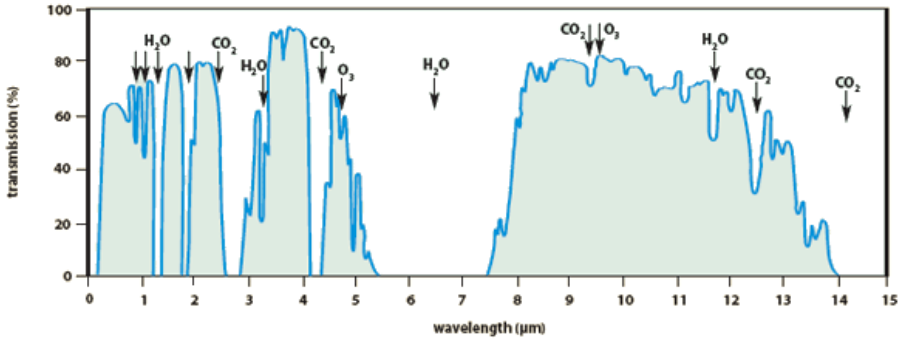

Figure 4.1: Atmospheric transmission in infrared region (Infrared Spectral Selection, 2015).

A blackbody completely absorbs any heat or light radiation falling upon it. Blackbodies are only theoretical because no known object or substance is a perfect absorber or emitter. Blackbodies are used to familiarize the radiation characteristics of a surface. Blackbodies are important for the scientific explanation and understanding of infrared radiation principles. Section 4.4 (see p. 17) describes how emissivity is linked to the three radiation laws introduced next.

Planck's Radiation Law – Planck's radiation law describes the total emission intensity for a blackbody as a function of wavelength

$$I(\lambda) = \frac{2\pi hc^2}{\lambda^5(e^{\frac{hc}{\lambda k_B T}} - 1)}. \tag{4.5}$$

Equation (4.5) predicts the existence about *photons*. Photons are the quanta of light that are elementary particles in which the energy of light is embedded. The detectors of thermographic cameras are engineered to be sensitive to photon activity and so temperature measurement is based on levels of photon activity striking the detector surface. Planck's radiation law controls the distribution of radiation. Consequently, it also includes laws proved before:

Wien's displacement law (4.6) and Stefan-Boltzmann law (4.7). Figure 4.2 illustrates Planck's radiation law and Wien's displacement law for different temperatures. The plotted curves are known as *planckian curves*.

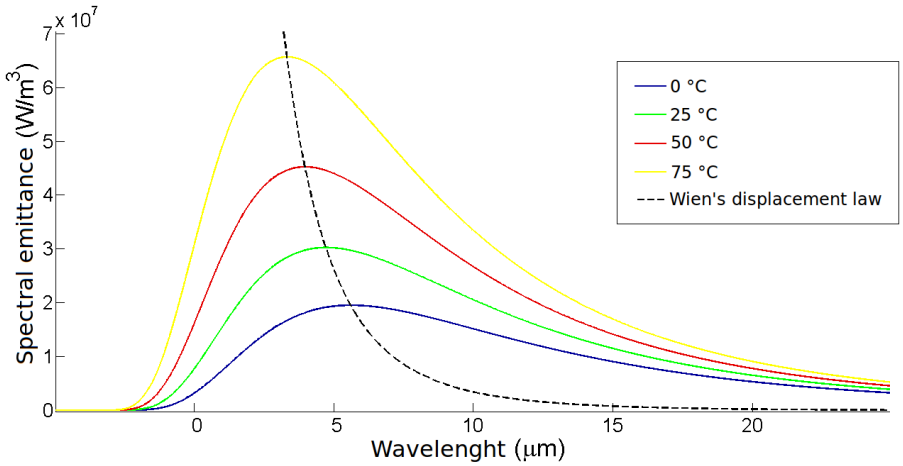

Figure 4.2: Planckian curves. Radiation is entirely in the infrared region.

Wien's Displacement Law – Wien's displacement law gives the distribution of radiation for different wavelengths

$$\lambda_m T = 2,90 \cdot 10^{-3} \text{ mK}, \tag{4.6}$$

where λ_m gives the position of the maximum intensity of radiation. Figure 4.2 illustrates the displacement of the maximum intensity of radiation to shorter wavelengths. As previously stated, λ_m is achieved by differentiating Planck's formula (4.5) (see p. 15) with respect to λ.

Stefan-Boltzmann Law – Stefan-Boltzmann law can be derived by integrating Equation (4.5) (see p. 15) while lower limit is $\lambda = 0$ and upper limit is $\lambda = \infty$. Integral gives the total area under a planckian curve for a specific surface temperature, that is the total intensity of radiation.

$$I = \sigma(T^4 - T_S^4), \tag{4.7}$$

The temperature of the surroundings (T_S) has been taken into account in Equation (4.7).

The intensity of radiation is very much temperature dependent. While temperature increases, an object radiates more energy at every wavelength due to increased molecular activity and planckian curves shift towards shorter wavelengths. When temperature is equal or more than 500 °C , energy will be generated increasingly in

the visible part of the spectrum. Fortunately, temperature does not exceed 500 °C in most IRT applications.

4.4 Emissivity

Moving from the concept of a *blackbody* to a *real body* makes the theory slightly more difficult. Real bodies absorb, reflect and transmit radiation, however the sum of absorptivity α_λ, reflectivity ϕ_λ and τ_λ transmissivity τ_λ is always constant

$$\alpha_\lambda + \phi_\lambda + \tau_\lambda = 1. \tag{4.8}$$

Lower index λ is used to imply wavelength dependence. In practice, most materials are opaque to infrared radiation ($\tau_\lambda = 0$). Thus, Equation (4.8) simplifies to

$$\alpha_\lambda + \phi_\lambda = 1. \tag{4.9}$$

From the IRT point of view, *emissive properties* of a surface are interesting. Fortunately, objects that are good absorbers of infrared light are equally good reflectors. *Kirchhoff's law of thermal radiation* implies that good radiators are good absorbers. Relation of emissivity ε_λ and absorptivity α_λ can be written as

$$\frac{\alpha_\lambda}{\varepsilon_\lambda} = 1 \iff \alpha_\lambda = \varepsilon_\lambda, \tag{4.10}$$

since they are properties of the surface. By substituting Equation (4.10) to Equation (4.9) we have

$$\varepsilon_\lambda + \phi_\lambda = 1. \tag{4.11}$$

However, *thermal imbalances* can occur due to not only because interaction of objects of different temperatures with one another but also because emissivity varies with temperature (Walker, 2004). After scaling Equations (4.5) (see p. 15), (4.6) (see p. 16) and (4.7) (see p. 16) with emissivity ε, blackbodies become graybodies that are indeed real bodies. Some bodies cannot considered even as a gray bodies because their emissivity varies as a function of wavelength.

As previously stated, temperatures do not exceed 500 °C in most of the IRT applications. As a result, the emitted radiation is located completely in the middle infrared region. The total irradiance received by the IRT camera can be written as a combination of emissivity of the surface ε, radiance emitted from the surface $E_{sur}(\lambda)$, radiance emitted from environment $E_{env}(\lambda)$. Neglecting the atmosphere contribution as in most NDT applications gives the fundamental equation of infrared thermography

$$E_{cam} = \varepsilon E_{sur}(\lambda) + (1 - \varepsilon) E_{env}(\lambda). \tag{4.12}$$

An IRT camera measures heat flux from the received spectral irradiance (Maldague and Moore, 2001). The optics of thermal imaging cameras gather and focus the incoming spectral irradiance to a detector. The detector is fabricated to be sensitive for the infrared portion of the electromagnetic spectrum. The detector covers incoming infrared energy to an amplified electrical signal. The amplified signal is then processed and displayed as a thermogram, typically on a LCD viewer (Walker, 2004).

Emissivity Evaluation – As a rule of thumb, clean metals with emissivity ranging from 0,05 to 0,2 act like a mirror and non-metallic, organic materials and coated metals with emissivity ranging from 0,8 to 0,95 act more like blackbodies. High emissivity materials have much larger emitting area than reflecting, making these materials much easier to measure accurately using the IRT. Reliable and accurate temperature measurement is possible only if the camera emissivity setting corresponds to the emissivity of the measured surface. Thus, it is *mandatory* for an NDT-inspector to determine the target emissivity value and apply them accordingly (Maldague and Moore, 2001).

Surface Finish – Mirror-like, smooth surfaces reflect incident radiant energy at the angle complimentary to the angle of incidence; this is known as *spectral reflectance*. However, no surface is a perfect reflector, surface irregularities and textured surfaces present a multitude of angles incident to the radiation source. Therefore, a percentage of radiation will be diffused or scattered. This effect is known as *diffuse reflectance*. The IRT camera emissivity setting should be adjusted to compensate spectral and diffuse surface characteristics (Walker, 2004).

Angle of Measurement – The IRT should always be done perpendicular relative to the target surface to ensure that the surface does not appear to be cooler than it really is. If the IRT camera is not perpendicular to the target surface, the surface is reflecting more background temperature; this can be partially compensated by increasing target surface in IRT cameras *field of view* (FOV) (Walker, 2004).

Reflected Temperature (T_{amb}) – Obviously, a background temperature has an effect on the target surface. An IRT-inspector is usually able to determine the significance of specific background temperature by shielding the target from such a source and observing the difference and adjusting the ambient temperature (T_{amb}) setting on the camera to obtain better temperature measurement accuracy. Low emissivity targets are affected more by ambient temperature than high emissivity targets (ε>0,9) because they have an ability to act as a good reflector. For a possible low emissivity

target, emissivity must be accurately determined and also background temperature must be taken in to account.

Surfaces with much higher or lower temperature than a low emissivity target should be shielded. Good method for obtaining T_{amb} is use to appropriately sized aluminium foil. First, crumple and re-flatten the aluminium foil. Second, aluminium foil should be adhered to a flat piece of card. Third, foiled card should be placed in front of but facing away from the target surface to reflect all reflected temperature T_{amb} but not temperature from target to the IR camera. Finally, T_{amb} can be determined by measuring foiled card from various angles and averaging the temperature. For this activity, IR camera emissivity setting should be set to 1,0 and distance setting should be set to minimum (Walker, 2004).

Atmospheric Temperature (T_{atm}) – T_{atm} is the temperature of the atmosphere between the IRT camera and the target surface. T_{atm} is a required parameter to be set to the IRT camera or software for calculation of temperatures. T_{atm} can be measured on site by using a digital thermometer, measuring the temperature of a suspended cardboard of a nearby high emissivity surfaces. Relative high errors in T_{atm} can be tolerated when the temperature difference between target and T_{atm} is high. On the other hand, accurate determination of T_{atm} is desirable in order to avoid temperature errors when the temperature difference between the target and T_{atm} is low. It is recommended to avoid reflections nearby hot objects when determining T_{atm}. Also low emissivity objects should not be used for determination of T_{atm} (Walker, 2004).

Temperature and Emissivity – Normally increase in surface temperature increases emissivity. This phenomenon should be compensated in order to avoid erroneous measurements. Some materials actually behave vice versa but such materials are not usually encountered in industrial infrared thermography investigations.

Reference tables of emissivity should be used to adjust the IRT camera emissivity setting according to the temperature, target material and spectral responce (longwave, LW or shortwave, SW) of the IRT camera (Walker, 2004).

Determining Emissivity – Before the assessment of emissivity, the atmospheric temperature (T_{atm}) shall be determined and the IRT camera's T_{atm}-setting should be adjusted accordingly. The reflected temperature (T_{amb}) shall be compensated providing that all external sources of infrared radiation are removed or shielded.

PVC tape is an easy and useful tool for determining unknown emissivity because it has very high emissivity (ε_{PVC}=0,97), it is easy to adhere to almost any material and a quick thermal equalisation takes place with the target.

PVC tape shall be adhered to the target surface and the IR camera emissivity setting shall be adjusted to 0,97, and the surface temperature of the PVC tape (that is the correct surface temperature value) is recorded. Next, the IR camera emissivity setting shall be adjusted so that surface temperature corresponds to the previously measured PVC tape temperature. Now, emissivity setting should be close approximation of the real emissivity of the target surface (Walker, 2004).

4.5 Inspection of GRP

Standard PSK 6316 – *Industrial Fibre-reinforced Plastic Products. Condition monitoring. Thermographic Camera Inspection* presents infrared thermography as a nondestructive testing technique for fiber-reinforced plastics. In addition, the IRT camera specifications, instructions for selecting inspection objects, image processing and analysis are included in the standard. A reference measurement is considered mandatory.

The IRT camera must have a minimum thermal sensitivity of 0,1 °C and the IR resolution shall be 120×120 pixels or greater. The temperature difference between the object and its surroundings must be at least ±10 °C. Focus must be the sharpest possible before inspection because it cannot be changed afterwards. The emissivity factor shall be set to 0,95 for the inspection of fiber-reinforced plastics. Detailed recommendations are found from PSK 6316 (PSK 6316, 2009).

Infrared thermography is one of the best diagnostic NDT techniques for the inspection of the GRP. Other NDT techniques shall be used for more accurate measurements in order to identify the reason behind the temperature changes.

5 Phased Array Ultrasonic Testing Theory

Phased array ultrasonic testing (PAUT) is a powerful NDT technique. Its use is becoming more common in multiple applications because of the advantages it offers over the conventional ultrasonic testing (UT). The PAUT probes assemblies with from 16 to as many as 256 elements where conventional ultrasonic *transducer* or so called *probe* has just one element. The multiple elements can be utilized together in order to steer, shape and focus the ultrasonic beam increasing both inspection flexibility and capability. This ability is essential in terms of the inspection data visualization (Phased Array Tutorial). The theory of the PAUT may seem complex. Therefore, understanding of the physics concepts related to the PAUT such as mechanical waves, Snell's law and interference will prove critical for successful inspections. Some of the most important factors concerning the understanding of the phased array instrument and visualization are also discussed. In general, the PAUT is based on the reflected sound pressure from the interfaces inside the inspected structure. In homogeneous structure, the sound reflects between back and front facets because they form the only two interfaces with air. The first reflection in case of the defectless structure is the first back wall echo. If an echo is detected before the first back wall echo, it is normally a defect indication. However, the GRP structure is anisotropic and therefore multiple weak echoes are detected before the first back wall echo but the first back wall echo is always shown as the strongest echo in the defectless structure.

This Chapter begins with the introduction of *mechanical waves* in Section 5.1 (see p. 22), in which *pressure*, *attenuation*, *velocity* and *couplant* are discussed and mathematical description of a wave is derived. Important concept of the *Snell's law* is presented in Section 5.2 (see p. 27). Also introduction is given for the *critical angles* and the *temperature effect* on velocity. The PAUT relies on laws of physics that relate to the phenomena called *interference*. Interference and the characteristics that rely on it, namely *bending*, *steering* and *focusing* of ultrasonic waves, are presented in Section 5.3 (see p. 29). Section 5.4 (see p. 31) deals with *transducers* (also called *probes*) and their properties. The explanation of the *near field* effect is given in Section 5.5 (see p. 32). The near field is a nonuniformed beam front near the probe facet. The *ultrasonic views* or *scans* are introduced in Section 5.6 (see p. 34). The variety of ultrasonic views offer useful tool for the visualization and analysis of inspection data. Finally, specific notes on the PAUT for the GRP are given in the Section 5.7 (see p. 38).

5.1 Mechanical Waves

Ultrasound is a mechanical wave; a disturbance that travels through medium while the frequency (f) is higher than 20 kHz. Most industrial applications require frequencies between 100 kHz and 50 MHz. *Acoustic Spectrum* in Figure 5.1 consist of three ranges of frequencies and *The Ultrasonic Range* is broken down into three sub-sections.

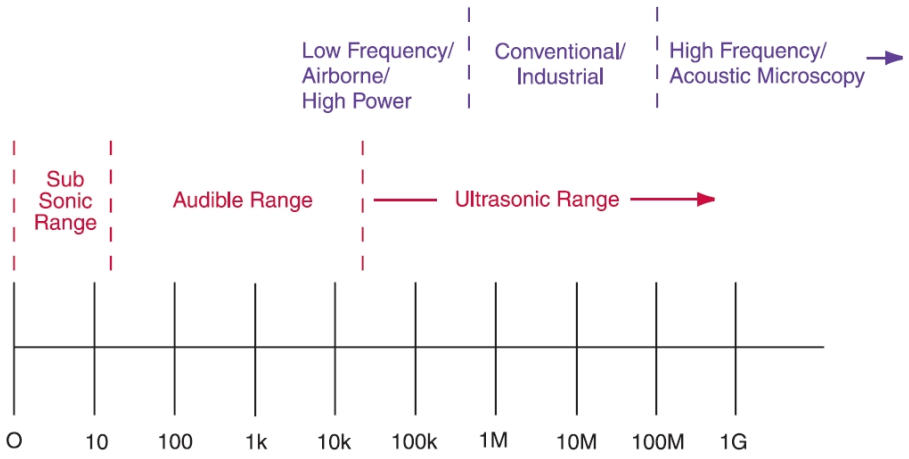

Figure 5.1: Acoustic spectrum (Panametrics, 2012).

Ultrasound has a short wavelength (λ) due to its high frequency. This property makes ultrasound useful for the NDT because the smallest detectable defect is theoretically $\lambda/2$. The time required to complete a full cycle is the period (T), defined as

$$f = \frac{1}{T}. \tag{5.1}$$

All periodic waves have the same proportional relation between wavelength and frequency

$$v = \lambda f. \tag{5.2a}$$

and by substituting Equation (5.1), we have

$$v = \frac{\lambda}{T}. \tag{5.2b}$$

Ultrasound appears in different wave modes. In liquids and gases, the propagation of ultrasonic waves only occurs in *longitudinal wave mode*. In solids ultrasound may appear in but is not limited to *longitudinal*, *transverse* (*shear*), *Surface (Rayleigh)*, *Plate Wave (Lamb)*, *Plate Wave (Love)*, *Stoneley (Leaky Rayleigh Waves)* or *Sezawa* wave modes (NDT Resource Education, 2015). Longitudinal (*L-waves*) and shear (*S-waves*) wave modes in Figure 5.2 are the most important for the NDT applications.

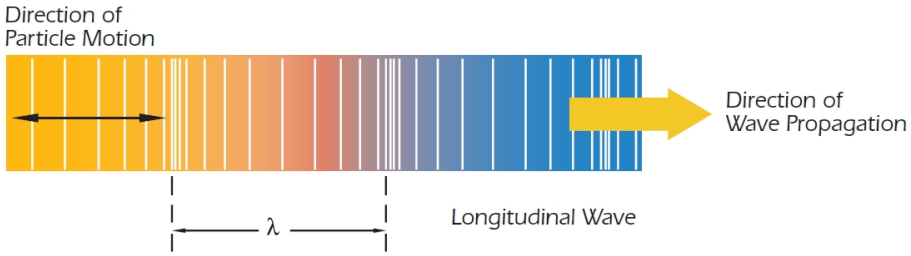

(a) L-wave.

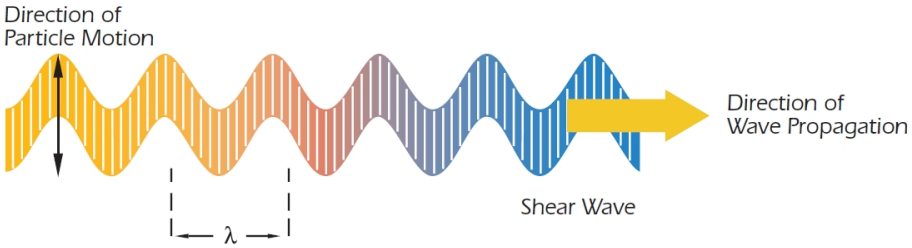

(b) S-wave.

Figure 5.2: The most important wave modes (Panametrics, 2012).

Ultrasonic waves have the physical properties of *reflection*, *refraction*, *attenuation*, *dispersion*, *interference*, *diffraction*, *polarization* and *mode-conversion*. Interference, the fundamental phenomenon for phased array ultrasonic testing is introduced in Section 5.3 (see p. 29) and the other important physical properties are covered briefly in the other Sections.

Pressure – Typically, the propagating type of ultrasound is either *cylindrical* or *spherical* (see Figure 5.3 on p. 24) but most of the sound pressure can be directed to the pre-defined direction.

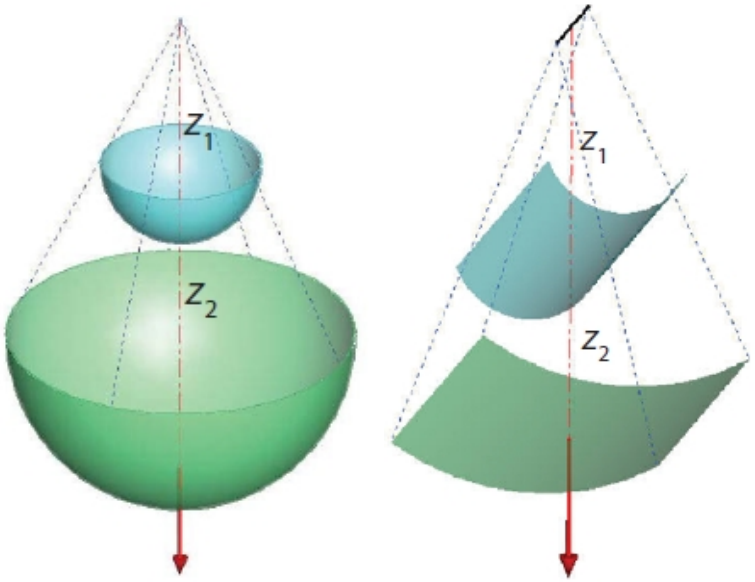

(a) Spherical propagation (point source).

(b) Cylindral propagation (line source).

Figure 5.3: The propagation of sound in medium (Dubé, 2004).

Intensity of sound is defined by pressure of sound p, mass density ρ and speed of sound v

$$I = \frac{p^2}{\rho v} \quad , \tag{5.3a}$$

therefore,

$$I \sim p^2. \tag{5.3b}$$

The average intensity at any distance in a case of a point source (see Figure 5.3a) is

$$I_{spherical} = \frac{P}{A} = \frac{P}{2\pi z^2}, \tag{5.4}$$

where the area A is spherical surface divided by two.

Similarly, the average intensity at any distance in a case of a line source (see Figure 5.3b) is

$$I_{cylindral} = \frac{P}{A} = \frac{P}{\theta z h}, \tag{5.5}$$

where the area A is the portion of cylindral surface, θ is the opening angle, z is the radius and h is the height of the cylinder.

By taking the ratio of two spherical intensities and using Equations (5.3b) and (5.4),

we get the following laws

$$\left(\frac{I_2}{I_1}\right)_{spherical} = \left(\frac{p_2}{p_1}\right)^2_{spherical} = \left(\frac{z_1}{z_2}\right)^2 \tag{5.6a}$$

and

$$\left(\frac{p_2}{p_1}\right)_{spherical} = \left(\frac{z_1}{z_2}\right). \tag{5.6b}$$

The derivation of ratio between two cylindral intensities is similar to the derivation of the Equations (5.6a) and (5.6b) above. By using Equations (5.3b) and (5.5) we get

$$\left(\frac{I_2}{I_1}\right)_{cylindral} = \left(\frac{p_2}{p_1}\right)^2_{cylindral} = \left(\frac{z_1}{z_2}\right) \tag{5.7a}$$

and

$$\left(\frac{p_2}{p_1}\right)_{cylindral} = \left(\frac{z_1}{z_2}\right)^{\frac{1}{2}}. \tag{5.7b}$$

Reflection and Transmission of Pressure – The boundary of two materials of different *acoustic impedances* is called an *interface* or an *acoustic interface*. The difference between the acoustic impedances define the *reflection* and *transmission coefficients*. Acoustic impedance is defined by mass density and speed of sound in certain material and is given by the following Equation

$$Z = \rho v. \tag{5.8}$$

Reflection (R) and transmission (T_{tc}) coefficients for normal angle of incidence is given as the percent of pressure (Dubé, 2004)

$$R = \frac{Z_2 - Z_1}{Z_2 + Z_1} \tag{5.9}$$

and

$$T_{transmission} = \frac{2Z_2}{Z_2 + Z_1}. \tag{5.10}$$

The reflection loss in decibels is (Dubé, 2004)

$$\Delta R_{\text{reflection}} = -20 \log_{10}\left[\frac{\mathrm{Z_2 - Z_1}}{\mathrm{Z_2 + Z_1}}\right], \tag{5.11}$$

and the transmission loss in decibels is (Dubé, 2004)

$$\Delta G_{\text{transmission}} = -20 \log_{10}\left[\frac{\mathrm{Z_1 Z_2}}{(\mathrm{Z_2 + Z_1})^2}\right]. \tag{5.12}$$

Equations (5.9) (see p. 25) and (5.10) (see p. 25) become more complex if the angle of incidence and multiple interfaces need to be taken into account. However, for the purpose of this work they are sufficient for understanding of the phenomena (Anderson, 2010).

Mathematical Description of a Wave – A transverse wave travelling in one dimension can be described by the *acoustic wave equation*

$$\frac{\partial^2 p(x,t)}{\partial x^2} = \frac{1}{v^2}\frac{\partial^2 p(x,t)}{\partial t^2}. \tag{5.13}$$

The solution for Equation (5.13) is the *pressure of sound of a wave function*

$$p(x,t) = p_0 \sin(\omega t - kx). \tag{5.14}$$

Equation (5.14) will provide important insight how steering, focusing and bending of the ultrasonic wave front are accomplished through the phenomena of interference as explained in Section 5.3 (see p. 29).

Amplitude – Amplitudes of two signals may be used to compare the signals. The amplitude variation is defined as

$$\Delta\text{dB} = 20 \log_{10}\left(\frac{h_{s1}}{h_{s2}}\right), \tag{5.15}$$

where h_1 and h_2 are the percentages of first and second signals of full screen height, respectively. ΔdB is the difference of signal amplitudes in decibels.

Determination of Velocity – Usually, the thickness of the material is known but especially the velocity of ultrasound for exotic materials is often unknown. The law describing velocity in *pulse-echo technique* is

$$s = 2\Delta d = v\Delta t, \tag{5.16a}$$

so

$$v = \frac{2\Delta d}{\Delta t}, \tag{5.16b}$$

where $2\Delta d$ is the ultrasonic path that the ultrasound travels between two back wall echoes. By measuring *time-of-flight* for two sequential echoes t_1 and t_2, we have

$$v = \left|\frac{2d}{t_2 - t_1}\right|. \tag{5.17}$$

Similarly, the *through-transmission technique* can be used. Then, Equation (5.17) gets the form of

$$v = \left| \frac{d_2 - d_1}{t_2 - t_1} \right|, \tag{5.18}$$

because sound travels the thickness of the plate only once.

Determination of Attenuation – Attenuation is the reduction in *amplitude*, *density*, or *energy* as the result of friction absorption and scattering (basically loss of sound as it travels through a material, generally more pronounced as grain size increases). The attenuation depends on frequency, grain size, wave type, and the anisotropy coefficient.

Attenuation coefficient (α) can be solved by using a probe with a normal angle of incidence and measuring the difference of two consecutive back wall echoes ($h_{1\mathrm{dB}}$ and $h_{2\mathrm{dB}}$) in desibeles in pulse-echo technique. Substituting the values, we have

$$\alpha = \frac{h_{1\mathrm{dB}} - h_{2\mathrm{dB}} - 6\mathrm{dB}}{2t}, \tag{5.19}$$

where t is the thickness of the material and -6 dB is the *geometrical constant attenuation* due to diffraction, scattering and absorption.

Ultrasound attenuates rapidly in the GRP. This may result in inability to measure two sequential echoes.

Couplant – A couplant is used between the probe and the target to get good *acoustic contact*. In some cases, surface roughness forces to use a thick layer of couplant. Optimally, the couplant thickness should be less than $\lambda/2$ to minimize gain loss. Ideally, the couplant thickness should be only a few microns. For instance, for a couplant thickness of $\lambda/4$, the gain loss is about 5 dB. As a rule of thumb, the couplant thickness should be minimized but not with the cost of contact (Dubé, 2004).

5.2 Snell's Law

Snell's law (*the law of refraction*) describes both reflection and refraction of ultrasound. Figure 5.4 (see p. 28) illustrates, schematically the situation when ultrasound encounters an interface. The parameters used in Snell's law also introduced.

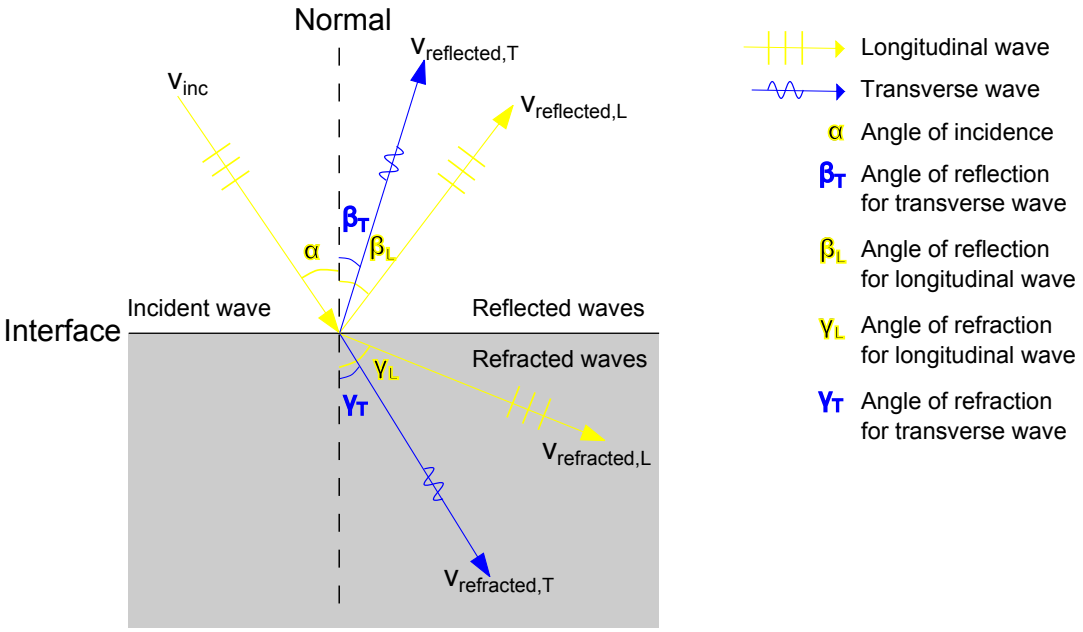

Figure 5.4: Schematic figure of Snell's law.

Snell's law for reflection is

$$\frac{\sin(\alpha)}{\sin(\beta_{\mathrm{x}})} = \frac{v_{\mathrm{inc}}}{v_{\mathrm{reflected,x}}} \tag{5.20a}$$

and for refraction it is

$$\frac{\sin(\alpha)}{\sin(\gamma_{\mathrm{x}})} = \frac{v_{\mathrm{inc}}}{v_{\mathrm{refracted,x}}}, \tag{5.20b}$$

where x implies either L-wave or T-wave. Equations (5.20a) and (5.20b) can be derived experimentally but they can also be derived theoretically from a wave description of sound (*Huyens' principle*). Snell's law is applied as well to *critical angles* discussed next.

Critical Angles – Definition of critical angles refer to angles of incidence in which longitudinal and transverse wave modes *refract* to propagate along the interface. In other words, the angle of refraction in Figure 5.4 is $\gamma_{\mathrm{x}} = 90°$. However, Snell's law may be used in every situation. Even though Zetec Advanced PA Calculator -software is used to calculate proper angles of incidence, the knowledge of the critical angles is important.

The first critical angle (α_{I}) is the threshold value for the angle of incident *related* to longitudinal wave mode. While the angle of incidence is

$$\alpha \geq \alpha_{\mathrm{I}}, \tag{5.21}$$

the longitudinal wave mode refracts to propagate along the interface, therefore γ_{L} =90°.

The second critical angle (α_{II}) is the threshold value for the angle of incident *related* to transverse wave mode. While the angle of incidence is

$$\alpha \geq \alpha_{\mathrm{II}}, \tag{5.22}$$

the transverse wave mode refracts to propagate along the interface, therefore γ_{T} =90°

Temperature Effect – Speed of ultrasound is temperature dependent. Temperature variations increase with the angle of refraction. Specific tables can be used to find the corrected velocities for target material in certain temperature. Velocity variations must be taken into account to avoid errors in defect detection, sizing and positioning (Dubé, 2004).

5.3 Interference

As previously stared, phased array ultrasonic testing is based on *interference*. Interference occurs when waves from two or more sources interact.

Inside a probe, piezo composite elements are pulsed according to computer controlled *delay* or *focal law*. The focal law contains information about the delay and amplitude of individual wave function. This *phase shifting*, or *phasing*, is in turn a way of controlling interference interactions by time-shifting wave functions that originate from two or more sources.

Equation (5.14) may be used to understand the interference phenomenon. By changing time t, phase shifting is achieved. Waves defined by phase shifted wave functions can be described as a single wave front according to *superposition principle*. The superposition principle states that the *net displacement* for waves of the medium at any point in space or time, is simply the sum of the individual wave displacements. Final wave front(s) is (are) predefined by focal law. Thus, constructive and destructive interference wave fronts propagate in medium as desired. This can be used to bend, steer or focus the energy of a wave front (Dubé, 2004).

Figure 5.5 shows the bi-modal components of a plane wave created by using 12 elements in a 25 mm aperture (every other element was deactivated to better illustrate the *wavelet* composition of the wave fronts). The calculated angle was 40° for the longitudinal mode which results in a 24° transverse mode following it.

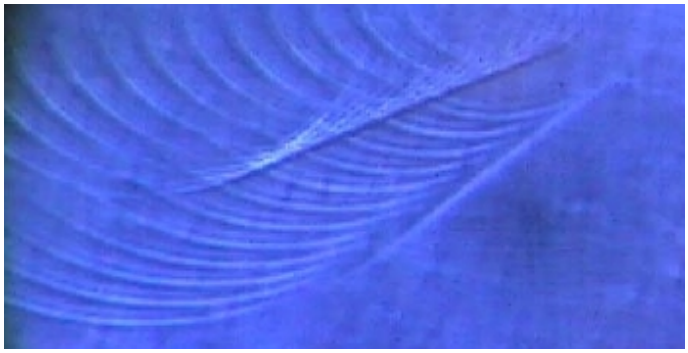

Figure 5.5: Photo elastic visualization of phased array ultrasonic in glass (Ginzel and Stewart, 2004).

Bending, Steering and Focusing of Ultrasonic Waves – One of the most important features of the PAUT compared to the conventional UT is the capability to bend, steer and focus ultrasonic waves. This is made possible by delaying elements. Figure 5.6a (see p. 30) shows how delayed elements in a PA probe interact through interference to form a focused beam into a certain depth. Figure 5.6b (see p. 30) illustrates how delayed elements are used to both steer and focus ultrasonic energy. In both cases, Zetec Advanced PA Calculator -software has been used to create the desired wave fronts.

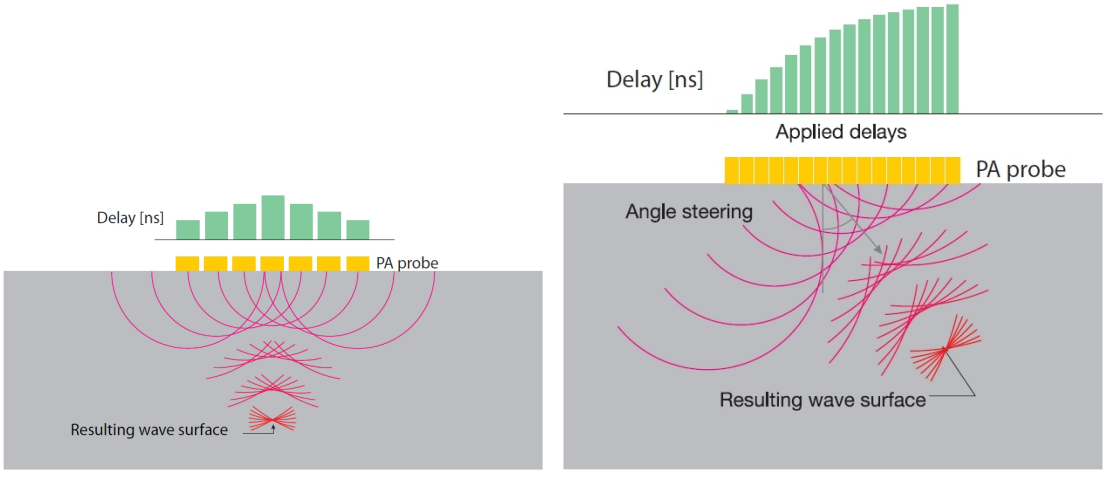

(a) Focusing normal to the surface.

(b) Simultanous steering and focusing.

Figure 5.6: Princible of beam focusing and steering (Dubé, 2004).

5.4 Probes

Appearance of probes and element models vary depending on the type of applications (see Figures 5.7a and 5.7b). The maximum amount of acoustic energy is transferred to the target when the acoustic impedance of the probe is *equal* to the target (reflection coefficient is zero in Equation (5.9) on p. 25). In many applications, the probe is mounted to a wedge. Then, the acoustic impedance of the wedge should be as close to the targets impedance as possible to attain energy transfer. *Impedance matching* between probe/wedge and the target may be achieved by a *matching layer* (see Figure 5.8 on p. 32) or electrical methods. The key requirements for the matching layer are optimization of energy transfer, influence on the pulse duration, contact protection for piezoelectric elements and a layer thickness of $\lambda/4$. A good backing material (see Figure 5.8 on p. 32) features high acoustic attenuation so that echoes from the crystal face are minimized and influence on pulse duration, so called high *damping* is achieved (Dubé, 2004).

(a) Phased array probes (Olympus NDT, 2010).

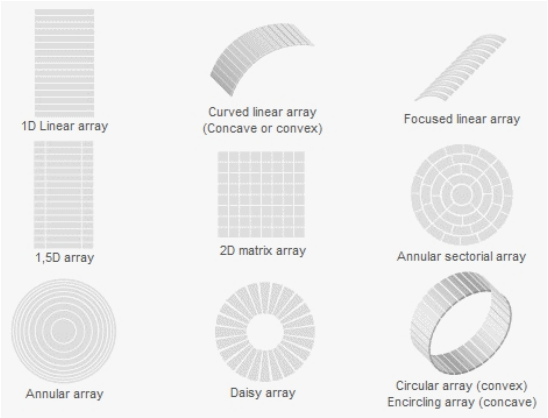

(b) Different element types of phased array probes (Imasonic, 2010).

Figure 5.7: Phased array probes and elements.

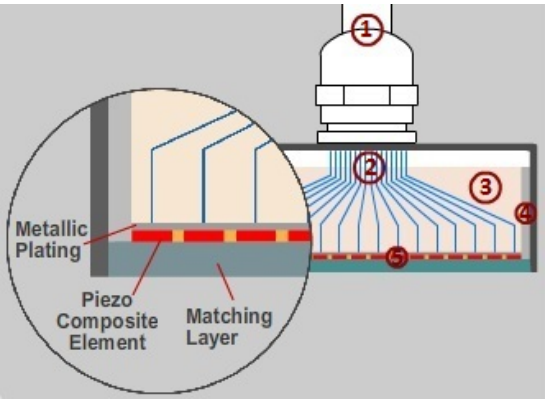

Figure 5.8: Probe cross section. 1) Multi-conductor coaxial cable 2) Element wiring 3) Backing 4) Inner sleeve 5) Piezo composite element (Phased Array Tutorial, 2015).

5.5 Near Field

Since the ultrasound originates from a number of points along the probe face, the ultrasound intensity along the beam is affected by constructive and destructive wave interference. This wave interference leads to extensive fluctuations in the sound intensity near the source and is known as the *near field*.

Consequently, the near field is the range in front of the probe where the sound beam is non-uniformed. In the near field, also referred as *Fresnel field* or *Fresnel zone*, the amplitudes of echo signals from defects can vary significantly and lead to misinterpretation of defect size or location. The near field for circular and rectangular elements can be calculated with Equations (5.23a) and (5.23b), respectively.

$$N_{\text{circular}} = \frac{D^2 f}{4v}, \tag{5.23a}$$

and

$$N_{\text{rectancular}} = \frac{k_{\square} L^2 f}{4v}, \tag{5.23b}$$

where $k_{\square}$ is the near field correction factor, L is the length of the probe and D is the diameter of the probe. Equation (5.23b) assumes that the length of the probe is equal to the width of the probe for phased array probes (Dubé, 2004).

The near field effect is illustrated in Figures 5.9 and 5.10. The near field effect makes amplitude based ultrasonic testing impossible under its length.

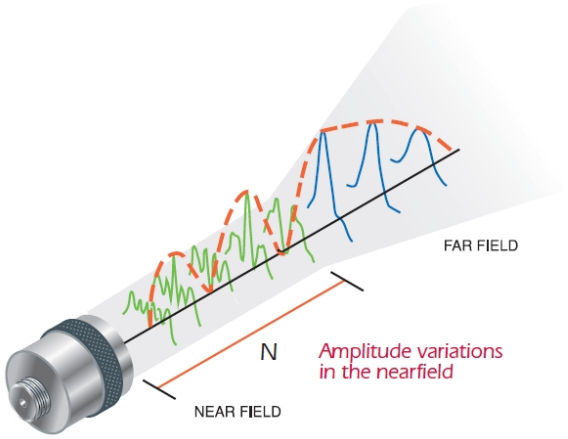

Figure 5.9: Visualisation of amplitude variations in near and far field (Anderson, 2010).

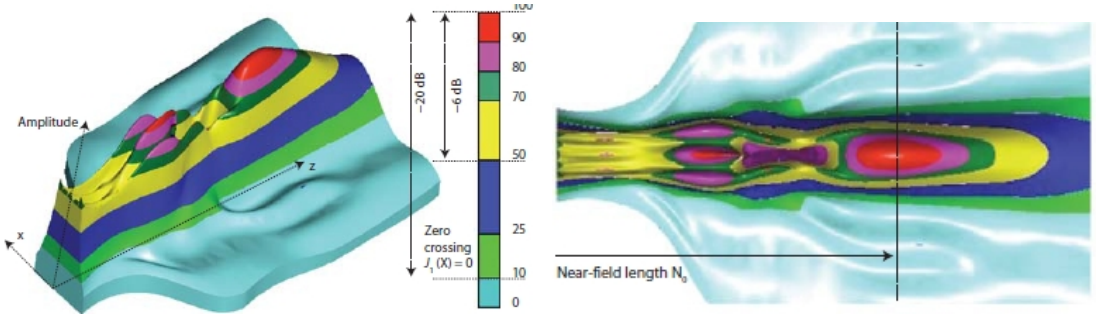

(a) Isometric sound pressure countour.

(b) Sound pressure contour from above.

Figure 5.10: Nearfield contours (Dubé, 2004).

5.6 Ultrasonic Views (Scans)

Ultrasonic views or so called *scans* are different plane views of the scanning data. Scans may be combined on screen to view multiple scans simultaneously. Multiple view is handy in many applications. The basic scans are listed in Table 5.1.

Table 5.1: Scans (Dubé, 2004)

A-scan
B-scan (*side*)
C-scan (*top*)
D-scan (*end*)
S-scan (*sectorial*)
Polar view
Strip chart (*amplitude and/or position*)

All the scans are introduced in Subsections below in the order of Table 5.1.

A-Scan – The A-scan is a one-dimensional representation of received ultrasonic pulse as a function of time-of-flight (ultrasonic path), or a waveform. The a-scan can be thought of as a Cartesian coordinate system where the y-axis gives the amplitude as a percent of screen hight and x-axis gives the time-of-flight. The A-scan is usually presented as bipolar-rectified signal (see Figure 5.11b) but also a RF (radio-frequency) signal presentation is possible (see Figure 5.11c). Bipolar-rectified signal is the basic view type for conventional UT.

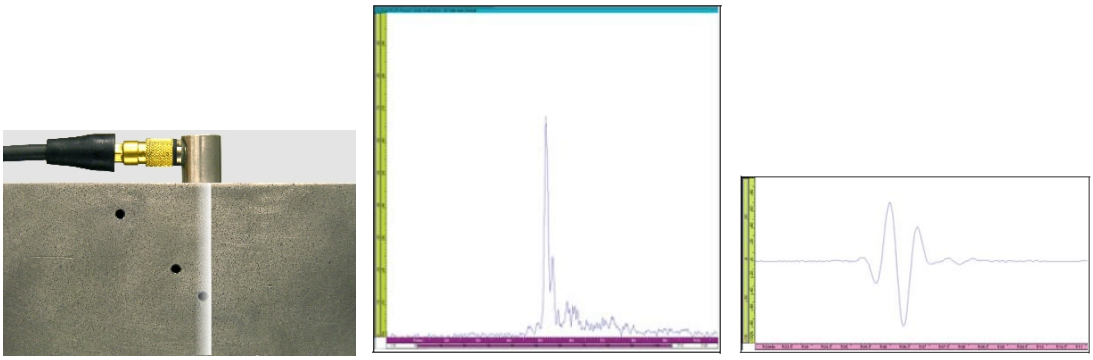

(a) Probe position (Phased Array Tutorial, 2015).

(b) Bipolar-rectified signal (Dubé, 2004).

(c) RF signal (Dubé, 2004).

Figure 5.11: A-scan.

B-Scan – The b-scan is a two-dimensional view of ultrasound data. Usually, in Cartesian coordinate (x,y) system the y-axis can be thought of as the scan position and x-axis the ultrasound path or time. Essentially, a B-scan is a series of stacked A-scans or waveforms. Each A-scan is represented by an encoder/time-base sampling position. B-scan is defined by the depth and probe movement axes. Figure 5.12 illustrates both probe position and received data as s B-scan.

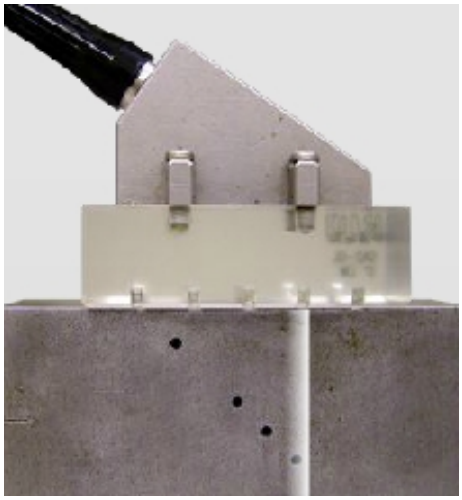

(a) Probe position.

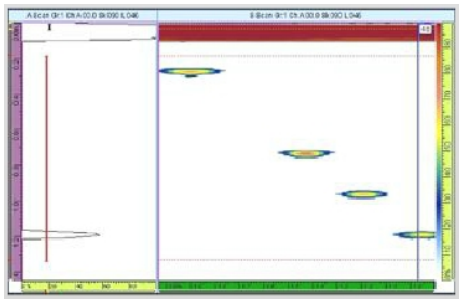

(b) Cross sectional linear scan.

Figure 5.12: B-scan (*side*) (Phased Array Tutorial, 2015).

C-Scan – The C-scan is a two-dimensional planar view of ultrasonic data. One of the axes is the scan and the other is the index. The position of the displayed data is related to the encoder positions during acquisition. The calibration of the encoder is critical in order to locate defects with confidence. The probe is typically moved along one axis while the beam electronically scans the other axis according to the focal law sequence (see Figure 5.13).

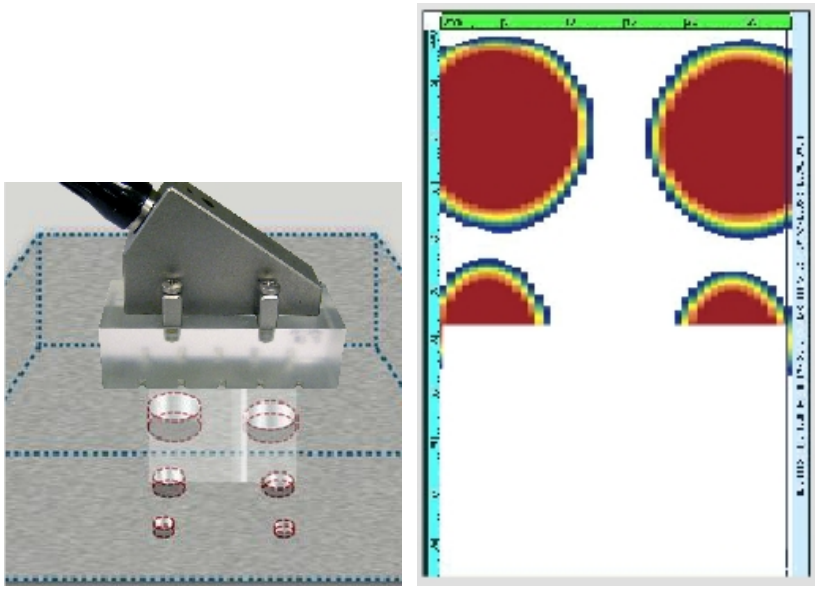

(a) Probe position. (b) C-scan data.

Figure 5.13: C-scan (*top*) (Phased Array Tutorial, 2015).

D-Scan – The D-scan is the right angle view of the B-scan. So if the B-scan is a side view then the D-scan is an end view. The D-scan is defined by the depth and electronic scan axis.

S-Scan – An S-scan is a sectoral two-dimensional view of ultrasonic data where the A-scans has been corrected for delay and refracted angle. The vertical axis corresponds to the depth and the horizontal axis corresponds to the projected distance from the beam exit point for a corrected image (see Figure 5.14).

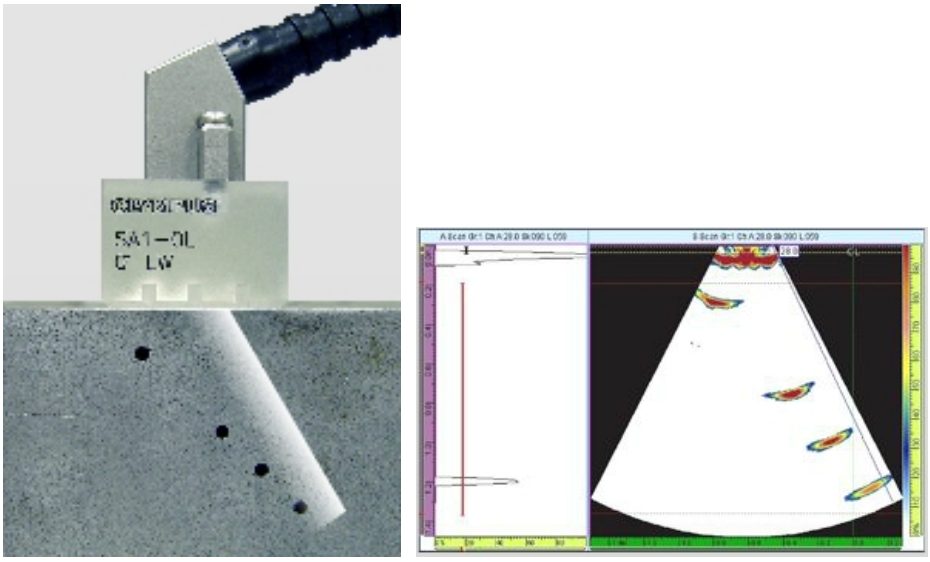

(a) Probe position and scan pattern.

(b) S-scan data.

Figure 5.14: S-scan (*sectorial*) (Phased Array Tutorial, 2015).

Polar View – The polar view is a cylindrical, two-dimensional view shown in Figure 5.15. In conjunction with the 2-D specimen layout, it provides the defect location in inner or outer diameter and angle.

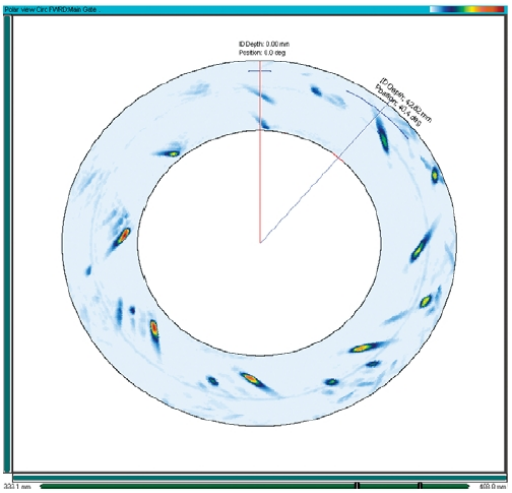

Figure 5.15: Polar view (Dubé, 2004).

Strip Chart – A strip chart is a display of peak signal amplitude in the gate as a function of time, usually for a single channel. In some strip charts, other data such as time-of-flight (or position) is included. Typically, digital strip charts use multiple channels, each displaying the data from specific regions of a weld or other components (see Figure 5.16).

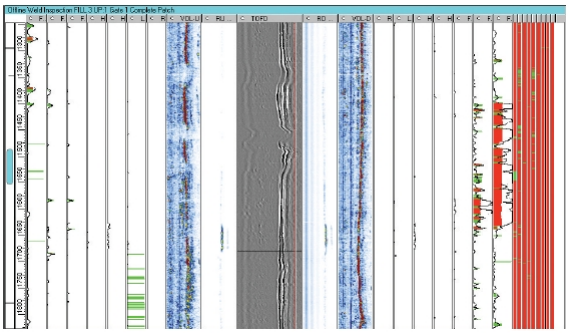

Figure 5.16: Multichannel strip chart. Display uses both amplitude and TOF data, plus couplant checks, TOFD, and B-scans. (Dubé, 2004).

5.7 Inspection of GRP

Standard PSK 6314 – *Industrial Fibre-reinforced Plastic Products. Condition monitoring. Ultrasonic Inspection* describes ultrasonic testing for fiber-reinforced plastics. Recommendations are given for testing parameters, selection of items to be inspected and analysis of test results. A reference measurement is considered mandatory. The information presented in PSK 6314 can be used also in phased array ultrasonic testing.

The frequency of the probe shall be 1-4 MHz for standard laminates. As a minimum requirement, ultrasonic testing is able to reveal wall loss and delamination. See PSK 6314 for further information (PSK 6314, 2011). C-scan may be used for detection of large voids, distribution of fine porosity, areas of variation in fiber, content or delaminations. Moreover, a thickness measurement can be done if the attenuation is not a limiting factor (Harris, 1983).

The GRP is very challenging material for ultrasonic testing. In many cases, composites are highly dispersive, having quite regular structural pattern at several levels of scale (fiber tows, weave of cloth, laminate stacking sequences), many interfaces (fiber-resin interfaces, interlaminar interfaces) and inherent defects (pores, voids, etc.). As a result ultrasonic waves are rapidly attenuated in the GRP and both velocity and attenuation are strongly dependent on frequency. The propagation of ultrasonic waves are affected by frequency, wave length, composite structure, structural defects and damage due to loading. Thus, the need for highly penetrating pulses is mandatory.

In some degree, the problem of high attenuation can be overcome by the use of a broadband, short pulse and low frequency probe with less a pronounced near field interference effect (Harris, 1983). High amplification may be needed although low pulse intensities are used for the GRP inspection. The attenuation limits the testing techniques. Therefore, methods based on multiple reflections are out of question but most of the common ultrasonic techniques can be used.

Equation (5.6a) (see p. 25) requires that in the far field the intensity of a point source falls as the inverse square of a distance. Attenuation due to these diffraction effects is approximately -6 dB for each doubling of the distance. In addition to diffraction due to beam spreading and mode conversion, attenuation occurs due to scattering and absorption. There are several mechanisms of scattering and loss in the GRP. Scattering occurs in interfaces when change in velocity occurs due to difference in acoustic impedance. Individual fibers and fine porosity are small enough for them to act as scattering center. Loading defects also cause attenuation in the GRP. Some energy loss occurs between surfaces of small cracks through friction. In carbon fiber composites, delaminations, debonded interfaces or distribution of fine resin pores all scattered affect strongly on attenuation and it was found to be as high as 40 dB/mm (Harris, 1983).

The problem of attenuation and matching can be overcome in some degree by selecting a proper *delay line* for the phased array probe that is closely matched to the GRP. Teflon and PUR were found good enough for the testing purposes.

6 Zero Interface Probe Ultrasonic Testing Theory

Zero interface probe ultrasonic testing (ZIP UT) relays, to a large extend, on the same physical principles as the phased array ultrasonic testing described in Sections 5.1 and 5.2. The two fundamental differences between the ZIP UT and PAUT are probe assembly and *delay line*. Zero interface probe contains just one element. Consequently, wave bending, steering and focusing of ultrasonic energy is not possible and only A-scan is useful for the inspection data visualization . However, what makes the ZIP UT extremely useful for the GRP and composite inspections is the special delay line. The delay line is matched to most composites and guides the maximum amount of acoustic energy into the composite without loss of energy in the delay line-composite interference due to reflection.

As the basic principles are already introduced before, this Chapter begins directly with the description of the delay line in Section 6.1. Understanding the fundamental principle of the delay line will help to understand the main challenges of the ultrasonic testing for the composites. Section 6.2 deals with the inspection of GRP. Available testing standard is introduced and the characteristic of the zero interface probes are discussed.

6.1 Delay Line

Delay line is material used between the probe and inspected object. ZIPs contain a delay line that is acoustically matched to most composites. Therefore, the maximum amount of acoustic energy is transferred to the target (reflection coefficient tends to zero in Equation (5.9) see p. 25) and the dead zone from the delay tip is minimized (GE Inspection Technologies, 2008).

The meaning of matching due to delay line is shown in Figure 6.1. Subfigure 6.1a proves nearly perfect matching between the delay line and the GRP. Thus, the maximum amount of ultrasonic energy is propagated into the GRP and one back wall echo is obtained. In general, only one back wall echo is visible when testing GRP. Subfigure 6.1b shows that ZIP is not matched to iron (huge delay line echo) and only a small part of the ultrasonic energy is penetrated into iron. However, ultrasound propagates in iron with little attenuation compared to the GRP and many back wall echoes are obtained. Subfigure 6.1c demonstrates the delay line echo when the probe is held in mid-air and obviously no matching is achieved.

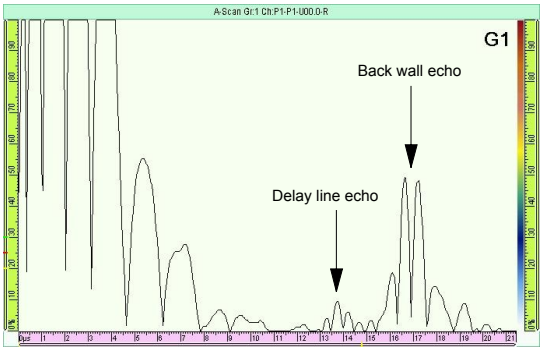

(a) Delay line echo when probe is in contact with the GRP. Nearly perfect maching is achieved.

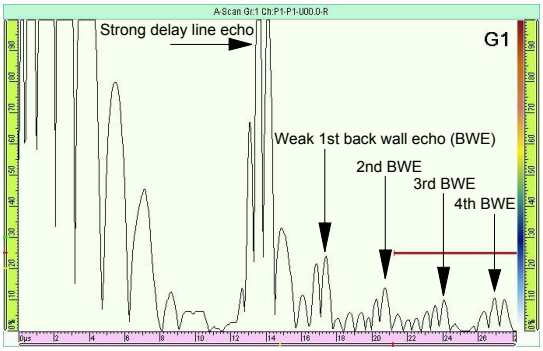

(b) Delay line echo and back wall echoes when the probe is in contact with iron.

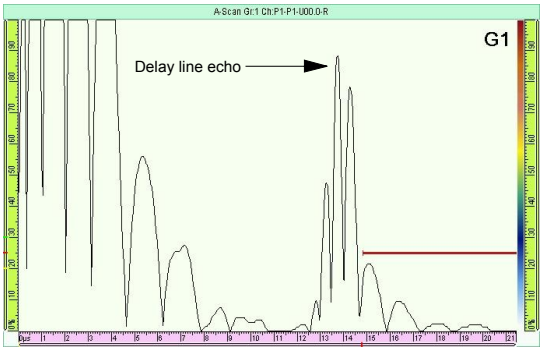

(c) Delay line echo when the probe is held in mid-air.

Figure 6.1: ZIP delay line echo.

In all Figures, x-axis is the time-of-flight (t). True depth (d) may be calculated by solving d from Equation (5.17) as follows

$$d = 2v(t_{\text{echo}} - t_{\text{delay line echo}}). \tag{6.1}$$

6.2 Inspection of GRP

Standard PSK 6314 – *Industrial Fibre-reinforced Plastic Products. Condition monitoring. Ultrasonic Inspection* discussed in Section 5.7 is also used for ZIP UT purposes.

Zero Interface Probes (ZIP) are broadband UT probes engineered especially for manual inspection of composites. The zero interface probes *solve* the main problem concerning ultrasonic testing for composites, the matching. Hence, although ultrasonic energy attenuates in the GRP, one back wall echo is obtained. The ZIPs are highly damped for high resolution and sharp A-scan image. Moreover, the characteristics of

the ZIPs also include high penetration due to low frequency and very high near surface resolution. The ZIPs can be applied for many smooth surface materials without couplant because delay line tend to adjust to the surface providing adequate contact (GE Inspection Technologies, 2008).

7 Digital Radiographic Testing Theory

Conventional radiography (RT) is one of the longest established NDT methods used for volumetric inspections. It reveals defect types such as thickness variations, various internal and surface defects, changes in structure and assembly details, to name few. Digital radiography (DRT) includes all the pros than conventional one and furthermore adding the capacity with computer-aided image developing, processing and analysis tools. The quality of the inspection images can be checked on-site. Neither film, film processor, darkroom nor chemicals are needed to produce image. Therefore both inspection and analysis is faster than with conventional RT (de Raad, 2008). However, the physical principles of electromagnetic radiation are universal and not dependent on the method. The knowledge of electromagnetic radiation will be important for being able to apply digital radiographic testing to composites such as the GRP. Generally speaking, the DRT is based on the penetration and attenuation of the X-rays. The attenuation is constant in terms of homogeneous structure where as discontinuities are indicated either stronger or weaker X-ray energy on the indicator.

The DRT relies on the propagation and attenuation of X-rays. The first Section 7.1 (see p. 43) deals with the important physical X-ray properties and the second Section 7.2 (see p. 49) introduces the phenomena of attenuation which can be expressed as exponential absorption of the X-rays. Section 7.3 (see p. 50) gives special insight to the computer aided digital radiographic testing. Finally, special attention of the DRT for the GRP is given in Section 7.4 (see p. 51)

7.1 X-ray Properties

X-rays are electromagnetic radiation, just as *gamma-rays*, *microwaves*, light and infrared radiation for instance. Figure 7.1 illustrates the electromagnetic spectrum of interest in terms of the DRT.

Electromagnetic radiation	Wavelength λ	m	Type
	10 μm	10^{-5}	Heat-rays, Infra-red rays, microwaves
	1 μm	10^{-6}	
X-ray energy	100 nm	10^{-7}	Visible light and Ultraviolet (UV)
100 eV	10 nm	10^{-8}	
1 keV	1 nm	10^{-9}	
10 keV	0.1 nm	10^{-10}	
100 keV	0.01 nm	10^{-11}	X-rays and Gamma-rays (Radiography)
1 MeV	1 pm	10^{-12}	
10 MeV	0.1 pm	10^{-13}	
100 MeV	0.01 pm	10^{-14}	

Figure 7.1: X-rays and electromagnetic spectrum (de Raad, 2008).

X-ray tube emits *heterogeneous radiation*. Heterogeneous radiation contains a continuous spectrum of many wavelengths with some superimposed spectrum lines (see Figure 7.2).

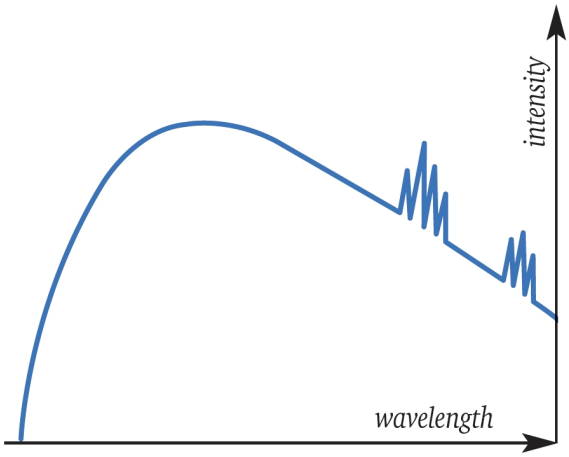

Figure 7.2: X-ray spectrum – intensity as a function of wavelength. Two small local maxima groups represent the characteristic radiation of the target material (de Raad, 2008).

The energy of the X-ray radiation is given by the *Planck relation*

$$E = hf, \tag{7.1a}$$

and by substituting Equation (4.4) (see p. 14), we have

$$E = \frac{hc}{\lambda}. \tag{7.1b}$$

Two distinct processes are involved in the X-ray emission. The first process is called *bremsstrahlung* (*"braking radiation"*). In the bremsstrahlung process some of the emitted electrons are stopped or decelerated by the target. The *kinetic energy* is converted partially or completely to a continuous spectrum of *photons*, including X-rays. The bremsstrahlung is illustrated as the continuous parts of the curve in Figure 7.2 (see p. 44). In the creation of X-rays, a large *potential difference* V_{AC} is used to accelerate electrons from *cathode* towards *anode* or target, gaining velocity of v (see Figure 7.3). An electron has a charge of $-e$ and mass of m_e. Due to external potential difference V_{AC} electron gains kinetic energy

$$E = \frac{1}{2} m_e v^2 = eV_{AC}. \tag{7.2a}$$

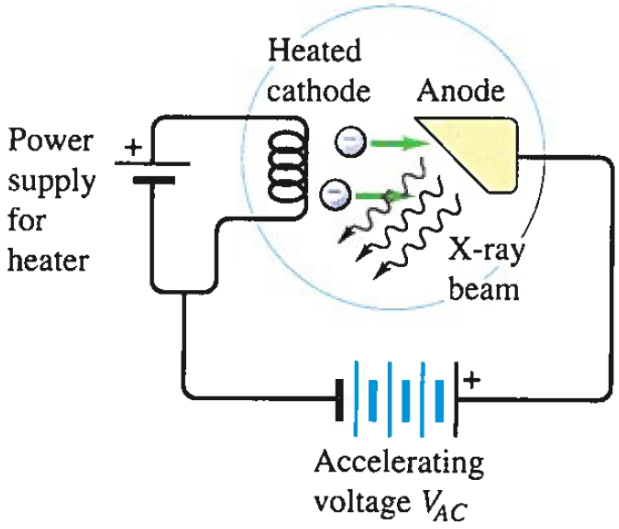

Figure 7.3: Schematic illustration of an apparatus used to produce X-rays. Electrons emitted from the heated cathode are accelerated toward anode. X-rays are produced when they strike to anode (Young and Freeman, 2008).

The most energetic X-ray photon is produced when all the kinetic energy of electron goes to its production. Substituting Equations (7.1a) and (7.1b), we get the *bremsstrahlung limits* (Young and Freeman, 2008)

$$eV_{AC} = hf_{max} = \frac{hc}{\lambda_{min}}. \tag{7.2b}$$

The shortest wavelength of the X-ray spectrum (see Figure 7.2 on p. 44) is given by the *Duane-Hunt law* (de Raad, 2008)

$$\lambda_{min} = \frac{hc}{eV} = \frac{1,234}{V_{AC}\ [\mathrm{kV}]}\ [\mathrm{nm}], \tag{7.2c}$$

note that f_{max} and λ_{min} do *not* depend on the target material in the X-ray tube.

The second process gives the *characteristic X-ray spectrum* for the target element for frequencies and wavelengths that *do* depend on the target material. These sharp peaks are shown in Figure 7.2 (see p. 44). Electrons that have enough kinetic energy can excite atoms within target. When atoms decay back to their ground level they may emit an X-ray photon that has a certain amount of energy. Since each material has unique set of atomic energy levels, each has a characteristic X-ray spectrum. (Young and Freeman, 2008)

Atomic Structure – All matter consist of atoms. According to *Bohr model* an atom may be simplified to central *nucleus* and electrons revolving around it. Elementary particles: *neutrons* and *protons* form the nucleus. Protons have positive

elementary electric charge +1 e, neutrons are neutral and electrons have negative elementary electric charge -1 e.

Atomic number (Z) indicates the place of the element in the *Periodic Table of Elements*. Atomic number is quantified as the number of protons in the nucleus.

A *shell* is a defined orbit that the electrons occupy. Shells are labelled K, L, M, N etc. from the closest to the nucleus. The maximum number of electrons able to occupy a certain shell is predefined by quantum mechanics. Only 2 electrons can occupy K-shell but for the O-shell it is 50 for instance. If an electron is removed from the shell by external energy, a positive *ion* results.

Electron Binding – The electrons are bound to the atom by what is called their *Binding Energy* E_b. This is strongest for the K-shell and gets weaker the further an electron is from the nucleus. K-shell binding energies increase with the atomic number of the nucleus.

Interaction Processes

Attenuation is caused by the interaction processed described below. In detail discussion of attenuation is given in Section 7.2.

Photoelectric Effect – Incident photon or X-ray photon of energy E_0 transfers its *total* energy to an electron. Low energy X-ray photon can only move the electron from one shell to another (Bryant and McIntire, 1985). The energy of the incident X-ray photon is the difference between the the binding energies of the higher energy shell $E_{b,h}$ and the lower energy shell $E_{b,l}$

$$E_0 = E_{b,h} - E_{b,l}. \tag{7.3}$$

However, a high energy X-ray photon may have sufficient energy to *ionize* the atom. In the ionization, the electron is completely removed from the atom (see Figure 7.4) (Bryant and McIntire, 1985). The kinetic energy of the ejected electron E_e is the difference between the incident photon energy E_0 and the binding energy of that certain electron in the atom E_b

$$E_e = E_0 - E_b. \tag{7.4}$$

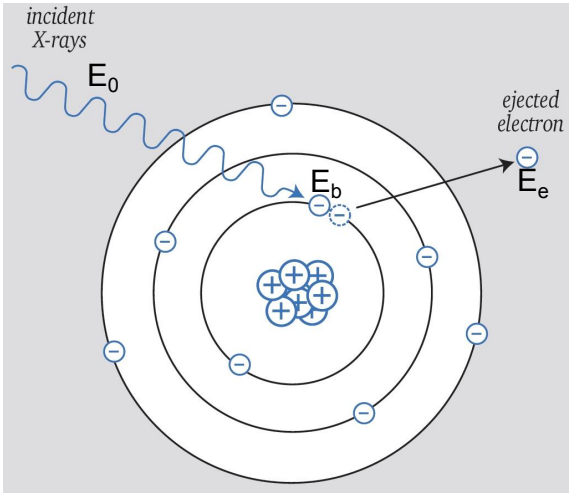

Figure 7.4: Photoelectric effect of an incident X-ray photon with an orbital electron (de Raad, 2008).

Compton Scattering – In *Compton scattering*, an incident x-ray photon collides with an electron, sharing a part of its energy with the struck electron. Consequently, some of the X-ray radiation is *scattered* (see Figure 7.5). Compton scattering is a direct confirmation of the quantum nature of X-rays and cannot be explained by classical electromagnetic theory.

Concerning the particle properties of a photon and the conservation of energy

$$E_0 - E_{e,r} = E_s + E_e, \tag{7.5a}$$

and the conservation of momentum during the collision

$$\vec{p_0} = \vec{p}' + \vec{P_e}, \tag{7.5b}$$

the law for Compton scattering can be derived (Young and Freeman, 2008)

$$\lambda - \lambda' = \frac{h}{m_e c}(1 - \cos\phi), \tag{7.5c}$$

where m_e is the electron rest mass. Used symbols are illustrated in Figure 7.5.

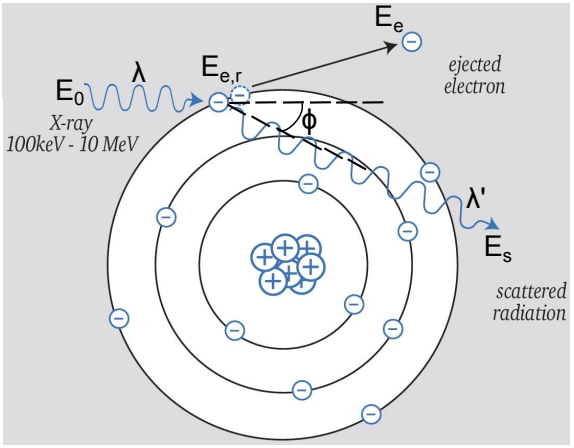

Figure 7.5: Compton scattering (de Raad, 2008).

Pair Production – The process in which a high energy photon is converted in the electric field of a nucleus into both an electron and a *positron* (see Figure 7.6). The minimum energy of the incident threshold X-ray photon is

$$E_{0,min} = 2m_e c^2 \approx 1,02\,\text{MeV}, \tag{7.6a}$$

that is the energy corresponding to the creation of the masses of the two particles. Taking into account the kinetic energies of the electron and positron, the energy of the incident X-ray is

$$E_0 = E_+ + E_- + 2m_e c^2. \tag{7.6b}$$

Pair production may also occur in the field of an orbital electron. In this case it is sometimes referred as *triplet production* (Bryant and McIntire, 1985).

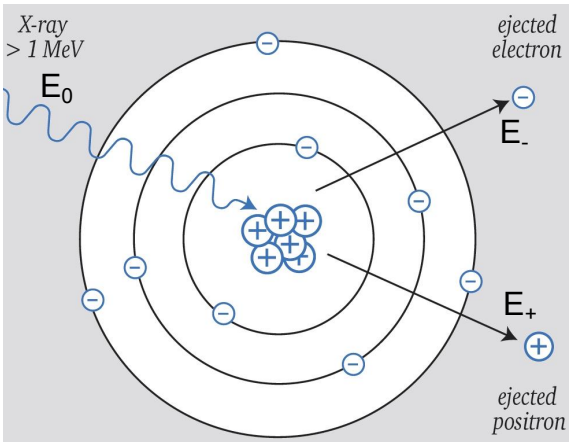

Figure 7.6: Pair production (de Raad, 2008).

Coherent Scattering – In terms of classical physics, *coherent scattering* or *Rayleigh process* occurs when the electrons of an atom are set into oscillation by the absorption of the incident photon and the photon does not experience energy shift. The electrons act as a *common source* for the emitted photon if the same frequency as the incident photon (Bryant and McIntire, 1985).

Photodisintegration – A *nuclear reaction* in which the absorption of high-energy photon causes the absorbing nucleus to change to another species by ejecting a subatomic particle, such as a proton or neutron for instance (Bryant and McIntire, 1985).

7.2 Attenuation of X-Rays

The interaction processes (see Section 7.1) causes exponential absorption of X-rays in its passage through matter, assuming narrow-beam geometry and the fact that usually a single even (one of the interaction processes) removes photon from the beam.

Removed photons may be expressed as

$$\mathrm{d}I(x) = -I(x)\, n\sigma_A\, \mathrm{d}x, \tag{7.7a}$$

and integration of Equation (7.7a) results in

$$I(x) = I_0 e^{-n\sigma_A x} = I_0 e^{-\mu x}. \tag{7.7b}$$

Here I_0 is the initial intensity of the incident X-ray beam, σ_A is the *total attenuation coefficient* and μ is the *linear attenuation coefficient*. The number of atoms per cubic centimeter can be calculated

$$n = \frac{N_A \rho}{A}, \tag{7.7c}$$

where N_A is the *Avogadro's number* and A is the *atomic weight* of the absorption material.

Total attenuation coefficient is the sum of all the attenuation coefficients of the different interaction processes

$$\sigma_A = \sigma_{ph} + \sigma_{com} + \sigma_{coh} + \sigma_{pr} + \sigma_{pd}, \tag{7.7d}$$

where σ_{ph} is the attenuation coefficient of photoelectric effect, σ_{com} Compton scattering, σ_{coh} coherent scattering, σ_{pr} pair production and σ_{pd} photodisintegration.

Half-Value Layer – $t_{1/2}$ is defined as the needed thickness of the material that reduces the intensity of the initial incident X-ray beam by 50 %. Under the con-

ditions of narrow-beam geometry, a mono-energetic (*homogeneous*) beam of photons and using Equation (7.7b) we can write

$$I(t_{1/2}) = \frac{1}{2} I(t_{1/2}) e^{-\mu t_{1/2}}. \tag{7.8a}$$

Solving Equation (7.8a) for the half-value layer, we have

$$t_{1/2} = \frac{\ln 2}{\mu} \approx \frac{0,693}{\mu}. \tag{7.8b}$$

Note that μ is given in *reciprocal* millimeters and then $t_{1/2}$ will be given in millimeters.

The x-rays penetrate the GRP structures easily with little attenuation. Thus, a radiation hardness must quite soft. A fairly soft hardness (60-150 kV) is adequate for the GRP plates and plates. The radiation hardness is categorized according to the used x-ray tube voltage. Soft hardness equals to the tube voltages under 150 kV, where as hard radiation equals to the voltages above 150 kV and >3000 kV equals to ultra hard radiation.

For a heterogeneous X-ray beam the half-value layer is not constant. The second half-value layer is slightly thicker than the first. However, relatively *hard* radiation is used. As a result, a fixed half-value layer is applied (de Raad, 2008).

Atomic Number Dependence – The atomic number Z has a significant effect on the magnitude of the total attenuation coefficient: Z for Compton scattering, $Z(Z+1)$ for pair production and between Z^4 and Z^5 for photoelectic effect. The contribution of coherent scattering is always smaller that 20 %. The effect of photodisintegration is only a few percentages.

7.3 Digital/Direct Radiography

A computer controlled inspection system is used to direct x-ray radiation through the inspection object to a flat panel radiation detector or so called imager. Flat panel detector converts the radiation into a digital information that can be viewed directly with a laptop The DRT provides near real-time inspection capacity as the flat panel exposure and image formation happen simultaneously and the digital image can be seen from the laptop screen (de Raad, 2008).

The main advances of digital radiography are listed in Table (7.1).

Table 7.1: The DRT advantages (de Raad, 2008).

Shorter exposure time to ionizising radiation
Faster image convertion
No chemicals, thus no encironmental pollution
Flat panel detectors can be used repeatedly
Fewer imaging retakes

Commonly used flat panel detectors use amorphous silicon technology. The flat panel converts the individual radiation photons into light. Light conversion is proportional to the radiation dose. A structured cesium iodide photodiode based scintillator and integrated thin film transistors make the conversion from light into electric signal. Figure 7.7 demonstrates the different active layers of a flat panel detector and their principles on converting photons into electrons and digital data.

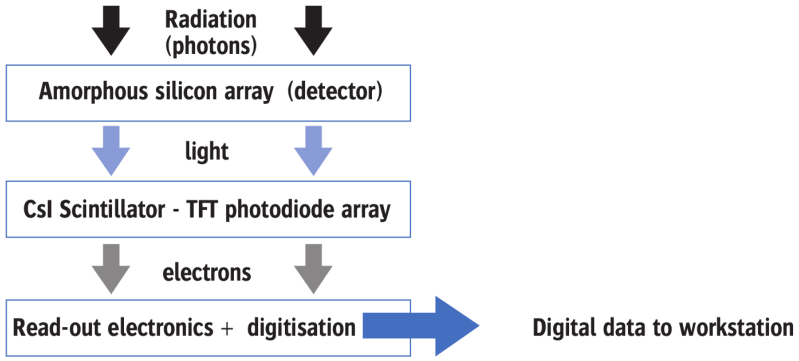

Figure 7.7: The conversion principle of a two-stage flat panel detector (de Raad, 2008).

7.4 Inspection of GPR

Standard PSK 6313 – *Industrial Fibre-reinforced Plastic Products. Condition monitoring. Radiographic Inspection* – introduces radiographic testing for fiber-reinforced plastics. Recommendations are given for testing parameters, selection of items to be inspected and analysis of test results. A reference measurement is considered mandatory.

Radiographic testing is suitable for pipes with outer diameter up to ≤ 300 mm if it's filled with water or similar liquid. The content of the pipe will deteriorate the image quality and sensitivity to detect defects because harder radiation is needed. The goal of the DRT is to get an image of the pipe profile whenever possible. The pipe profile is the most informative data in case of delamination and wall thickness variation.

The recommended focal spot is $\leq$ 3,0 mm, for inspection of cracks it is $\leq$ 1,0 mm. The source-to-detector distance should be approximately 750 to 1200 mm, but at least four times the outer diameter of the pipe to be inspected. By averaging overlapped images, signal to noise ratio can be improved in order to inspect small defects. Detectable defects are wall loss, cracks penetrated to the support layer, changes in protective layer caused by corrosion and many of the manufacturing defects (PSK 6313, 2011).

8 Equipment and Methods

All GRP test blocks were made of E-glass and their matrix was vinyl ester. Throughout the rest of the text, referring to A-side means the outside surface of the pipes. A-side surface roughness is much greater than in the B-side (inside surface of the pipes) and it is also more fuzzy. Surface roughness of the A-side of the testing blocks varied between 2,00 μm and 13,87 μm. Surface roughness of the B-side varied from 0,65 μm to 1,42 μm. This indicates that phased array ultrasonic testing should be carried out from the B-side for plates when ever possible. However, a good results were obtained from both surface sides. On the other hand, proper contact between small diameter (<100 mm) pipes and the probe was somewhat hard to achieve.

This Chapter begins with a demostration of the calibration blocks, plates, pipes and pipes removed from service in Sections 8.1, 8.2, 8.3 and 8.4, respectively. Second, wall thickness' and pipe diameter of the test blocks are presented in 8.5. Moreover, the acoustical characteristics are shown. Finally, the NDT equipment - the infrared camera, zero interface probe, phased array instrument and digital radiography system - are demostrated and introduced in Sections 8.6, 8.8, 8.7, 8.9, respectively.

8.1 Calibration Blocks

All composite structures have different properties. That's why the results of research are case-sensitive and *not* directly valid for all composite structures although they may give insight to the inspection of other composites. Calibration blocks are mandatory for reliable and accurate nondestructive testing and the calibration block shall be studied before the actual decision for reliable NDT can be made for composite structures. The calibration plates used here were manufactured by Plastilon Oy and the defects were produced by Inspecta Oy. Calibration plates are introduced in Figure 8.1 . Plate R_GRP_1_A_S3 is similar to R_GRP_1_A_S2, except the side of the flat bottom bores is opposite, thus it is not seen in the Figure 8.1.

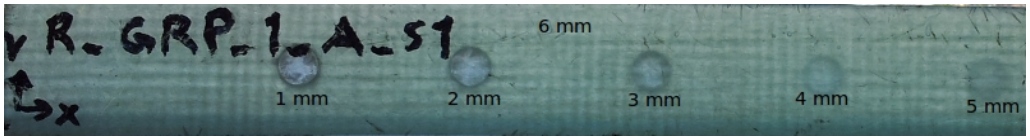

(a) R_GRP_1_A_S1 A-side. Nominal wall thickness seen in the upper- center is 6 mm. The other measurements 1 mm–5 mm indicate the wall thicknesses above the flat-bottom bore. The diameter of the flat-bottom bores is 12 mm.

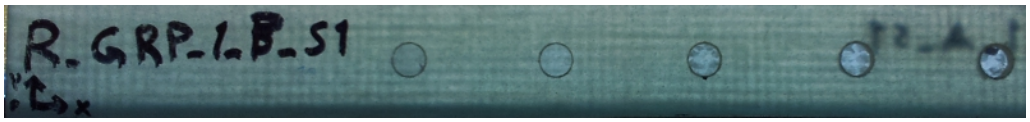

(b) R_GRP_1_B_S1. Flat-bottom bores from the B-side.

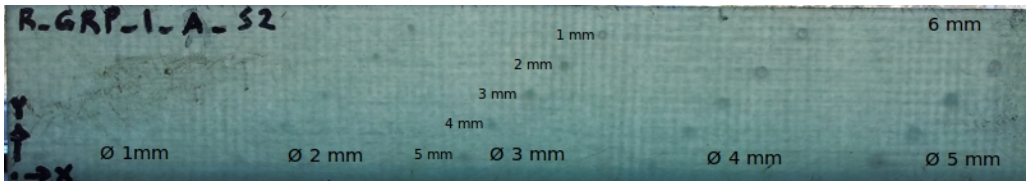

(c) R_GRP_1_A_S2. A-side. Nominal wall thickness seen in the upper-right corner is 6 mm. ⌀ symbol indicates the diameter of the flat-bottom diagonal bores. Diagonal values indicate the wall thicknesses above the diagonal bores.

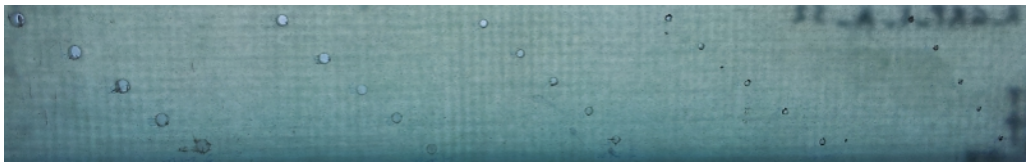

(d) R_GRP_1_B_S2 B-side.

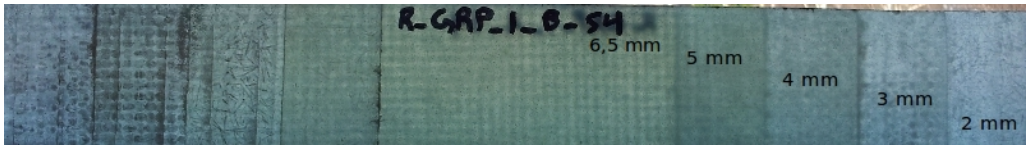

(e) R_GRP_1_B_S4 step plate is used for PAUT and ZIP UT thickness calibration. Marked values indicate the thicknesses of each stripes.

Figure 8.1: Calibration plates.

8.2 Plates

New plates (see Figure 8.2) were manufactured by Plastilon Oy to contain delamination. Afterwards, impact damages, wall losses and major cracks were fabricated at Inspecta Oy. Infrared thermography also revealed air bubbles in P_N_GRP_2.

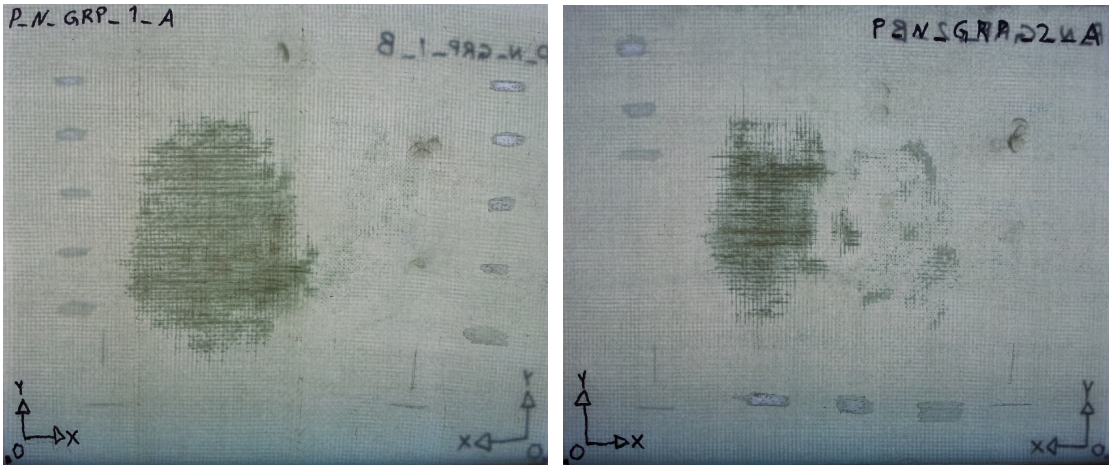

(a) P_N_GRP_1_A. (b) P_N_GRP_2_A

Figure 8.2: New test plates.

8.3 Pipes

New pipes (see Figure 8.3) were manufactured by Plastilon Oy to contain delamination. Afterwards, impact damages, wall losses and major cracks were fabricated at Inspecta Oy. Infrared thermography also revealed air bubbles in N_GRP_2.

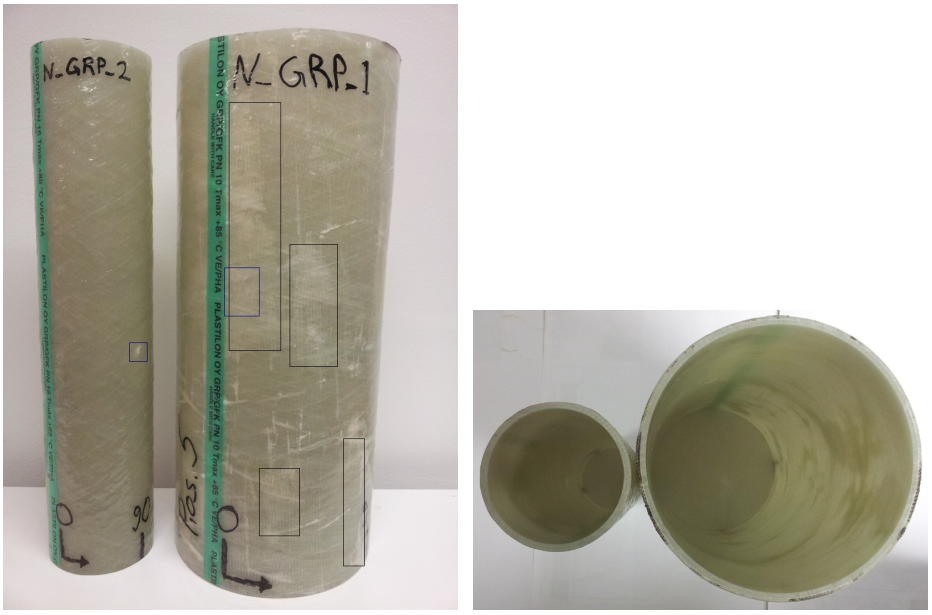

(a) Delamination is marked with black rectangles and impact damage is marked with blue rectangles.

(b) N_GRP_1-2 from the top.

Figure 8.3: New test pipes.

8.4 Pipes Removed from Service

Sulmu Oy delivered pipes removed from process industry's service (see Figure 8.4 on p. 56). Impact damages, wall losses and cracks were fabricated at Inspecta Oy.

(a) U_GRP_1-5 from the front.

(b) U_GRP_1-3 from the top. Loose glass fiber due to inner wall loss.

Figure 8.4: Test pipes removed from service.

8.5 Characteristics of GRP

Glass content, lay-up etc. have quite a small effect on normal to reinforcement (through-thickness) velocities of common composites (Harris, 1983). Summary of calculated and measured ultrasonic characteristics of calibration plates are shown in Table 8.1.

Table 8.1: Ultrasonic characteristics of GRP

Material	Density ρ	Velocity v	Impedance Z
	$\mathrm{kg/m^3}$	$\mathrm{m/s}$	$10^6 \frac{kg \cdot m}{m^3 \cdot s}$
N_GRP	1470	2700	4,0
U_GRP	1590	2610	4,1

Wall thickness and pipe diameter can play an important role as testing parameters. Summary of wall thickness and pipe diameters are shown in Table 8.2.

Table 8.2: Thicknesses and diameters of GRPs

Block	Thickness t	Diameter D
	mm	mm
P_N_GRP_1	5,5	
P_N_GRP_2	3,5	
N_GRP_1	6,5	200
N_GRP_2	5,5	100
U_GRP_2	4,3	150
U_GRP_3	4,1	150
U_GRP_4	5,5	60
U_GRP_5	12	80

8.6 Infrared Thermography

Experiments in infrared thermography were made with the Infrared camera shown in Figure 8.5. The IR camera was manufactured by FLIR and its model was FLIR T425. Table 8.3 consists of some important FLIR T425 specifications.

Figure 8.5: FLIR T425 IR camera.

Table 8.3: FLIR T425 specifications (FLIR T425 Technical Data, 2011)

Manufacturer	FLIR SYSTEMS
Model	T425
Object temperature range [°C]	-20 . . . +1200
IR resolution [px]	320×240
Thermal sensitivity [°C]	0,05
Digital camera [Mpx]	3,1

Used heating sources were a 1000 W infrared heater and a 1600 W resistive heater.

The testing method used was so called active thermography. In active thermography, an external heating source is used to heat the target to be inspected. The distribution of heat is then studied with the IRT camera. Nonetheless, some images of passive thermography are given in Appendix B (see p. 78) for illustrative purposes. In passive thermography, no external heating source is used.

Infrared camera setting were set as follows. Distance was between 0,3 m and 1,2 m. Emissivity was set to 0,95 which is the recommended value for the GRP in Standard (PSK 6316, 2009). Reflected and atmospheric temperatures were set to 29,8 °C.

Afterwards, images were processed with FLIR Reported 8.5.

8.7 Phased Array Instrument

The phased array ultrasonic testing was done with the phased array instrument shown in Figure 8.6. The instrument was manufactured by Olympus and its model was OmniScan MX. Table 8.4 (see p. 59) contains important OmniScan MX specifications.

The phased array matrix probe was manufactured by Zetec. Its model was 1.5-M-5X3-E-17.5-9. Specifications of the phased array probe can be read from the model marking as follows. Frequency was 1,5 MHz, M stands for matrix prove, 5×3 means the number of element rows and columns and the dimension of the active layer was 17,5 mm $\times$ 9 mm.

Polytetrafluoroethylene (PTFE) or *Teflon* in colloquial language and polyurethane (PUR) were found to serve as adequate delay lines. Piece of teflon or polyurethane was used between the probe and the GRP to achieve sufficient acoustic matching.

Glycerol and industrial ultrasonic gel were used as couplants. The thicker couplant layer was needed for pipes to obtain adequate contact. Therefore, industrial ultrasonic gel was found to be better for pipes.

The testing method used was so called pulse–echo-technique. Pulse–echo-technique is based on studying of the reflected echoes from interfaces or defects. Same probe was used to transmit and receive the signal. Calibration plates (see Figure 8.1 on p. 54) were used to calibrate OmniScan MX. OmniScan MX settings were matched to PA probe.

Figure 8.6: OmniScan MX phased array instrument.

Table 8.4: OmniScan MX specifications (Dubé, 2004)

Manufacturer	Olympus
Integrated motor control	No
Number of ultrasonic channels	16/128
Axis support	2 semiautomatic
Portability	Yes

8.8 Zero Interface Probe

The zero interface probe used in the inspection was manufactured by Krautkramer. Its frequency was 1,25 MHz and diameter was 20 mm. The ZIPs differ from one another by frequency and size (see Figure 8.7). Similar testing method, calibration procedures and instrument were used as in the PAUT.

Industrial ultrasonic gel and glycerol were used as couplants. Industrial ultrasonic gel was found to be a better couplant especially for pipes.

Figure 8.7: Zero interface probes. Special delay lines are seen as black cylindrical–shaped blocks in the front of the probes faces (GE Inspection Technologies, 2006).

8.9 Digital Radiography

The main components of the foX-Rayzor system are an Amorphous Silicon (a-Si) flat panel (Imager), and its Imager Control Unit (ICU), connected by 50 m of cable to a laptop (CDU – Control and Display Unit) and an X-ray source. Inspection is done as shown in Figure 8.8, where the imager is directly behind the target. The whole inspection process is controlled by the CDU, a safe distance away. The CDU includes FlatFox software that is used for graphing x-ray images, displaying and enhancing x-ray images and managing the database. However, Vidisco Image Viewer and ImageJ are excellent freeware options for modifying the x-ray images and are used in this special assignment.

Three main testing parameters, exposure time, voltage and current are easy to adjust because the DRT takes only a few seconds for glass-fiber reinforced plastics. These parameters are given in detail in the tables of Section E.5.

Testing parameters were adjusted so that reference intensity curve (see Section E.6 on p. 117) settled between 40 % and 45 %. The distance between the radiation source and the target was always 1 m.

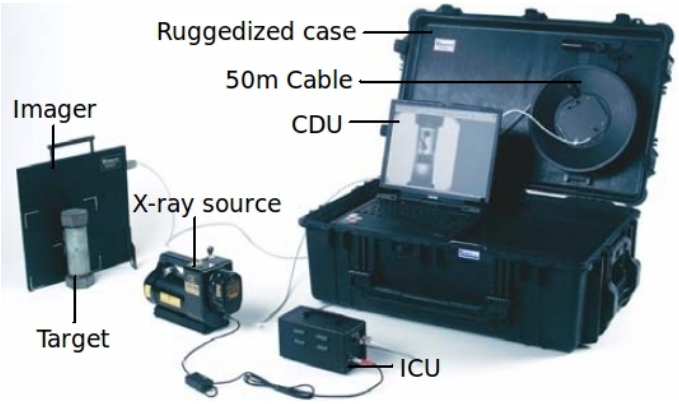

Figure 8.8: foX-Rayzor digital x-ray system.

In the DRT, the pipes were inspected through both walls. In other words, the X-ray source was in front of the target and the imager was behind the target (see Figure 8.8). The distance between the target and the x-ray source was 1 m. The exposure times, voltages and currents used here are presented in Section E.5 (see p. 116).

9 Results

This Chapter describes the results of each used NDT technique. All the actual inspection data is presented as illustrative image banks in Appendices.

9.1 Visual Testing

The resolution for visual testing is smaller than 1 mm in diameter if inspected from the defected side. Otherwise the resolution is considered to be 2 mm in diameter.

Wall losses, major cracks, impact damages, delamination and air bubbles are all detected visually. Cracking of the matrix due to impact damage is the most difficult to detect. Whiter area under the cracking is delamination. Cracking is completely undetectable from the outside surface. However, the size of the impact damage and delaminated area may indicate the severity of the cracking.

As time passes, the GRP begins to turn yellow and obviously, more non-translucent. Still, impact damages, delamination and loss in wall thickness can be detected but the actual type of the defect should be confirmed by the other NDT techniques.

Inspection data is presented as an image bank in Appendix A (see p. 70) which begins with the inspection of calibration plates (see Section A.1 on p. 70). Section A.2 (see p. 71) deals with the VT for plates. Section A.3 (see p. 72) gives the testing results for pipes.

9.2 Infrared Thermography

Image quality and thus, the testing resolution depends on the shooting distance. The shorter the distance, the smaller defects can be detected. From the A-side the resolution is found to be 4 mm and the resolution for depth change is 1 mm. From the B-side the resolution is found to be 1 mm and the resolution for depth change is 1 mm. Therefore, heating is to be done from the other side of the defects and the IRT is to be done from the defected side whenever possible.

Air bubbles are clearly visible as colder areas as well as delaminations. The force of the impact damage must be strong enough to create delamination. Therefore, only strong impact damages are detected as circular delaminated areas.

A stabile temperature decreases the inspection resolution significantly as defects and defectless areas begin to equalize into the same temperature

When a uniform heat flux is supplied, anomalous variations in temperature distribution are indications of structural defects. Uniform heat flux has been shown to be an important testing parameter (Lähteenmäki, 2011). The infrared heater and resistive

heater were found to be good, uniform heating methods. Moreover, the small size of the infrared heater (115×7×4,8 cm) gives the possibility to inspect small diameter pipes across long lengths.

Inspection data is presented as an image bank in Appendix B (see p. 78) which is divided into five Sections. Section B.1 (see p. 78) introduces the reference heating process for a pipe area without defets. Section B.2 (see p. 79) describes the testing of the calibration plates. Section B.3 (see p. 81) deals with the IRT for plates. Section B.4 (see p. 84) gives the testing results for empty pipes. Section B.5 (see p. 90) describes the testing results for pipes filled with water.

9.3 Phased Array Ultrasonic Testing

The S-scan was found to be best view mode for the detection of small flat-bottom bores. Even a bore of 1 mm in diameter could be detected as weakening of the back wall echo.Gradual wall losses are best seen from the B-scan. B-, C- and S-scans were found the most informative for delaminated areas. The S-scan was the most suitable for pipes. Delamination and impact damages were detected as loss of back wall echo energy.

The effect of water to the back wall echo is significant but does not completely remove it. For normal angle of incidence, the reflection coefficient for the GRP–water -interface can be calculated using Equation (5.9) (see p. 25)

$$R = \frac{Z_2 - Z_1}{Z_2 + Z_1} = \frac{1,5 - 4,0}{1,5 + 4,0} \approx -0,45, \tag{9.1}$$

where Z_2 is the acoustic impedance of water and Z_1 is acoustic impedance of GRP. Even so, a reflection pressure of 45 % is enough for an adequate PAUT results. When comparing Figure C.8a (see p. 101) of the empty pipe to Figure C.8b (see p. 101) of the pipe filled with water, it is clear that approximately 45 % of the ultrasound reflects back to the probe.

As mentioned in Section 5.7 (see p. 38), the phased array ultrasonic testing of the GRP includes many challenges. However, Figures of Appendix C prove that with a proper delay line, the PAUT is an informative and illustrative NDT technique for the GRP.

Multiple plastics were studied and compared as the delay line material. Two plastics were found to form an adequate acoustic matching to the GRP: *Polytetrafluoroethylene* (PTFE) or *Teflon* in colloquial language and *polyurethane* (PUR). The advantage of Teflon is that its friction coefficient is small. Thus, it provides a smooth movement for the probe along the surface of the target. On the other hand, it is rigid. Therefore, a good contact between the delay line and the target may be hard to obtain. The fric-

tion coefficient of the PUR is greater than Teflon but it is flexible and not completely hard. Hence, a good contact and clear back wall echo can be obtained. The gain may be set to as high as 50 dB when using Teflon or PUR as the delay lines.

Inspection data is given as an image bank in Appendix C (see p. 97) which is divided into four Sections. Section C.1 (see p. 97) describes the testing of the calibration plates. Section C.2 (see p. 99) deals with the testing of the plates. Section C.3 (see p. 100) gives the testing results for empty pipes. Section C.4 (see p. 101) describes the testing results for pipes filled with water.

9.4 Zero Interface Probe Ultrasonic Testing

Resolution for used probe is 3 mm. Consequently, smaller diameter flat-bottom bores could not be detected. Thinning of the target in 1 mm steps could be detected. Also the barrier layer can be detected in some cases. Delamination and impact damages were detected as both loss of back wall echo energy and multiple delamination echoes between delay line echo and back wall echo.

A portion of ultrasonic energy is transferred to water in the GRP–water -interface because the acoustic impedance of water is non-zero. Therefore, the back wall echo is weaker but detectable when the pipes are filled with water.

Inspection data is presented as an image bank in Appendix D (see p. 102). Section D.1 (see p. 102) describes the testing of the calibration plates. Section D.2 (see p. 104) deals with the testing of plates. Section D.3 (see p. 105) gives the testing results for empty pipes. Finally, Section D.4 (see p. 107) describes the testing results for pipes filled with water.

9.5 Digital Radiographic Testing

In digital radiographic testing (DRT) it is easy to adjust exposure time, voltage and current to obtain the most informative DRT image. Taking one DRT image is fast because a laptop is used to control all the parameters and exposure time is only a few seconds for glass fiber reinforced plastics.The DRT is a useful NDT technique for detecting wall loss, delamination and major cracks in the pipe profile image for empty pipes. Delamination is only visible in profile figure. Fiber orientation and major cracks are visible also in shell figure. Wall loss, major cracks and fiber orientation can be detected from plates. The conditions of the barrier, support and protective layers may be monitored in some degree. Soft radiation shall be used as the x-rays transit through the GRP structures easily.

The localization of the defects should be done with visual testing or infrared ther-

mography. The importance of the localization of the defects is clear because certain defects need to be accurate in the profile to be seen in the DRT image.

The bigger the water filled GRP pipe is in diameter, the more difficult the testing becomes. The x-rays need more energy to transmit through the water filled GRP pipe. Thus, the effect of the GRP structure to the energy of the x-ray is minimal in comparison with water and wall loss in the shell cannot be detected. The diameter of 200 mm was found critical for the DRT. Figure E.11 (see p. 114) illustrates that the detection of defects in the DRT turn out to be difficult for water filled pipes with diameter exceeding 200 mm.

Impact damages could not be found in any of the test pieces even though the resolution was good. Consequently DRT cannot reveal thin cracks or small delaminations due to impact damages.

The biggest pipe in diameter N_GRP_1, contains a large volume of water. The energy needed for radiographic testing is so great that the the content of the pipe will deteriorate the image quality and sensitivity to detect defects.

Inspection data is presented as an image bank in Appendix E (see p. 108). Section E.1 (see p. 108) describes the digital radiographic testing results for reference plates. Section E.2 (see p. 109) introduces the testing results for plates. Section E.3 (see p. 110) introduces the results for pipes. Section E.4 (see p. 114) covers pipes filled with water. Testing parameters are introduced in Section E.5 (see p. 116). Section E.6 (see p. 117) is dedicated for the analysis of the intensity profiles and measurements of the defects. The type of the defect is marked inside of a rectangle with a specific color code. Red indicates delaminations, green indicates wall losses and yellow indicates cracks.

10 Conclusion

The main goal of this work was to find the best combination of nondestructive testing techniques available to locate, identify and visualize the defect types both in new and used glass fiber reinforced plastic products. The inspection must remain reliable and reproducible. The main problem was that there is not much experience about nondestructive testing (NDT) for glass fiber reinforced plastics (GRP). As a result, NDT-inspectors do not have the proper knowledge to inspect composites. Only in recent years The Processing Industry Standards Association published standards concerning visual testing (VT), infrared thermography (IRT), ultrasonic testing (UT) and digital radiographic testing (DRT) for fiber reinforced plastics (PSK 6312, 2011; PSK 6313, 2011; PSK 6314, 2011; PSK 6316, 2009). However, wide illustrative and instructive work still remained undone before this work.

This research showed that the VT and the IRT are the best techniques for localizing wall losses, delamination and strong impact damages. The IRT proved to be fast, illustrative, reliable and reproducible. Heating sources that produce constant heat flux were found to best, as also stated in my previous study (Lähteenmäki, 2011). If possible, IRT should be done as a real-time video recording to be able to study the whole heating process afterwards. Some problems may occur in stable temperature conditions or when the distance between the target and the IRT camera is large, both of them decrease the possibility to detect small defects. Other NDT techniques are to be used to quantify the type and the severity of the defects.

Zero interface probe ultrasonic testing (ZIP UT) was found to be excellent in measuring wall thickness and detect wall losses and delamination. Impact damages can be studied when they are strong enough to cause delamination. The ZIP probe and delay line engineering proved to be nearly perfect for the testing of the GRP.

Phased array ultrasonic testing (PAUT) remained challenging after my Bachelor's Thesis (Lähteenmäki, 2011) because the lack of the proper delay line. However, this study proved that with a proper delay line, the PAUT is an extremely informative and illustrative NDT technique for the GRP. The S-scan was found to be best for the detection of small flat-bottom bores. Even a flat-bottom bore 1 mm in diameter could be detected as the weakening of the back wall echo. Gradual wall losses are most easily seen from the B-scan. B-, C- and S-scans were found to be the most informative for delaminated areas. S-scan was the most suitable for pipes. Delamination and impact damages were detected as loss of back wall echo energy. Water effect to the back wall echo is significant but does not completely remove it.

The DRT was found to be a good technique for detecting wall loss, cracks and delamination, especially from the profile image. The DRT can be used to quantify the

severity of the delamination. The DRT of calibration plates showed that from the intensity profile, a skilled inspector is able to measure the thickness and the dimensions of the defects very accurately.

Testing parameters for all of the NDT techniques were quite similar with new pipes and pipes removed from service. However, many of the whiter areas in pipes removed from service were found to be wall losses rather than delamination which was the original hypothesis of the VT. This problem can be overcome most easily with the help of the ultrasonic testing.

In the future, research work should be done to confirm that if the results of this work are comparable to other reinforce plastics and composites. Also more complex GRP structure shapes (joints, glanges, field branches ...) should be studied. Microwave testing (MWT) is one of the upcoming NDT techniques that are being developed. In detail study of dielectrics and composites and their microwave testing can be found from my Special Assignment in Electrophysics -research project (Lähteenmäki, 2015). Also, a list of all possible NDT techniques for the dielectrics and composite inspection is provided.

References

M. Anderson, editor. *Phased Array Testing: Basic Theory for Industrial Applications*. NDT Field Guide. Olympus NDT, 1 edition, 2010.

L. Bryant and P. McIntire, editors. *Nondestructive Testing Handbook*, volume 3 of *Radiography & Radiation Testing*. The American Society for Nondestructive Testing, 2 edition, 1985. ISBN 0-931403-6.

J. A. de Raad, editor. *Industrial Radiography Image forming techniques*. GE Inspection Technologies, 2008.

N. Dubé, editor. *Introduction to Phased Array Ultrasonic Technology Applications: R/D Tech Guideline*. Advanced Practical NDT Series. R/D Tech inc., 1 edition, 2004. ISBN 0-9735933-0-X.

FLIR T425 Technical Data. Infrared camera with picture-in-picture and thermal fusion. Published by FLIR, 2011. [WWW]. [2.8.2015]. http://support.flir.com/DsDownload/Assets/45307-0202_en_51.pdf.

Ultrasonic Probes. GE Inspection Technologies, 2006. [WWW]. [20.6.2015]. http://www.ndtproducts.ca/products/files/UT%20Probe%20Cat.pdf.

Ultrasonic Transducers For Flaw Detection and Sizing. GE Inspection Technologies, 2008. [WWW]. [15.6.2015]. http://www.ge-mcs.com/download/ultrasound/transducers/GEIT-20117EN_ultrasonic-transducer-catalog.pdf.

E. Ginzel and D. Stewart. Photo-Elastic Visualisation of Phased Array Ultrasonic Pulses in Solids. In *16th World Conference on Nondestructive Testing*. Materials Research Institute, Waterloo, Ontario, Canada and Oceaneering Inspection, Aberdeen, Scotland, United Kingdom, 2004. ISBN 0-9736577-0-7.

B. Harris, editor. *Developments in GRP Technology–1*. Applied Science Publishers LTD, 1983. ISBN 0-85334-204-0.

Infrared Spectral Selection. Atmospheric Attenuation in Infrared Region, 2015. [WWW]. [23.6.2015] http://www.photonics.com/EDU/Handbook.aspx?AID=25132.

M. Kakkonen. NDT menetelmien soveltuvuus kuitulujitettujen muovituotteiden kunnonvalvontaan prosessiolosuhteissa. Master's thesis, Tampere University of Technology, 2011.

H. Lähteenmäki. Infrapunatermografia vaiheistetun ultraäänitarkastuksen apuna lasikuitulujitetun muovin NDT-tarkastuksessa. Bachelor's Thesis, Aalto University, School of Electrical Engineering, 2011.

H. Lähteenmäki. Detection of Defects in Dielectrics by Microwave Testing. Special Assignment in Electrophysics, Aalto University, School of Electrical Engineering, 2015.

X. Maldague and P. Moore, editors. *Nondestructive Testing Handbook*, volume 3 of *Infrared and Thermal Testing CD-ROM*. The American Society for Nondestructive Testing, 3 edition, 2001. ISBN 978-1-57117-081-1.

P. Moore. *Nondestructive Testing Handbook, Third Edition: Volume 9, Visual Testing*. ASNT, 2010. ISBN 978-1-57117-186-3.

NDT Resource Education. Modes of sound waves, 2015. [WWW]. [7.8.2015] http://www.ndt-ed.org/EducationResources/CommunityCollege/Ultrasonics/Physics/modepropagation.htm.

Panametrics. *Ultrasonic Transducers, Wedges, Cabels, Test Blocks*. Olympus, 2012.

Phased Array Probes and Wedges. Olympus NDT, 2010. [WWW]. [22.8.2015]. http://www.olympus-ims.com/en/.downloads/download/?file=285213040&fl=en_US.

Phased Array Tutorial. Olympus phased array tutorial, 2015. [WWW]. [15.6.2015] http://www.olympus-ims.com/en/ndt-tutorials/phased-array/.

PSK 6312. Industrial Fibre-reinforced Plastic Products. Condition monitoring. Sensory Inspection. PSK Standards Association, 2011. 3 p.

PSK 6313. Industrial Fibre-reinforced Plastic Products. Condition monitoring. Radiographic Inspection. PSK Standards Association, 2011. 10 p.

PSK 6314. Industrial Fibre-reinforced Plastic Products. Condition monitoring. Ultrasonic Inspection. PSK Standards Association, 2011. 5 p.

PSK 6316. Industrial Fibre-reinforced Plastic Products. Condition monitoring. Thermographic Camera Inspection. PSK Standards Association, 2009. 16 p.

O. Saarela, I. Airasmaa, J. Kokko, M. Skrifvars, and V. Komppa. *Komposiittirakenteet*. Muoviyhdistys ry, Helsinki, 2007. ISBN 978-951-9271-28-6.

SFS 3910. Reinforced themosetting plastics. Visual inspection and classification of corrosion resistant laminates and joints. Finnish Standards Association SFS, 1993. 7 p.

SFS 5162. Plastics pipes. GRP pipes and fittings. raw material and structure. Finnish Standards Association SFS, 1993. 4 p.

The Norwegian Oil Industry Association (OLF). *Recommended Guidelines for NDT of GRP Pipe Systems and Tanks*, 1997.

Ultrasonic Transducers. Imasonic, 2010.

N. J. Walker. *Principles and Practice*, volume 1 of *BINDT CM Series: Infrared Thermography*. The British Institution of Non-Destructive Testing, 2004. ISBN 0903132 33 8.

H. Young and R. Freeman. *Sears and Zemansky's University Physics with Modern Physics*. Pearson Addison-Wesley, 11 edition, 2008. ISBN 978-0805386844.

A Visual Testing Image Bank

Defects are marked inside a coloured rectangle. Green signifies wall loss, yellow major cracks, blue impact damages, black delamination and red air bubbles.

A.1 Calibration Plates

Visual testing shall be done for both sides of the target if possible. The resolution for visual testing is smaller than 1 mm in diameter according to Subfigure A.1b if inspected from the defected side. Otherwise, the resolution is considered 2 mm in diameter (see Subfigure A.1a).

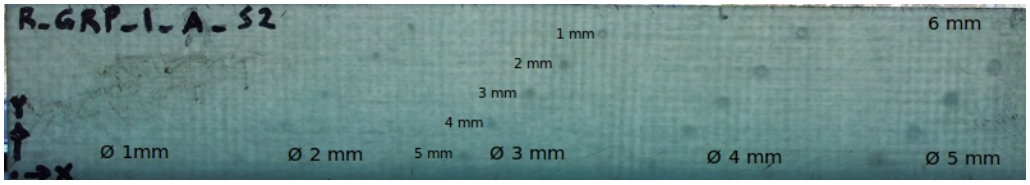

(a) R_GRP_1_A_S2. A-side. Nominal wall thickness (6 mm) seen in the upper-right corner. ⌀ indicates the diameter of the flat-bottom diagonal bores. Diagonal values indicate the wall thicknesses above the diagonal bores. All the other bores are detectable except for the 1 mm flat-bottom bores.

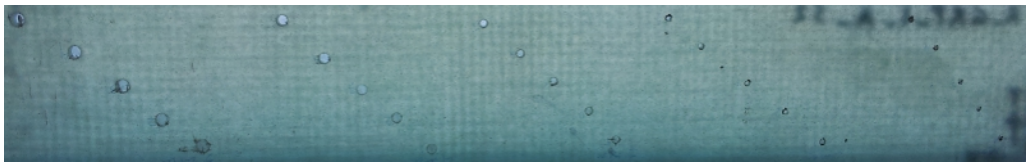

(b) R_GRP_1_B_S2 B-side. Even 1 mm flat-bottom bores are undetectable.

Figure A.1: VT of calibration plates.

A.2 Plates

All the defect mentioned above can be detected visually (see Figure A.2 on p. 71). Air bubbles are the hardest to detect. As mentioned in Section A.1, the reliability of the inspection is improved when the inspection can be done from the defected side of the target. Optimally the VT shall be done for both sides of the target.

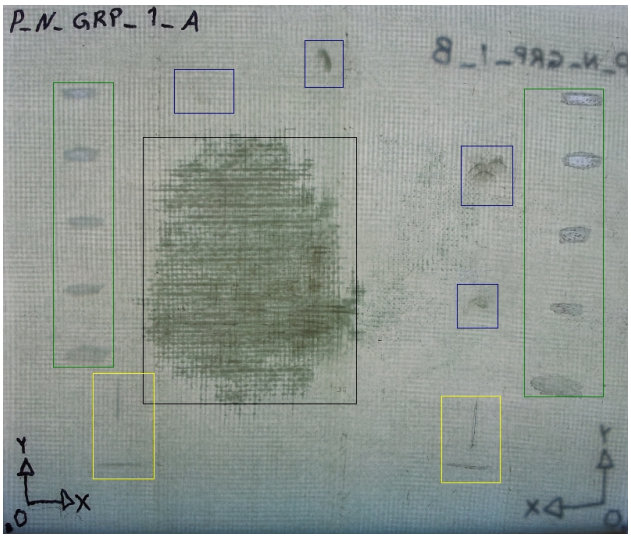

(a) P_N_GRP_1_A. A-side. Wall losses, major cracks, impact damages and delamination

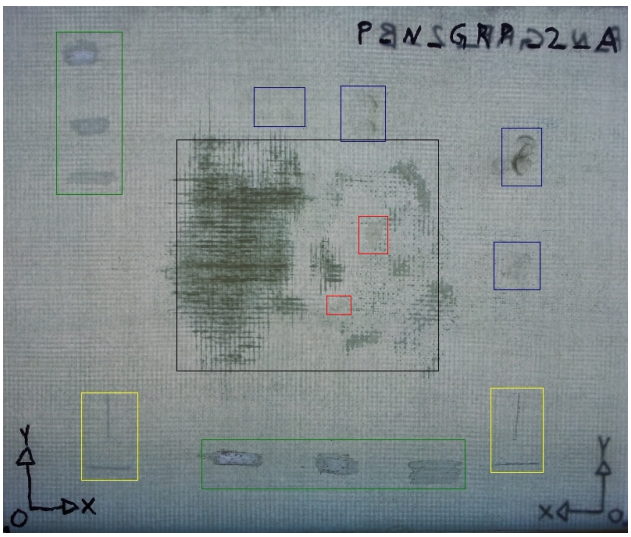

(b) P_N_GRP_2_A. A-side. Wall losses, major cracks, impact damages, delamination and air bubbles.

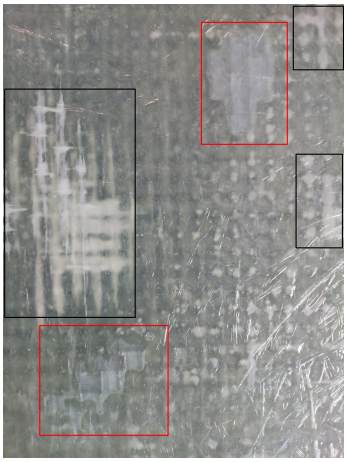

(c) P_N_GRP_2_B. B-side. Zoomed air bubbles and delamination.

Figure A.2: VT of plates.

A.3 Pipes

VT of N_GRP_1 outer surface is shown in Figure A.3. Impact damage cannot be distinguished from the delamination. However, it causes cracks onto the inner surface of the pipe that cannot be detected from the outside.

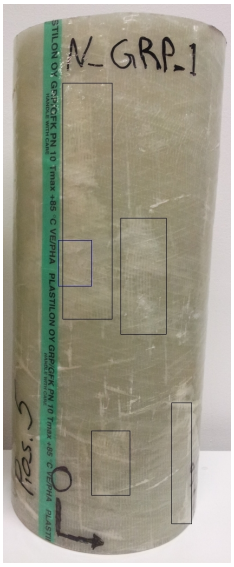

(a) Impact damage on the top of delamination.

(b) Delaminations and impact damage.

(c) Strong impact damage causes circular delamination.

(d) Weak impact damage might cause cracks without prodicing delamination.

(e) Wall losses are not easy to detect.

Figure A.3: VT of N_GRP_1. Outer surface.

VT of N_GRP_1 inner surface is shown in Figure A.4. Whiter area under the cracks is delamination. Cracks are totally undetectable from the outside surface.

(a) Matrix cracks due to impact damage.

(b) Matrix cracks of matrix due to impact damage.

(c) Matrix cracks due to impact damage.

(d) Wall losses are usually very hard to detect from the outer surface.

(e) Cracks are usually very hard to detect from the outer surface.

Figure A.4: VT of N_GRP_1. Inner surface.

VT of N_GRP_2 outer surface is shown in Figure A.5.

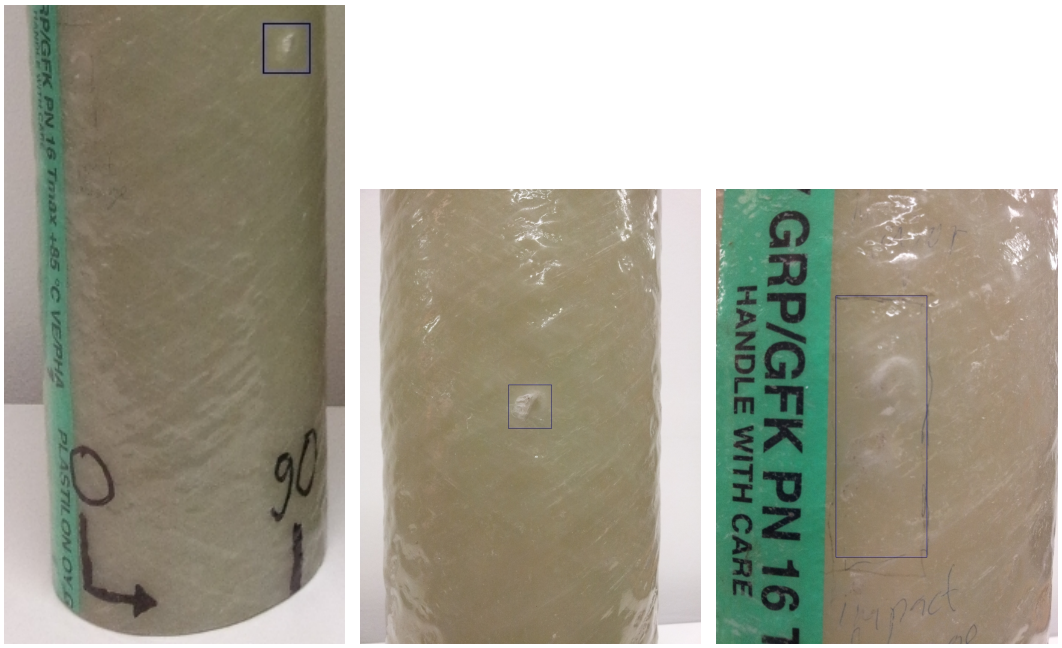

(a) Strong impact damage. Otherwise defectless.

(b) Strong, point-like impact damage.

(c) Strong impact damage.

(d) Weak impact damage.

(e) Major crack near the surface.

(f) Gradual wall loss.

Figure A.5: VT of N_GRP_2. Outer surface.

VT of N_GRP_2 inner surface is shown in Figure A.6.

(a) Cracks and darker delaminated area caused by strong impact damage.

(b) Cracks caused by very weak impact damage that is not seen from outside.

(c) Gradual wall loss not seen from outside.

Figure A.6: VT of N_GRP_2. Inner surface.

VT of U_GRP_2 outer surface is shown in Figure A.7 (see p. 75). Whiter areas are usually wall losses rather than delaminations. To be able to separate delamination and wall loss IRT, PAUT or ZIP-UT can be used, IRT being the best method.

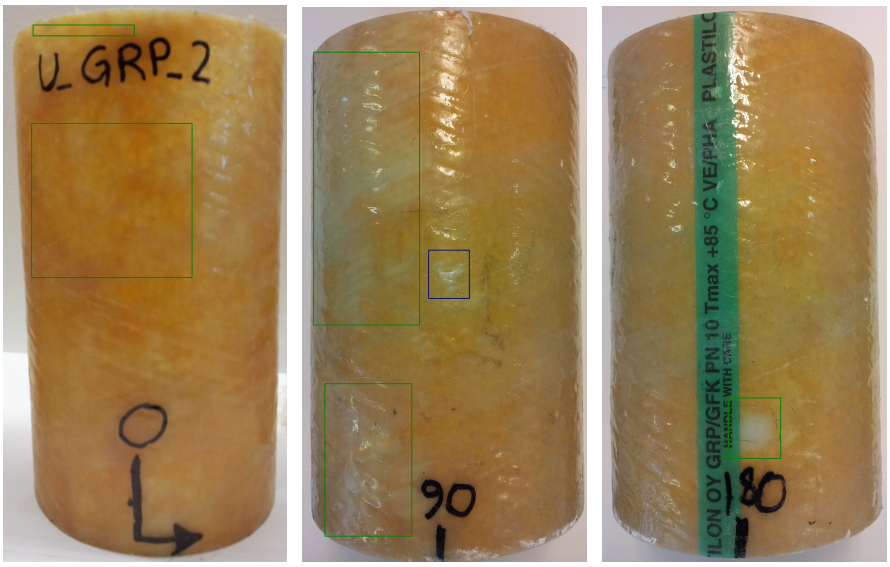

(a) Wall loss.

(b) Wall loss and impact damage.

(c) Local wall loss.

Figure A.7: VT of U_GRP_2. Outer surface.

VT of U_GRP_3 outer surface is shown in Figure A.8. Whiter areas are usually wall loss rather than delamination.

Figure A.8: VT of U_GRP_3. Outer surface. Wall losses.

VT of U_GRP_4 outer surface is shown in Figure A.9.

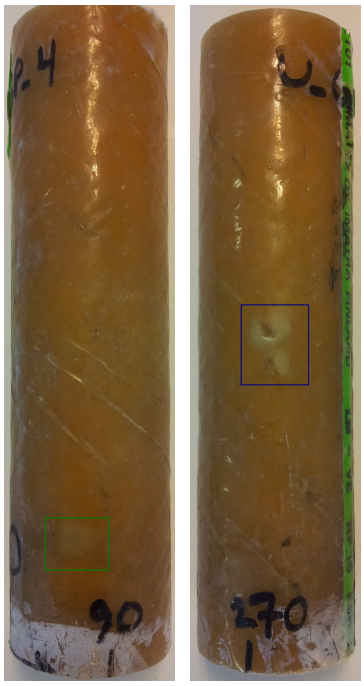

(a) Wall loss. (b) Impact damage.

Figure A.9: VT of U_GRP_4. Outer surface.

VT of U_GRP_5 is shown in Figure A.10.

(a) Wall loss not visible. (b) Wall loss in the inside surface.

Figure A.10: VT of U_GRP_5.

GRP removed from service may be difficult to visually test from inside surface because of loose fiber in the inner surface (see Figure A.11).

Figure A.11: VT of U_GRPs. Loose fiber in the inner surface.

B Infrared Thermography Image Bank

The heating source for calibration plates (see Section B.2 on p. 79), plates (see Section B.3 on p. 81) and empty pipes (see Section B.4 on p. 84) was a 1000 W infrared heater. The water inside pipes was heated with a 1600 W resistive heater.

The distance of the target varied between 0.3 m and 1.2 m.

B.1 Reference Heating Process

Reference heating process for the pipe area without defects is shown in Figure B.1 as heating time and and therefore temperature increases.

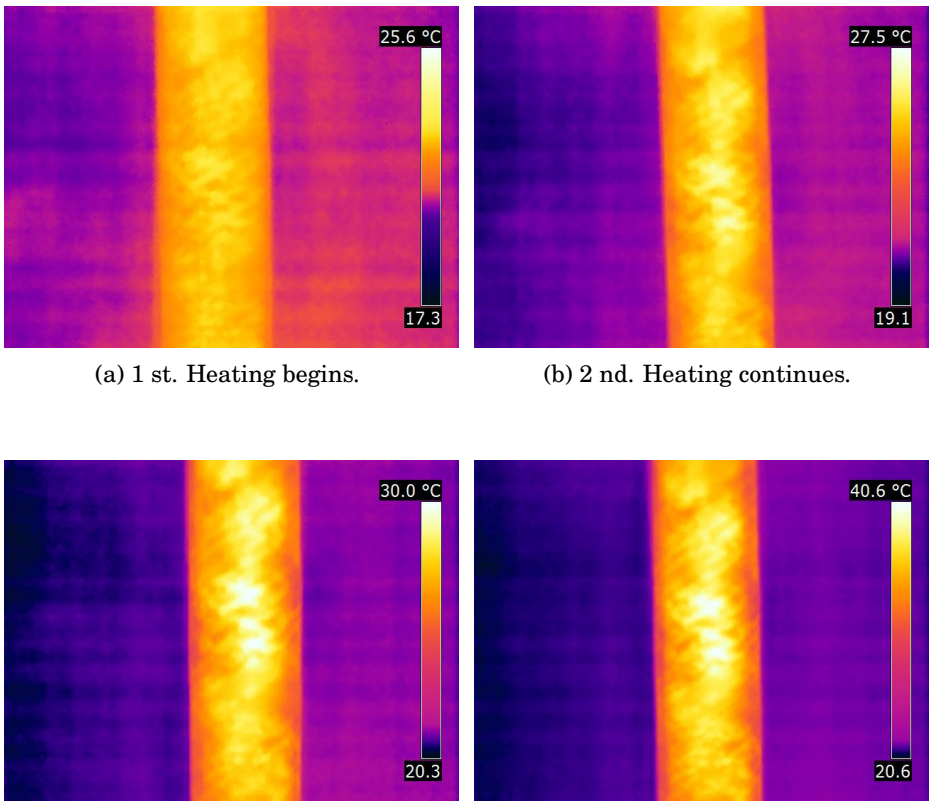

(a) 1 st. Heating begins.

(b) 2 nd. Heating continues.

(c) 3 rd. Heating still continues.

(d) 4 th. Heating ends.

Figure B.1: Reference heating process for defectless pipe area.

B.2 Calibration Plates

Testing shall be done for both surfaces. If inspected from the side of the defects and heated from the other, the resolution is much better than otherwise.

IRT of R_GRP_1_A_S4 is shown in Figure B.2.

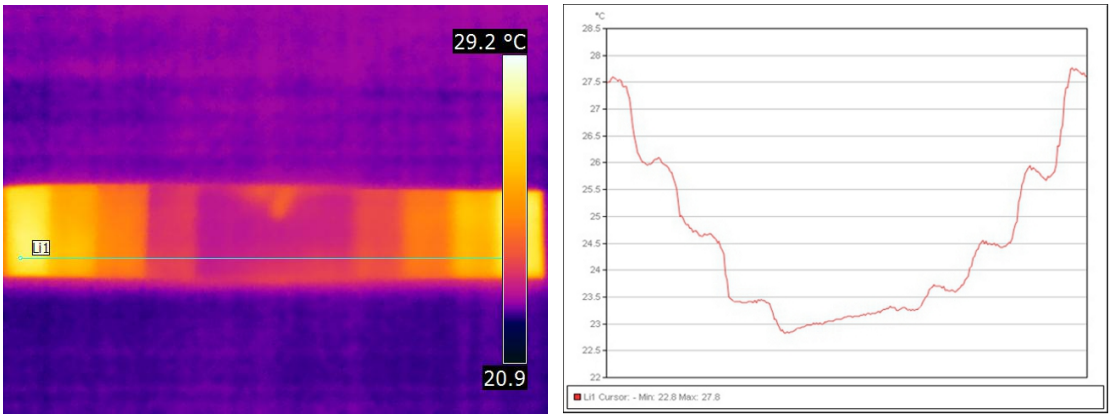

(a) IR image. (b) Infrared profile of Li1.

Figure B.2: IRT of R_GRP_1_A_S4 step plate.

IRT of R_GRP_1_A_S1 is shown in Figure B.3

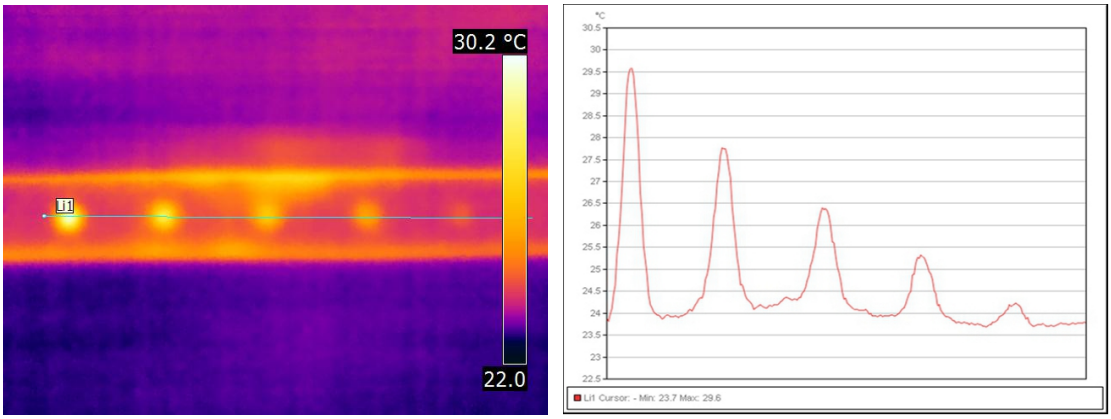

(a) IR image. (b) Infrared profile of Li1.

Figure B.3: IRT of R_GRP_1_A_S1.

IRT of R_GRP_1_A_S2 is shown in Figure B.4 (see p. 80). From the A-side the resolution was found to be 4 mm and the resolution for depth change is 1 mm.

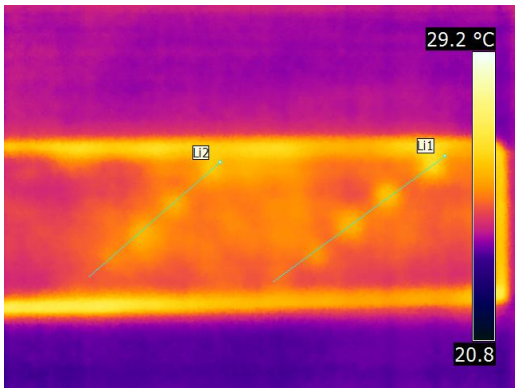

(a) Flat-bottom bores of 4 mm and 5 mm in diameter .

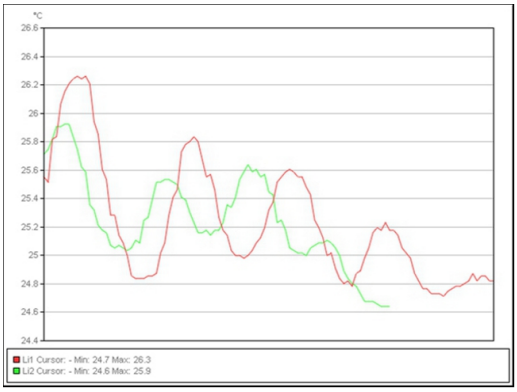

(b) Infrared profile of Li1 and Li2.

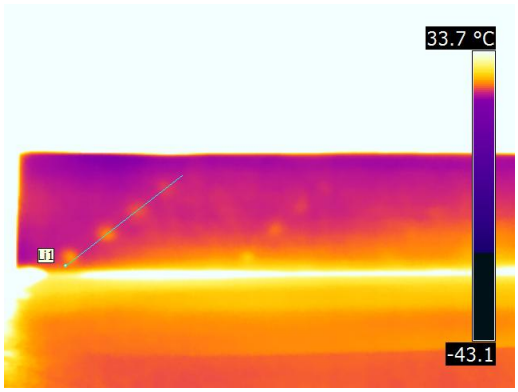

(c) Flat-bottom bores of 5 mm and 4 mm in diameter.

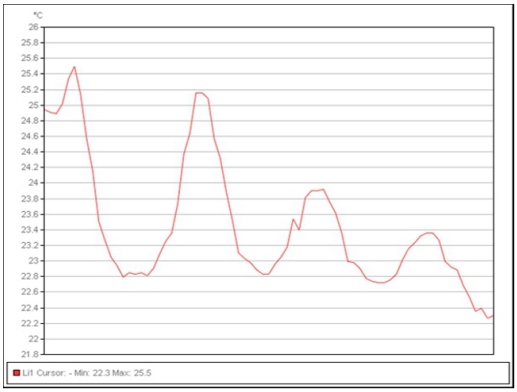

(d) Infrared profile of Li1.

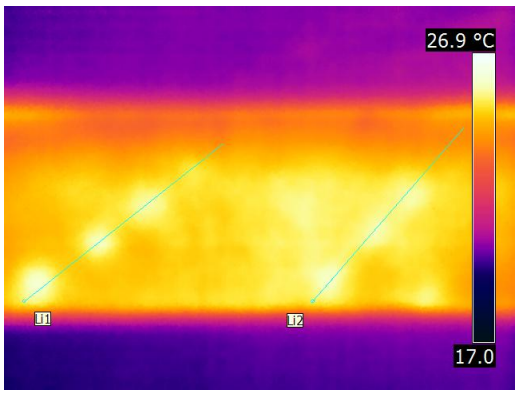

(e) IR image from the small distance of 0,3 m.

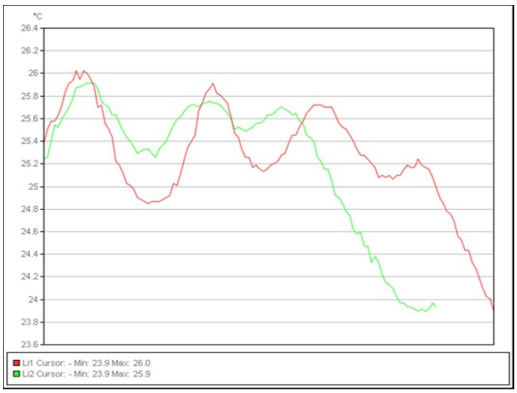

(f) Infrared profile of Li1 and L2.

Figure B.4: IRT of R_GRP_1_A_S2.

IRT of R_GRP_1_B_S2 is shown in Figure B.5. From the B-side the resolution was found to be 1 mm and the resolution for depth change is 1 mm. Therefore, heating shall be done from the other side of the defects and the IRT from the defected side when ever possible.

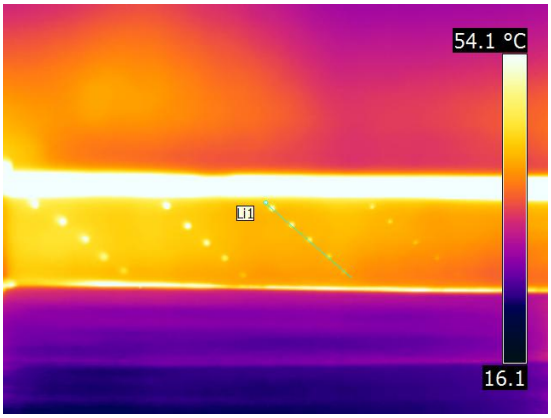

(a) Flat-bottom bores of 5 mm, 4 mm, 3 mm, 2 mm and 1mm in diameter .

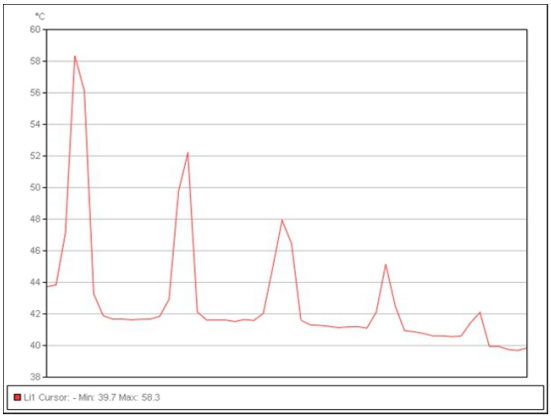

(b) Infrared profile of Li1.

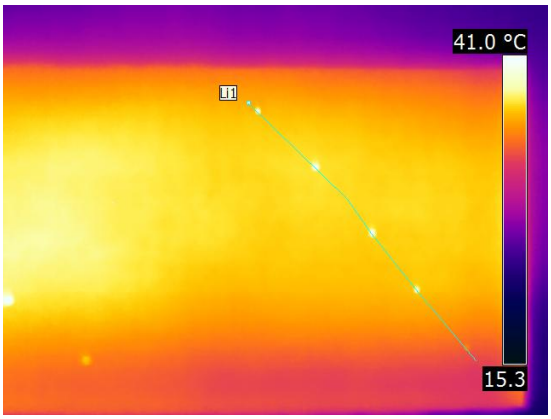

(c) IRT image from the smaller distance of 0,3 m. Resolution is as small as 1 mm.

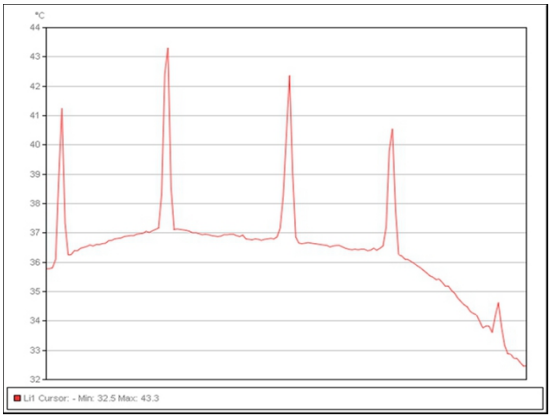

(d) Infrared profile of Li1.

Figure B.5: IRT of R_GRP_1_B_S2.

B.3 Plates

IRT of P_N_GRP_2_A is shown in Figure B.6. Air bubbles are clearly visible. Temperature difference between defectless point (Sp3 in Subfigure B.6a) and air bubbles (Sp1 and Sp2 in Subfigure B.6a) is approximately 4 °C.

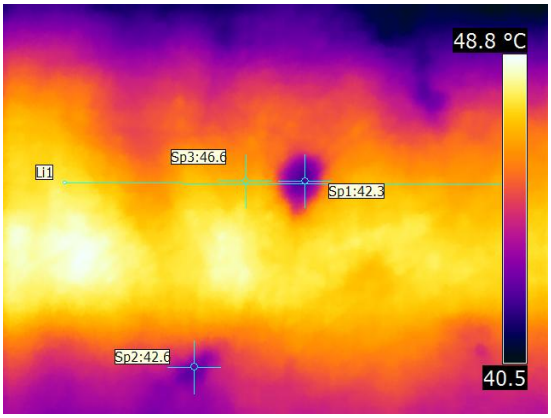

(a) Air bubbles Sp1 and Sp2. Temperature of a defectless structure is shown in Sp3.

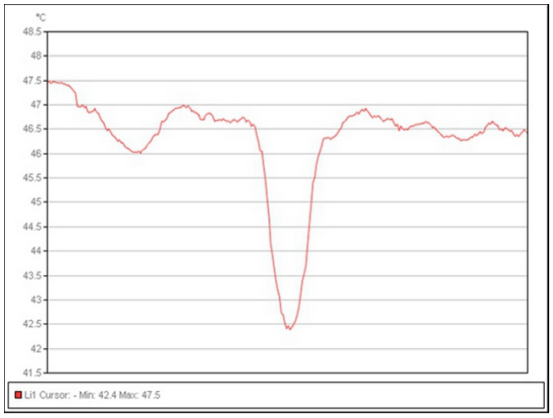

(b) Infrared profile of Li1.

Figure B.6: IRT of P_N_GRP_2_A.

IRT of P_N_GRP_1 is shown in Figure B.7. Inspection is more accurate from the defected B-side.

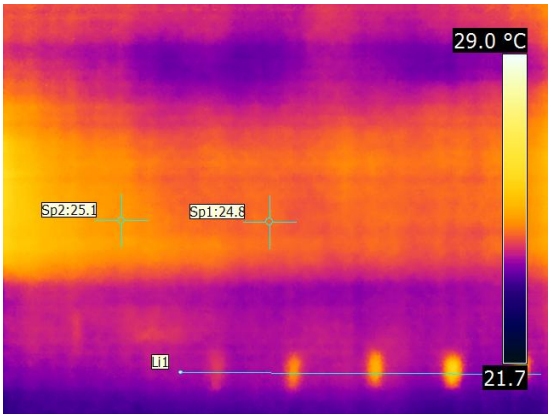

(a) B-side. Wall losses, major cracks and delamination. Sp1 is the temperature in delaminated area and Sp2 is the temperature in defectless area

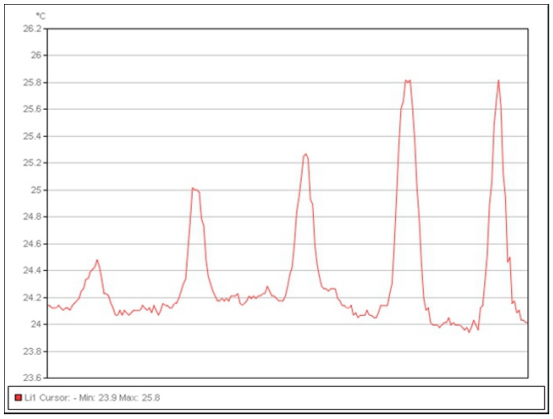

(b) Infrared profile of Li1.

Figure B.7: IRT of P_N_GRP_1 (*continued on the next page*).

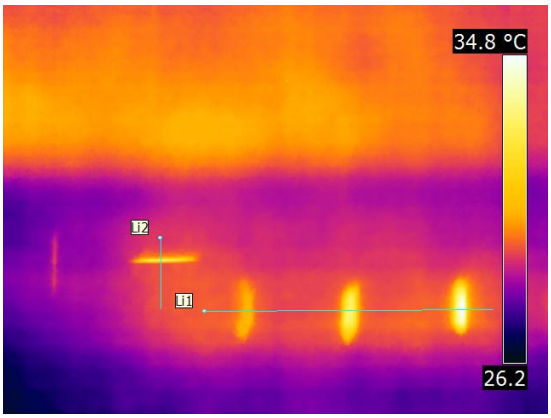

(c) B-side. Wall losses and major cracks.

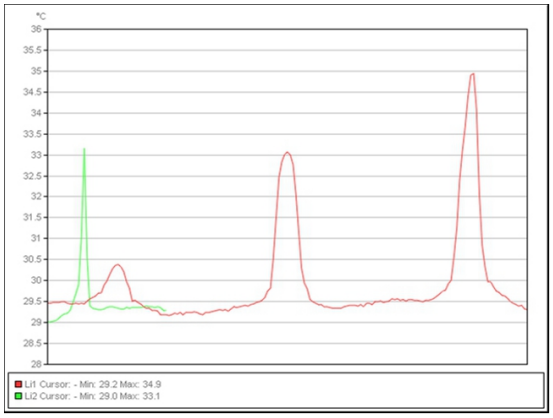

(d) Infrared profile of Li1 and Li2.

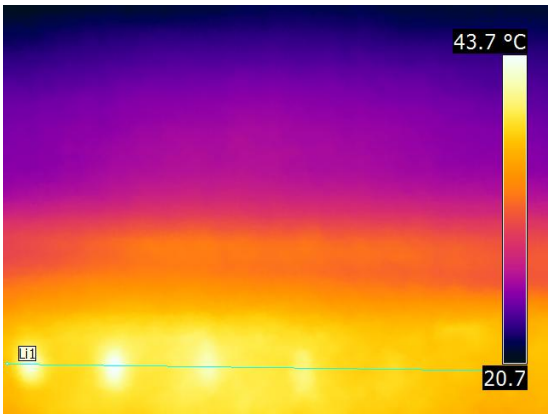

(e) A-side. Wall losses. Resolution is not nearly as good as when inspected from B-side.

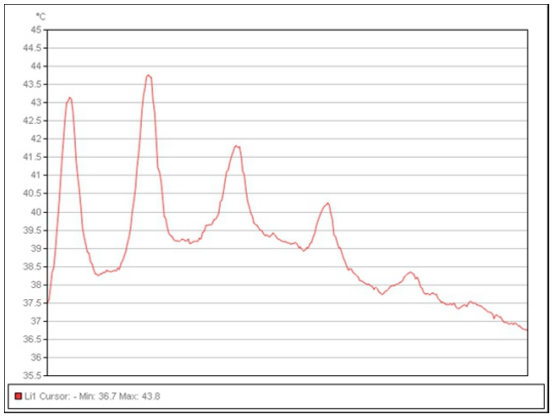

(f) Infrared profile of Li1.

Figure B.7: IRT of P_N_GRP_1.

B.4 Empty Pipes

IRT of N_GRP_1 is shown in Figure B.8. Temperatures in delaminated areas are shown in measurement points Sp1-Sp5. Sp6 is the temperature of the defectless area. Temperature difference between delaminated areas and defectless area is approximately 3 °C.

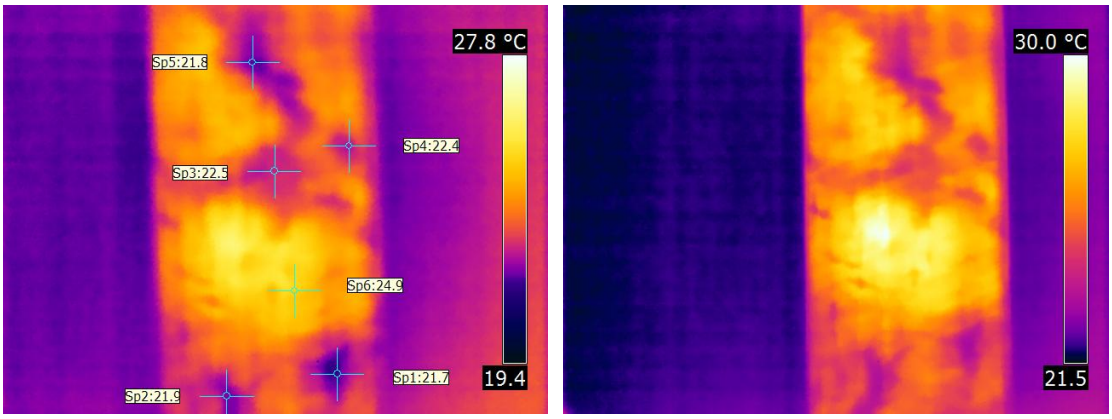

(a) Delaminations are detected as colder areas Sp1-Sp5. Sp6 is the temperature of the defectless area.

(b) Delaminations are detected as colder areas.

Figure B.8: IRT of N_GRP_1.

IRT of N_GRP_1 is shown in Figure B.9 (see p. 85). Temperatures in some of the delaminated areas are shown in measurement points Sp1-Sp3. Sp4 is the temperature of the defectless area. The temperature difference between the delaminated areas and the defectless area is 4.4. . . 6 °C.

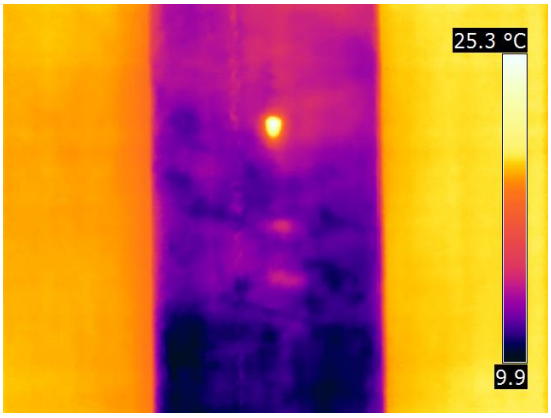

(a) Heating begins. Wall losses are immediately seen as warmed areas in the middle of the pipe. Delamination are detected as cold, dark-blue areas.

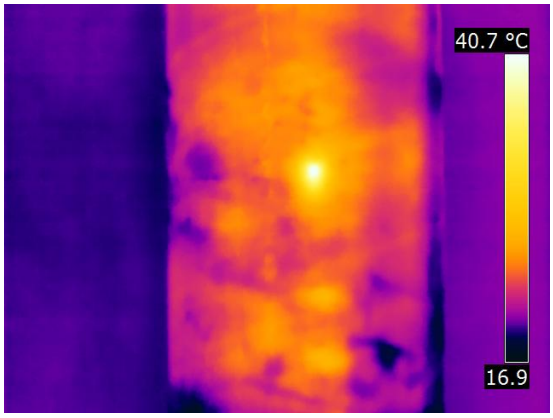

(b) Heating stopped. Defect detection resolution becomes poorer as heating process stabilizes.

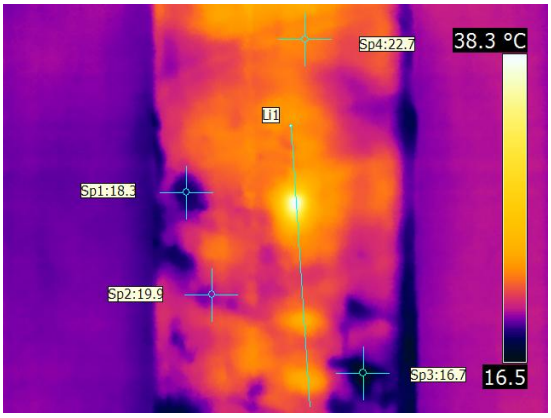

(c) Delaminations are detected as colder areas Sp1-Sp3. Sp4 is the temperature of the defectless area. Li1 is the infrared profile measurement over wall losses.

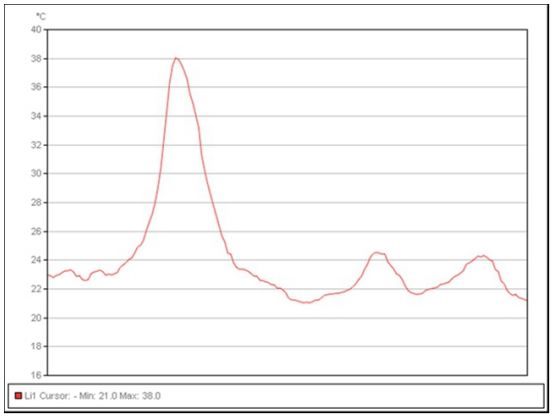

(d) Infrared profile of Li1 over wall losses.

Figure B.9: IRT of N_GRP_1.

IRT of N_GRP_1 is shown in Figure B.10. The force of the impact damage must be strong enough to create delamination. Therefore, only strong impact damages are detected as circular delaminated areas. The point of the impact damage is shown as measurement point Sp1. Sp2 is the temperature of the defectless area. The temperature difference between Sp2 and Sp1 is 1.2. . . 1.5 °C according to Subfigures B.10a and B.10b.

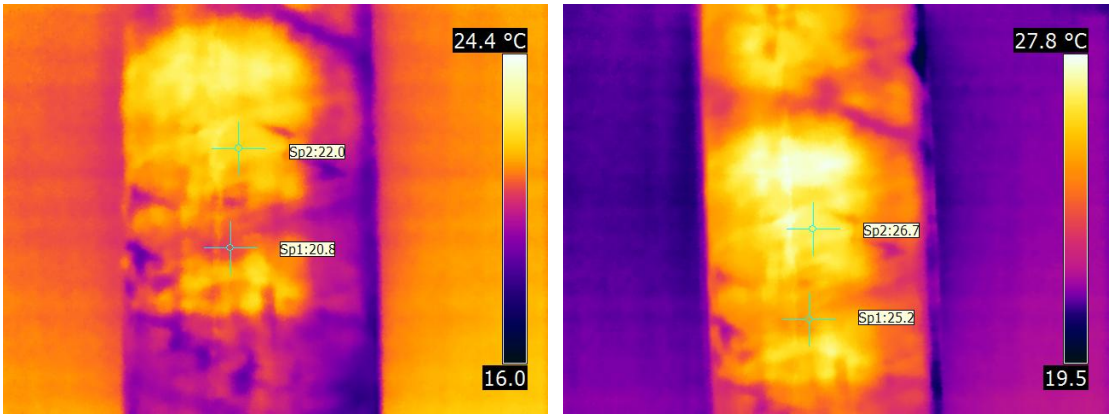

(a) Delamination caused by an impact damage is detected under Sp1 as circular area. Sp2 is the reference temperature of the defectless area.

(b) Circular delamination caused by an impact damage.

Figure B.10: IRT of N_GRP_1. Impact damage.

IRT of N_GRP_2 is shown in Figure B.11. Infrared profile measurement line Li1 of Subfigure B.11b (see p. 87) illustrates the temperature dependance of the delamination caused by an impact damage.

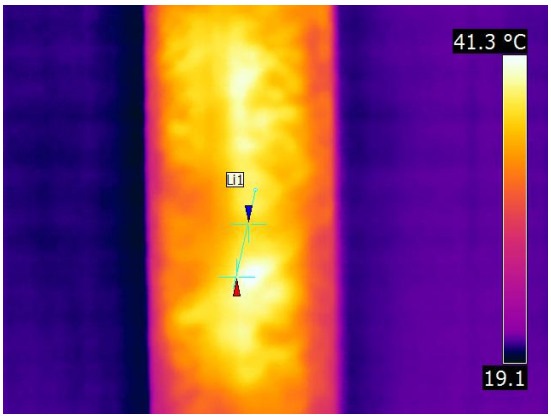

(a) Delamination caused by an impact damage is detected under blue triangle as colder circular area. Red triangle is the warmest point of the infrared profile Li1.

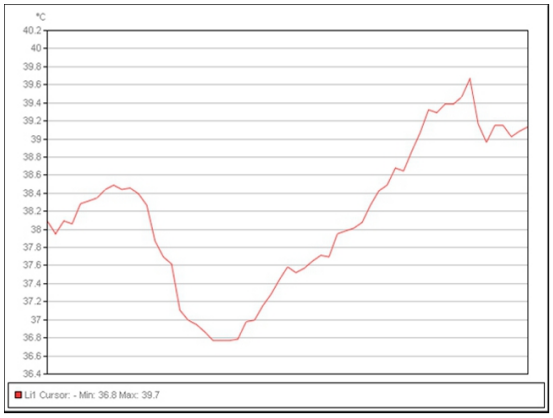

(b) Infrared profile Li1. Delamination caused by an impact damage is seen as the concave, colder part of the curve and the warmest point is seen as the absolute maximum point of the curve.

Figure B.11: IRT of N_GRP_2. Delamination caused by a strong impact damage.

Heating process and infrared profile measurement of N_GRP_2 is shown in Figure B.12.

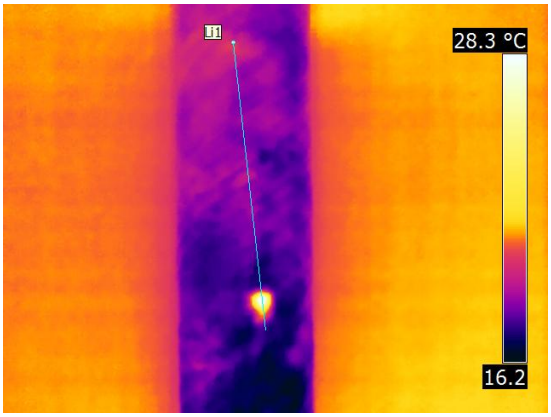

(a) Heating begins. Li1 is used to illustrate normal heating process of the defectless area except the wall loss at the end of the line.

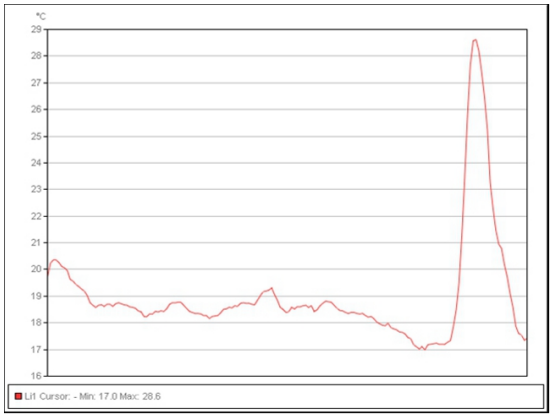

(b) Infrared profile Li1.

Figure B.12: IRT of N_GRP_2. Heating process and infrared profile measurements (*continued on the next page*).

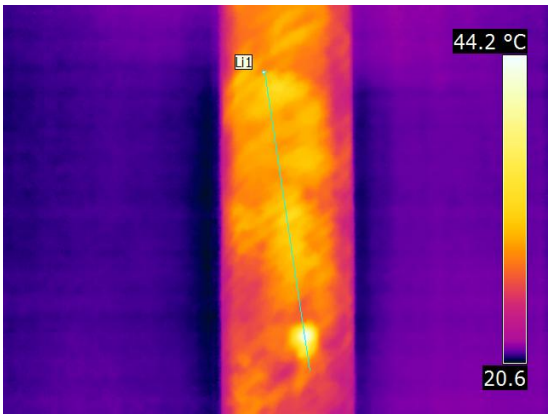

(c) Heating continues.

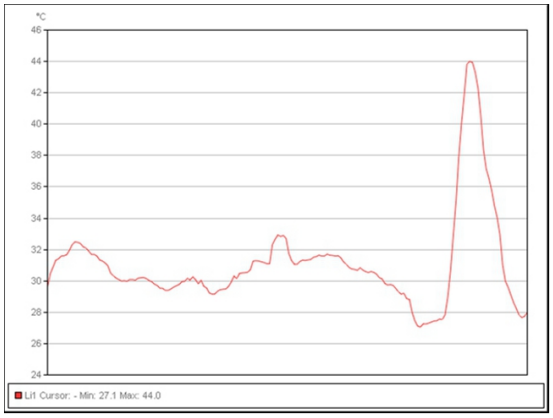

(d) Infrared profile Li1.

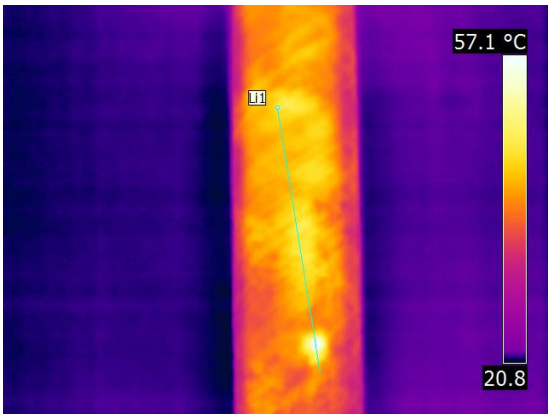

(e) Heating process is stopped.

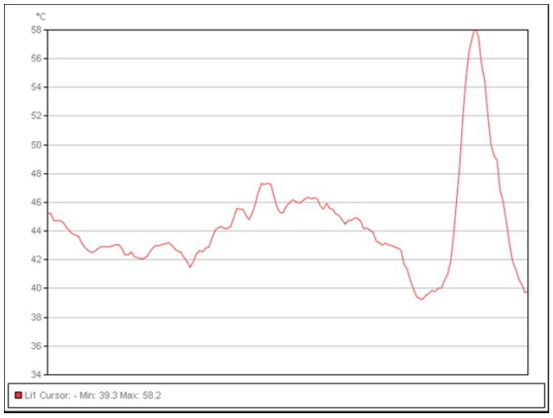

(f) Infrared profile Li1.

Figure B.12: IRT of N_GRP_2. Heating process and infrared profile measurements.

IRT of U_GRP_2 is shown in Figure B.13 (see p. 89). Pipes removed from service seem to have significant variations in wall thickness. Measuring points Sp3-Sp5 are either thicker areas of wall or delamination. This can be confirmed by ultrasonic testing. Sp2 is the point of wall loss. Sp1 is considered to be the point of defectless area. It is obvious that reference measurements should be done for new GRP products to be able to give accurate inspection results by comparison of previous inspection results.

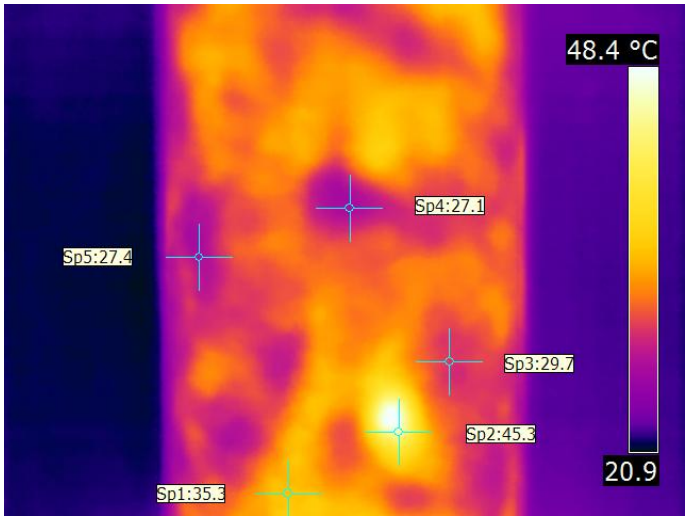

Figure B.13: IRT of U_GRP_2. Difficulty of the interpretation of the IR image without reference measurements.

IRT of U_GRP_2 is shown in Figure B.14. Infrared profiles Li1 and Li2 are used to analyse the change in temperatures. Again, it is noticed that inspection resolution drops when the temperature begins to stabilize.

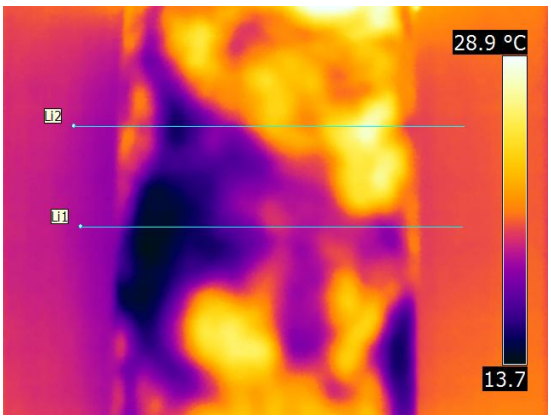

(a) Wall thickness variations and infrared profile measurement lines Li1 and Li2

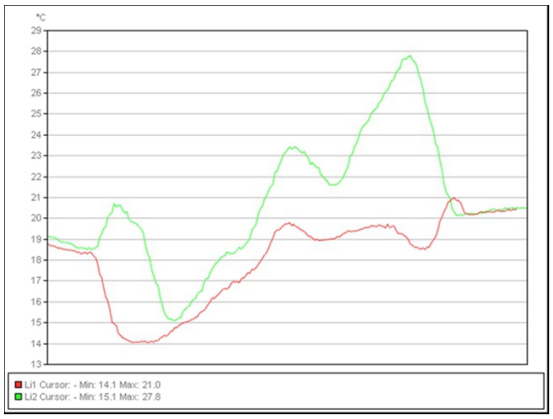

(b) Infrared profile of Li1 and Li2.

Figure B.14: IRT of U_GRP_2. Significant variations in wall thickness (*continued on the next page*).

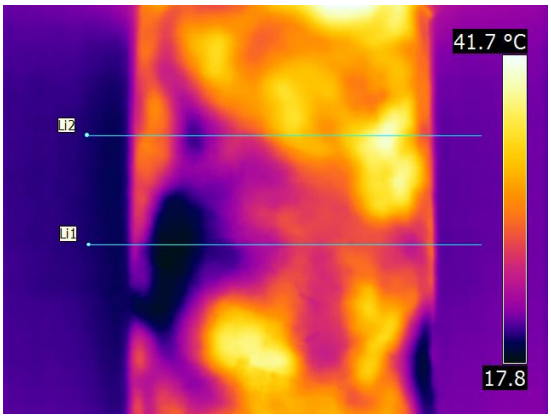

(c) Higher temperature. Wall thickness variations and infrared profile measurement lines Li1 and Li2

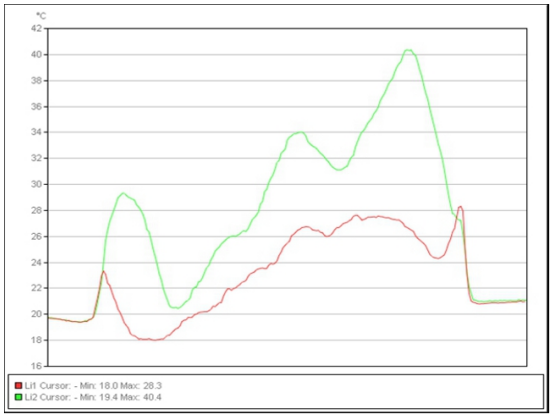

(d) Infrared profile of Li1 and Li2.

Figure B.14: IRT of U_GRP_2. Significant variations in wall thickness.

B.5 Pipes Filled with Water

IRT of N_GRP_1 is shown in Figure B.16. Wall losses greater than 1 mm in depth are easily detected. Minor wall losses between 1 mm in depth to scratches are not detected.

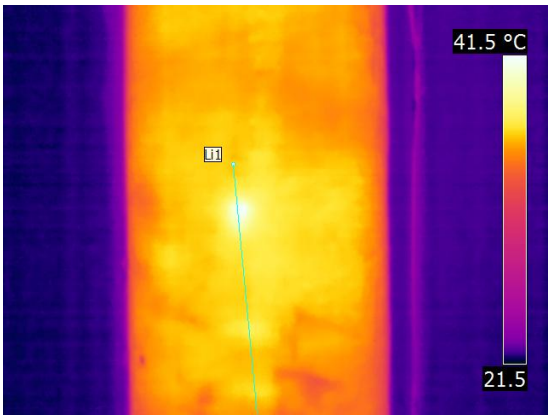

(a) Three visible wall losses along infrared profile measurement line Li1

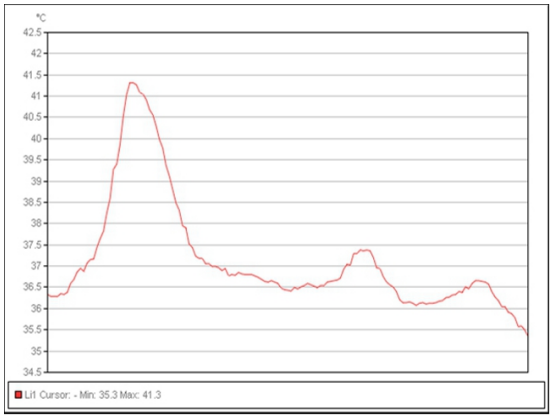

(b) Infrared profile of Li1. Local maximums indicate the temperatures in the points of wall losses.

Figure B.15: IRT of N_GRP_1. Wall losses (*continued on the next page*).

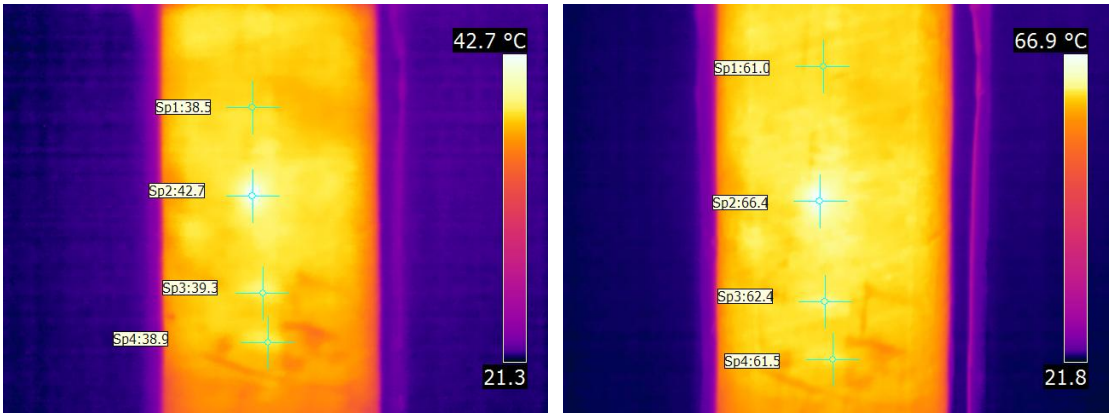

(a) Wall losses. Sp1 is the temperature of the defectless area. Sp2-Sp4 indicates the exact temperatures of the wall losses.

(b) Highest temperature. Wall losses. Sp1 is the temperature of the defectless area. Sp2-Sp4 indicates the exact temperatures of the wall losses.

Figure B.16: IRT of N_GRP_1. Wall losses.

IRT of N_GRP_1 is shown in Figure B.17 . Delamination caused by a strong impact damage is detected as circular colder area. Other delaminated areas are also detected as colder areas.

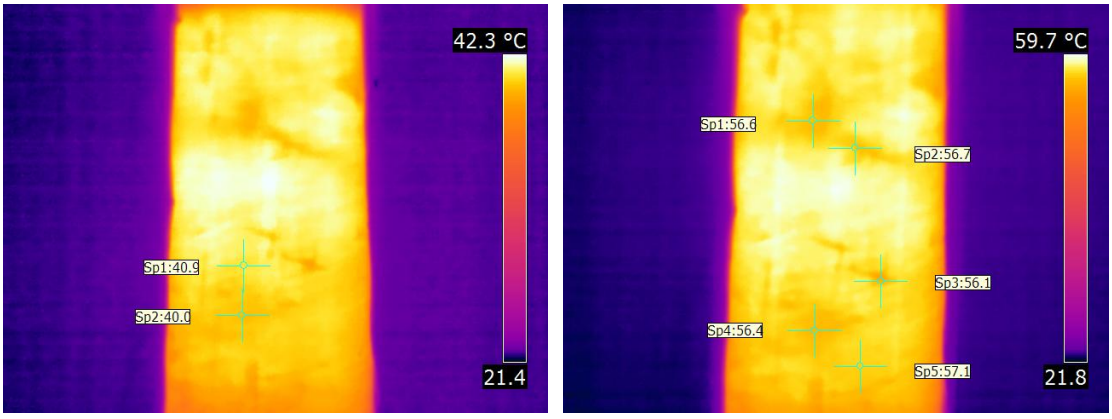

(a) Measuring point Sp1 indicates the temperature of the defectless area. Sp2 indicates the circular delamination area caused by a strong impact damage.

(b) Sp1-Sp3 indicates delaminated areas, Sp4 is the circular delamination area caused by a strong impact damage and Sp5 is the reference temperature of the defectless area.

Figure B.17: IRT of N_GRP_1. Strong impact damage.

IRT of N_GRP_2 is shown in Figure B.18. Delamination caused by a strong impact damage is detected as a circular colder area in Subfigure B.18a. Air bubbles and wall loss are detected in Subfigures B.18c. A stabilizing temperature drops the inspection resolution significantly (see Subfigures B.18e and B.18f).

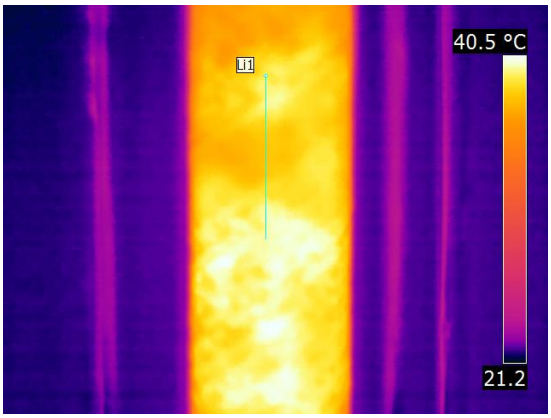

(a) Delamination caused by a strong impact damage is detected as circular colder area in the middle of the infrared profile measurement line Li1.

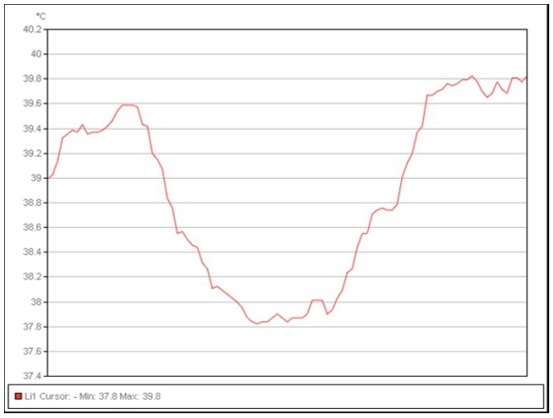

(b) Infrared profile of Li1.

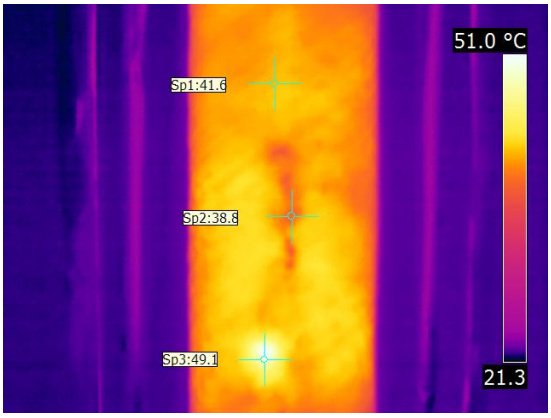

(c) Measuring point Sp1 indicates the temperature of the defectless area. Sp2 indicates air bubbles. Sp3 indicates wall loss.

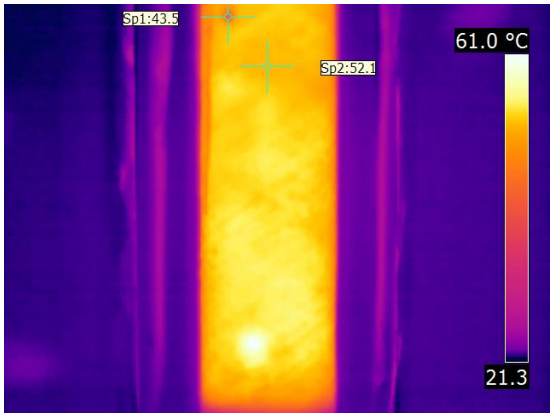

(d) Measuring point Sp2 indicates the temperature of the defectless area. Sp1 indicates an air bubble.

Figure B.18: IRT of N_GRP_2. All detected defects (*continued on the next page*).

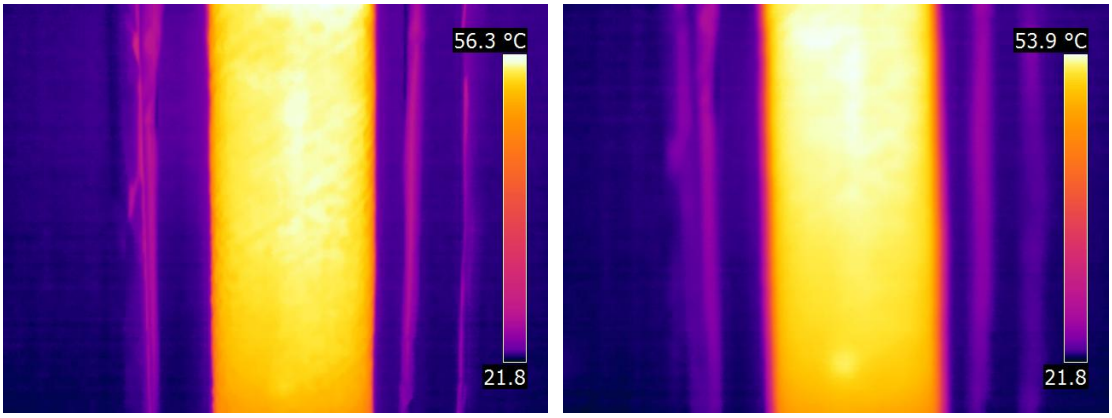

(e) Stabilized heating decreases the inspection resolution.

(f) Stabilized heating decreases the inspection resolution.

Figure B.18: IRT of N_GRP_2. All detected defects.

IRT of U_GRP_2 is shown in Figure B.19. Inspection resolution decreases when the GRP begins to thermally equalise with water.

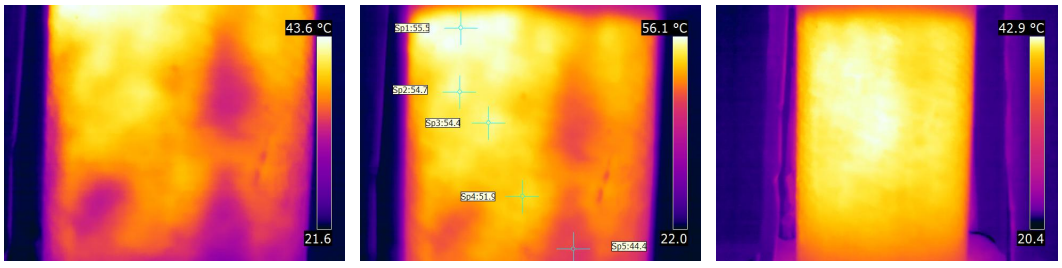

(a) Heating begins. Wall thickness variations.

(b) Sp1-Sp3 indicates the temperatures of the areas of wall losses. Sp4 is the reference temperature. Sp5 is the thickest wall thickness area.

(c) Stabilized heating process. It becomes hard to detect small defects.

Figure B.19: IRT of U_GRP_2. All detected defects.

IRT of U_GRP_3 is shown in Figure B.20. Inspection resolution decreases when the GRP begins to thermally equalise with water.

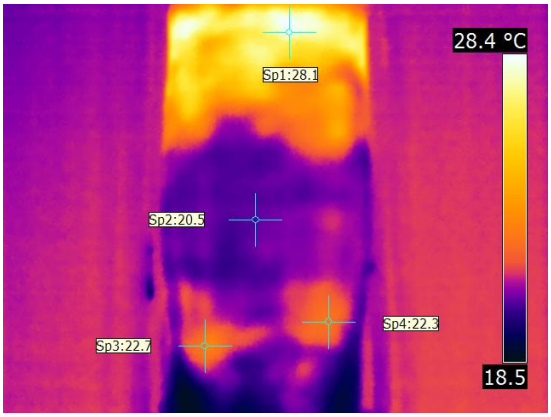

(a) Heating begins. Sp1 indicates wall loss, Sp2 joint area and Sp3-Sp4 minor wall losses.

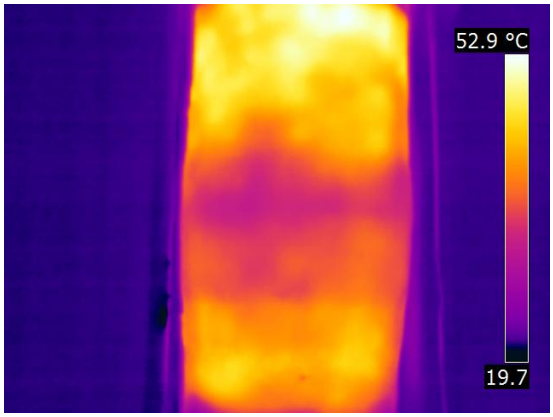

(b) Heating continued. Joint is seen as colder area in the middle of the pipe.

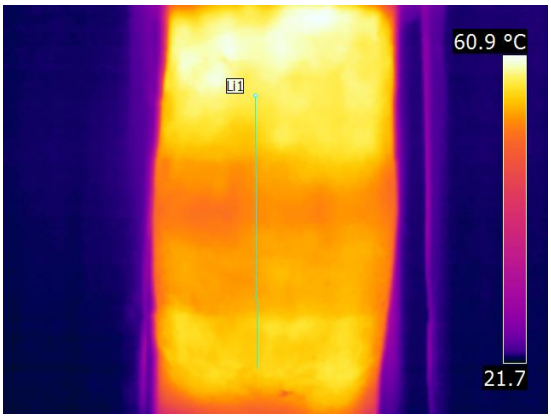

(c) Infrared profile measurement over joint in stabilized process.

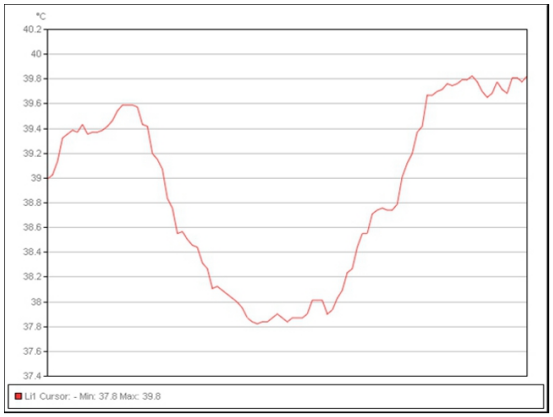

(d) Infrared profile of Li1.

Figure B.20: IRT of U_GRP_3. All detected defects and joint area.

IRT of U_GRP_4 is shown in Figure B.21 (see p. 95). Wall loss and delamination is detected. Colder, continuous vertical line over the whole length of the left side of the pipe might be a manufacturing defect.

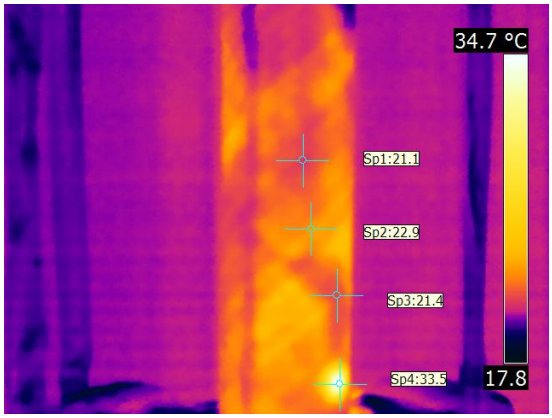

(a) Heating begins. Sp1 and Sp3 are indications of delamination. Sp4 indicates the wall loss area. Sp2 is the reference temperature.

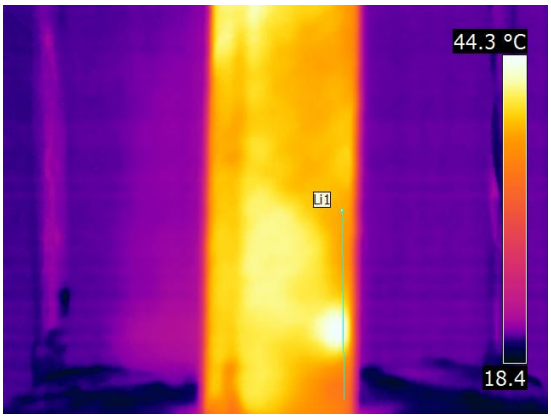

(b) Heating continued. Infrared profile is taken along line Li1 where wall loss occurs.

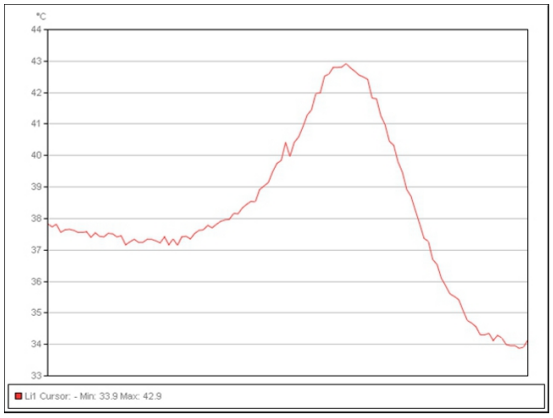

(c) Infrared profile of Li1.

(d) Indication of major cracks are seen under measurement points Sp2 and Sp3. Sp1 is the reference temperature of the defectless area.

Figure B.21: IRT of U_GRP_4. All detected defects and joint area.

IRT of U_GRP_5 is shown in Figure B.22. Wall loss and major cracks are detected.

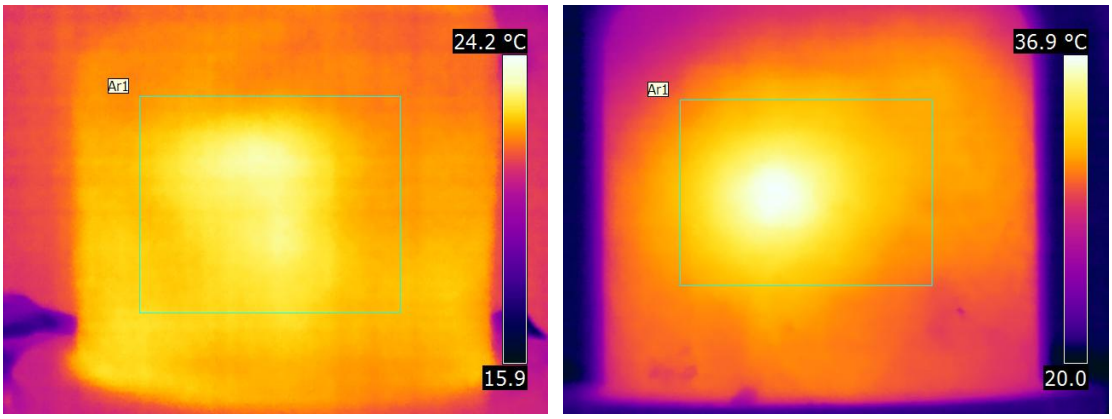

(a) Major cracks are seen as warmer areas inside the rectangle Ar1. Maximum temperature inside Ar1 is 23,5 °C and minimum is 21,9 °C.

(b) Wall loss is seen as warmer areas inside the rectangle Ar1. Maximum temperature inside Ar1 is 39,9 °C and minimum is 29,8 °C.

Figure B.22: IRT of U_GRP_5. Major cracks and wall loss.

C Phased Array Ultrasonic Testing Image Bank

The main problem of attenuation can be overcome by choosing a proper delay line for the phased array probe (see Section 5.7). Figure C.1 (see p. 97) illustrates the delay line echo.

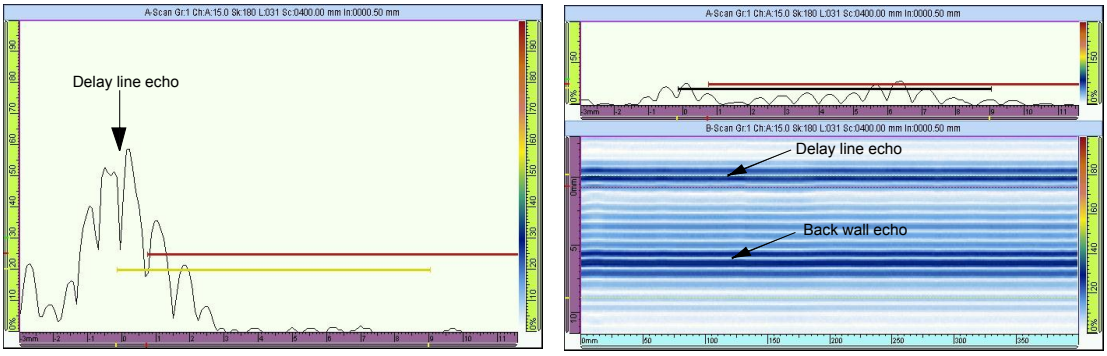

(a) Delay line echo when the probe is held in midair.

(b) Delay line echo and back wall echo when the probe is contacted to GRP .

Figure C.1: PAUT delay line.

A-, B-, C- and S-scans (see Section 5.6 on p. 34) were found informative when analysing the data.

C.1 Calibration Plates

Testing of step plate R_GRP_1_B_S4 (see Subfigure 8.1e on p. 54) is shown in Figure C.2.

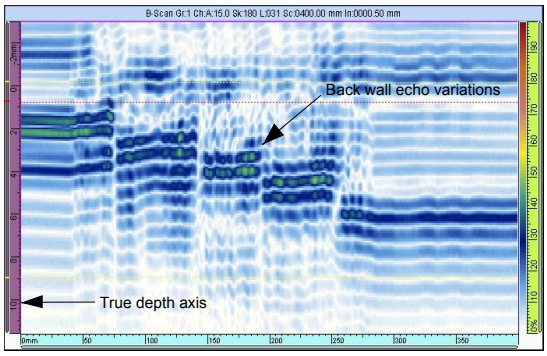

Figure C.2: PAUT of R_GRP_1_B_S4 step plate. B-scan of gradual wall losses.

Testing of the R_GRP_1_B_S3 resolution plate (similar to Subfigure 8.1d on p. 54) is shown in Figure C.3. The S-scan was found to be best for the detection of small flat-bottom bores. Even a flat-bottom bore 1 mm in diameter could be detected as the weakening of the back wall echo.

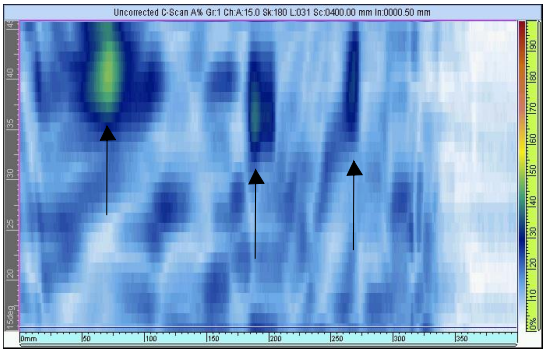

(a) C-scan. Flat-bottom bores 3 mm in diameter in different depths.

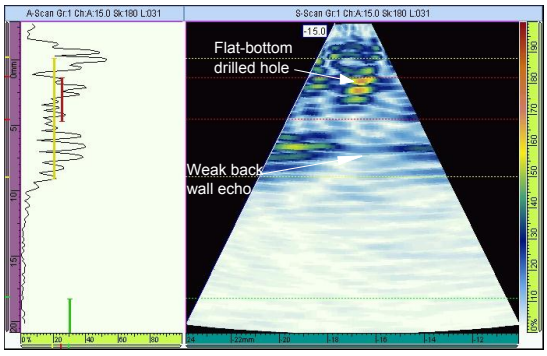

(b) Multiview: A- and S-Scans. Flat-bottom bores 3 mm in diameter 2 mm below surface.

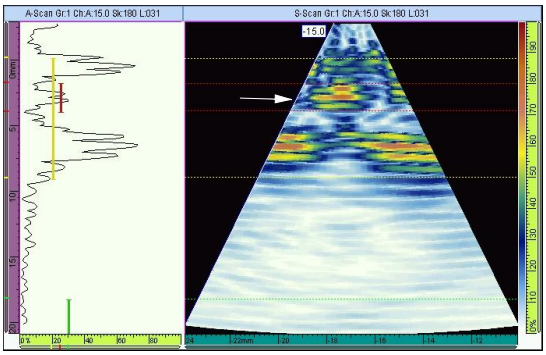

(c) Multiview: A- and S-Scans. Flat-bottom bores 2 mm in diameter 3 mm below surface.

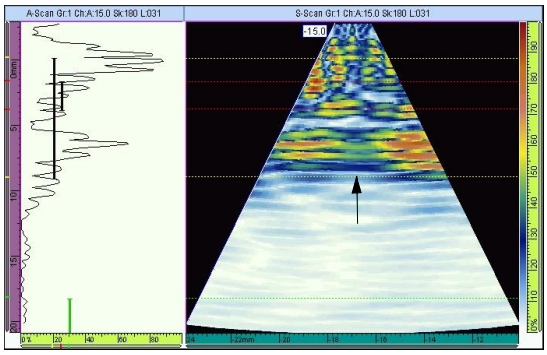

(d) Multiview: A- and S-Scans. Flat-bottom bores 1 mm in diameter 2 mm below surface. The weakening of the back wall echo.

Figure C.3: PAUT of R_GRP_1_B_S3 resolution plate.

C.2 Plates

Gradual wall loss is shown in Figure C.4 (see p. 99). The B-scan is more informative.

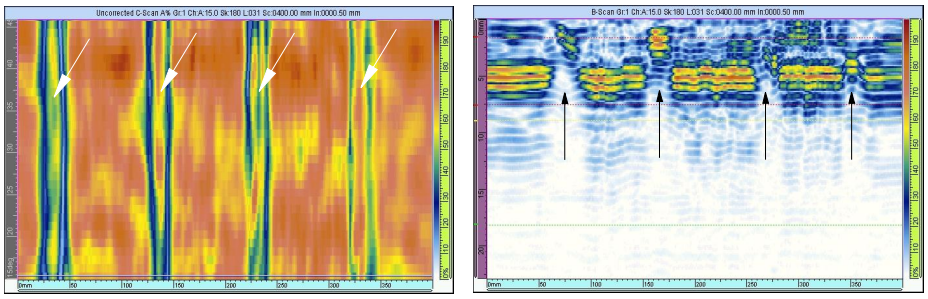

(a) C-scan. (b) B-scan.

Figure C.4: PAUT of P_GRP_1_B plate. Gradual wall loss.

Delamination is shown in Figure C.5.

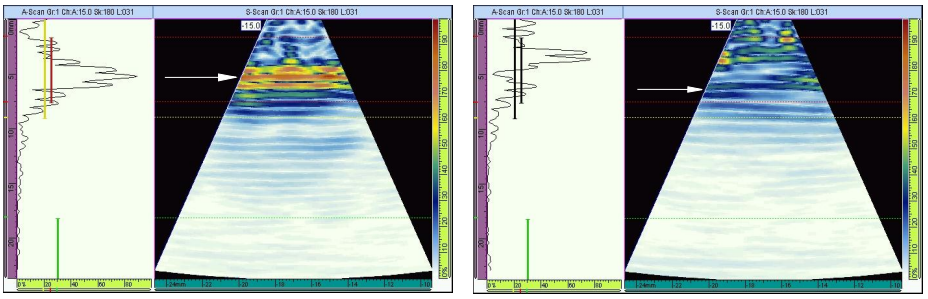

(a) S-scan. Reference back wall echo from the defectless area.

(b) S-scan. Loss of back wall echo energy due to delamination.

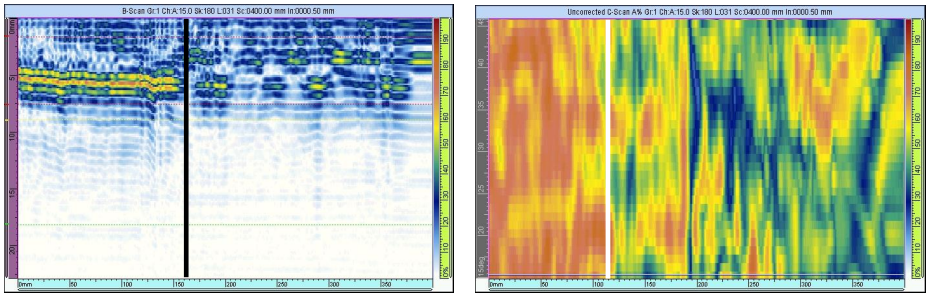

(c) B-scan. Defectless area are is on the left side of the black line and delaminated area is on the right side.

(d) C-scan. Defectless area are is on the left side of the white line and delaminated area is on the right side.

Figure C.5: PAUT of P_GRP_1_B plate. Delamination.

C.3 Empty Pipes

Delamination due to impact damage is shown in Figure C.6.

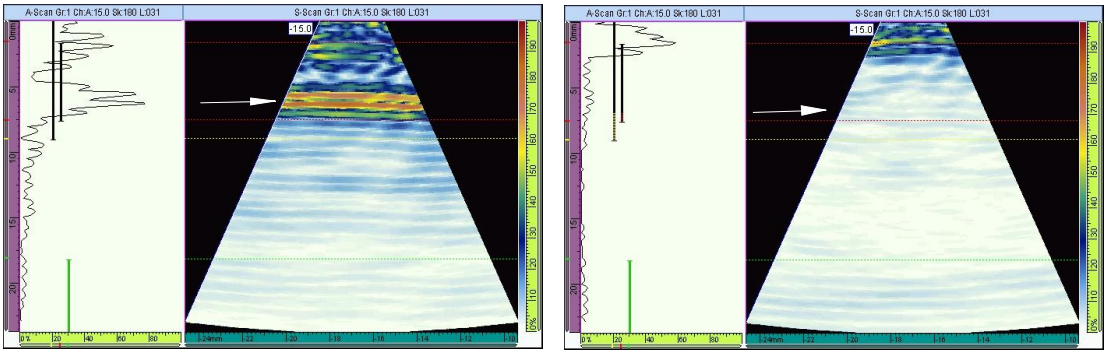

(a) S-scan. Reference back wall echo from the defectless area.

(b) S-scan. Impact damage. Loss of back wall echo energy due to delamination.

Figure C.6: PAUT of N_GRP_1. Delamination caused by an impact damage.

The reference back wall echo, wall loss and delamination due to impact damage are shown in Figure C.9.

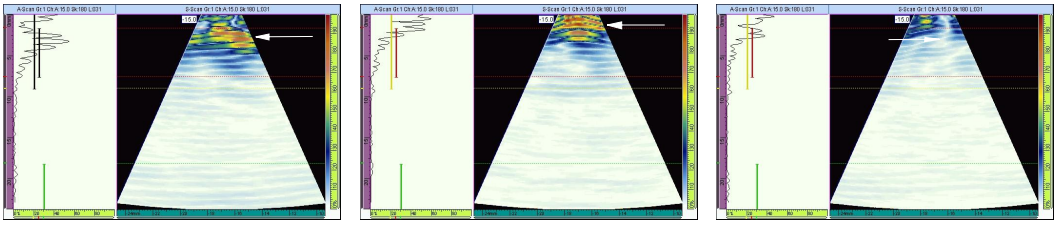

(a) S-scan. Reference back wall echo from the defectless area.

(b) S-scan. Wall loss.

(c) S-scan. Impact damage. Loss of back wall echo energy due to delamination.

Figure C.7: PAUT of U_GRP_2. Wall loss and delamination.

C.4 Pipes Filled with Water

The GRP–water -interface causes a portion of the ultrasound to transfer to water. Therefore, the back wall echo is weaker but detectable when the pipes are filled with water (see Figures D.6 and D.7).

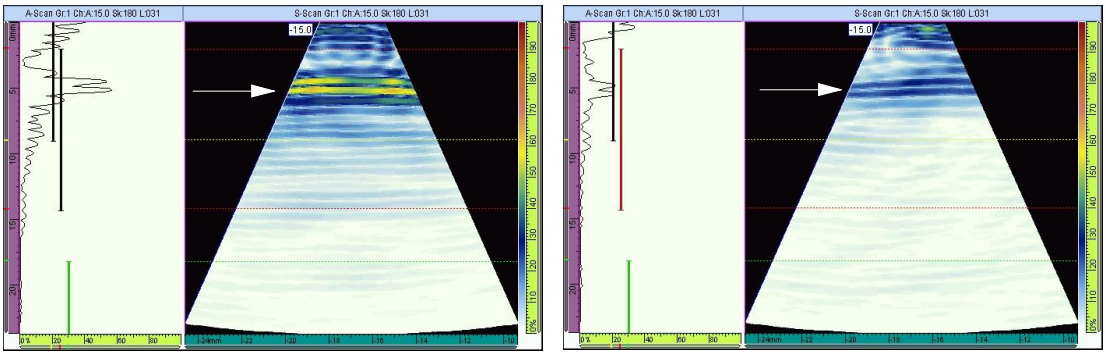

(a) S-scan. Reference back wall echo from the empty pipe.

(b) S-scan. The effect of water.

Figure C.8: PAUT of N_GRP_2 pipe filled with water.

For small wall thickness, near field effect to disturbs the back wall echo (see Subfigure C.9b).

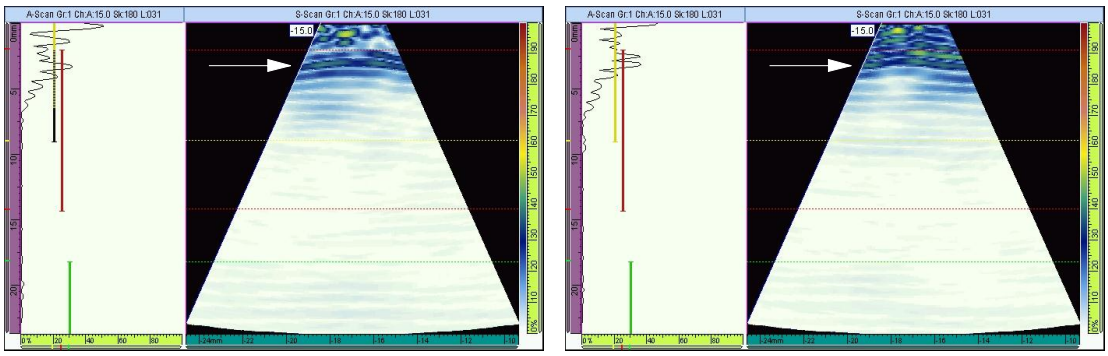

(a) S-scan. Reference back wall echo from the empty pipe.

(b) S-scan. The effect of water.

Figure C.9: PAUT of U_GRP_2 pipe filled with water. The effect of water to the back wall echo.

D Zero Interface Probe Ultrasonic Testing Image Bank

Section 6.2 covers the theory of zero interface probe ultrasonic testing (ZIP UT). The ZIPs contain a delay line that is acoustically matched to most composites. The ZIPs are highly damped for high resolution and sharp A-scan image. Moreover, the characteristics of the ZIPs include high penetration due to low frequency and very high near surface resolution (GE , 2008). Delay line echo is larger for small diameter (<100 mm) pipes compared to plates because of inferior contact due to cylindrical surface geometry.

Surface roughness of the A-side of the testing blocks varied between 2,00 μm and 13,87 μm. Surface roughness of the B-side varied from 0,65 μm to 1,42 μm. This indicates that the zero interface probe ultrasonic testing should be carried out from the B-side for plates when ever possible. However, good results were obtained from both surface sides.

D.1 Calibration Plates

Testing of R_GRP_1_B_S2 (see Subfigure 8.1d on p. 54) proved that the resolution for ZIP used is 3 mm. Consequently, smaller diameter flat-bottom bores could not be detected.

The testing of step plate R_GRP_1_B_S4 (see Subfigure 8.1e on p. 54) is shown in Figure D.1 (see p. 103). When comparing Figures D.1 and 6.1, it is clear that ZIP is well acoustically matched to GRP because the delay line echo is almost non-existant when the probe is contacted to GRP. As a result, only a small amount of ultrasonic energy is reflected from the interface. Figure D.1 shows how the back wall echo is gradually moving to the left, meaning a thinning of the target in 1 mm steps. The barrier layer is detected in Subfigures D.1a and D.1b.

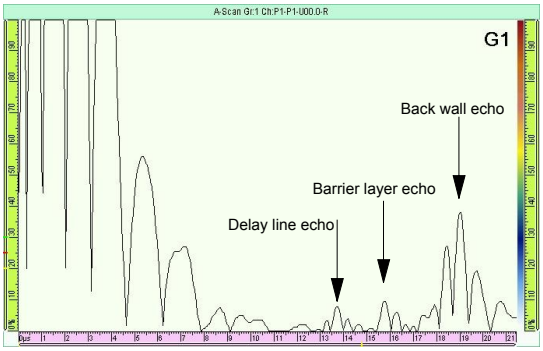

(a) Thickness of 6,5 mm.

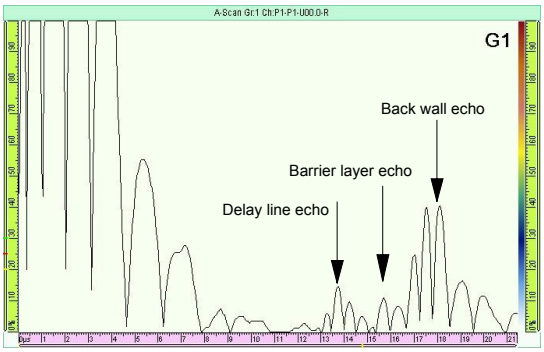

(b) Thickness of 5 mm.

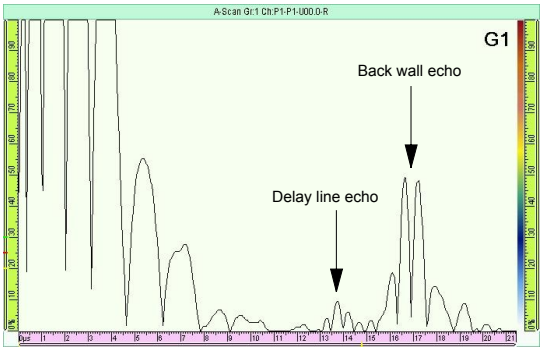

(c) Thickness of 4 mm.

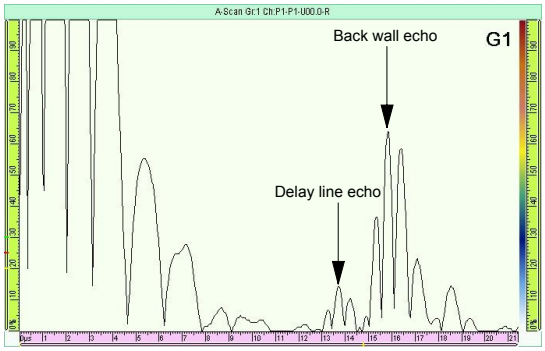

(d) Thickness of 3 mm.

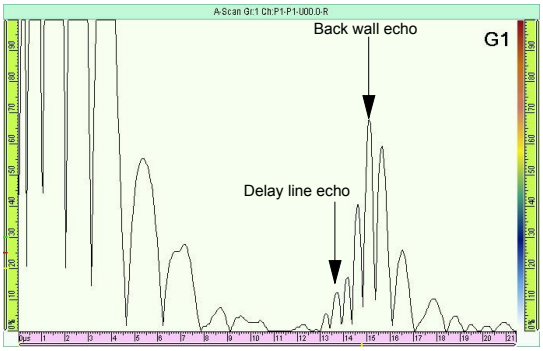

(e) Thickness of 2 mm.

Figure D.1: ZIP UT of R_GRP_1_B_S4.

D.2 Plates

Gradual thinning in plate P_GRP_1_B (see Subfigure 8.2a on p. 55) is shown in Figure D.2.

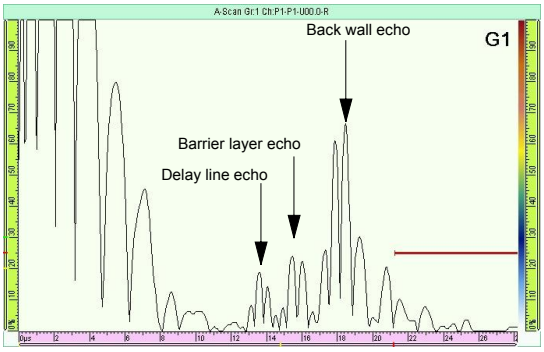

(a) Nominal thickness.

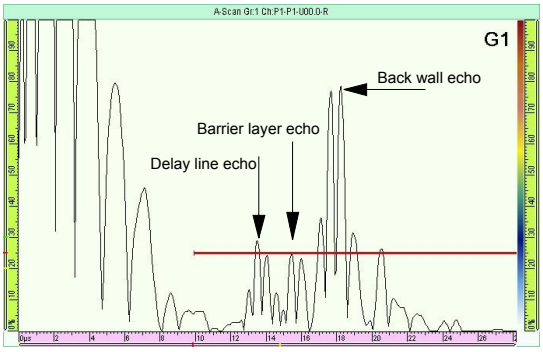

(b) The smallest thinning and the smallest displacement of the back wall echo towards delay line echo.

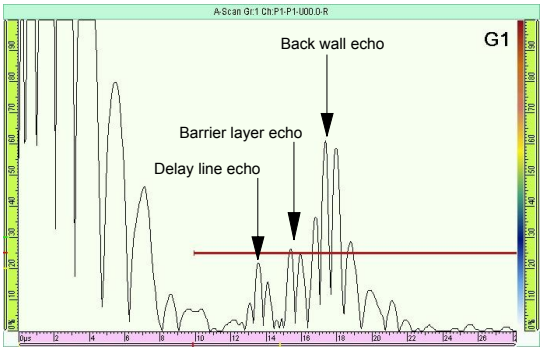

(c) 2 nd gradual thinning.

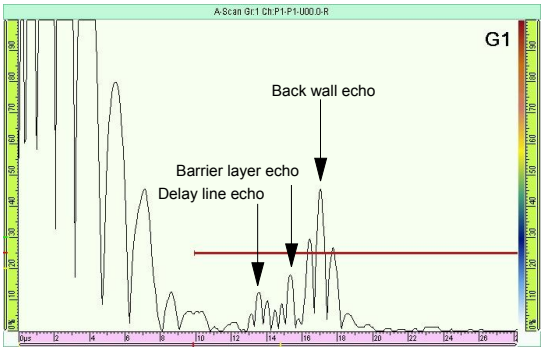

(d) 3 rd gradual thinning.

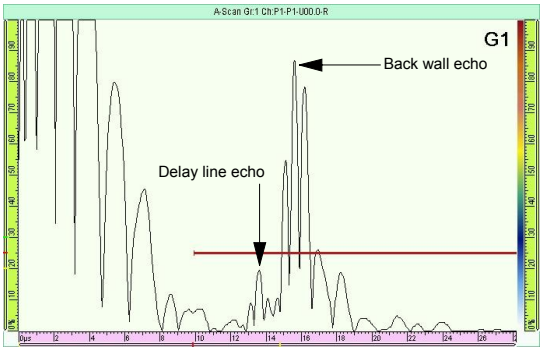

(e) 4 th gradual thinning.

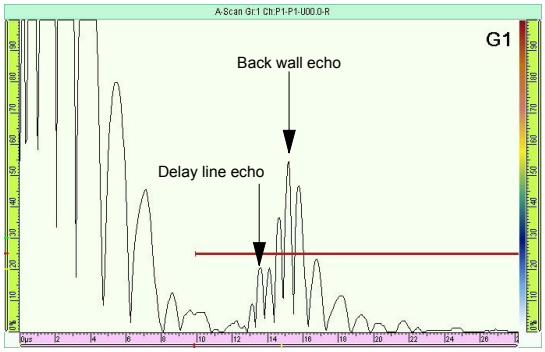

(f) The largest thinning and the greatest displacement of the back wall echo towards delay line echo.

Figure D.2: ZIP UT of P_GRP_1_B. Gradual thinning and barrier layer.

Delamination and the impact damage effect in plate P_GRP_1_B (see Subfigure 8.2a

on p. 55) are shown in Figure D.3.

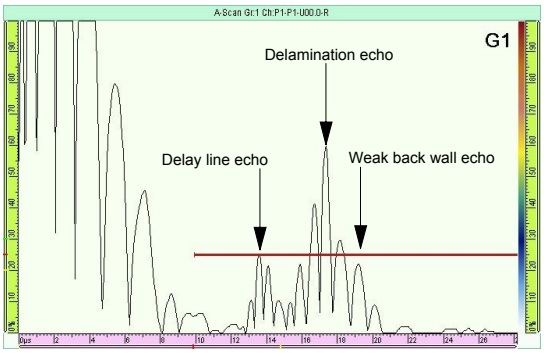

(a) Delamination.

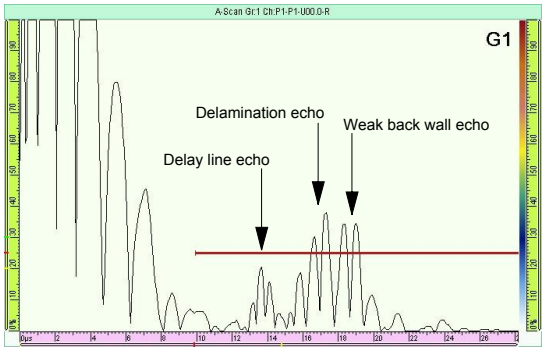

(b) Delamination.

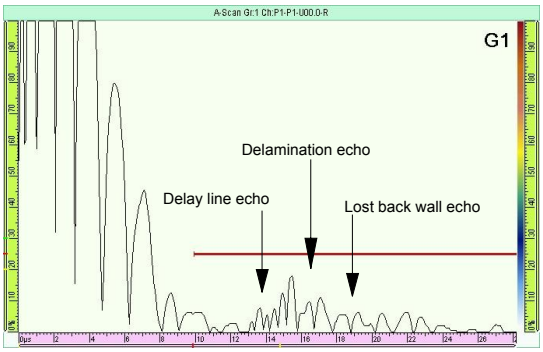

(c) Delamination caused by impact damage.

Figure D.3: ZIP UT of P_GRP_1_B. Delamination and impact damage.

D.3 Empty Pipes

Impact damages are detected only when they cause delamination. Delamination is usually detected as multiple echoes after the delay line echo and lost back wall echo. Impact damage in N_GRP_1 is shown in Figure D.4 (see p. 106).

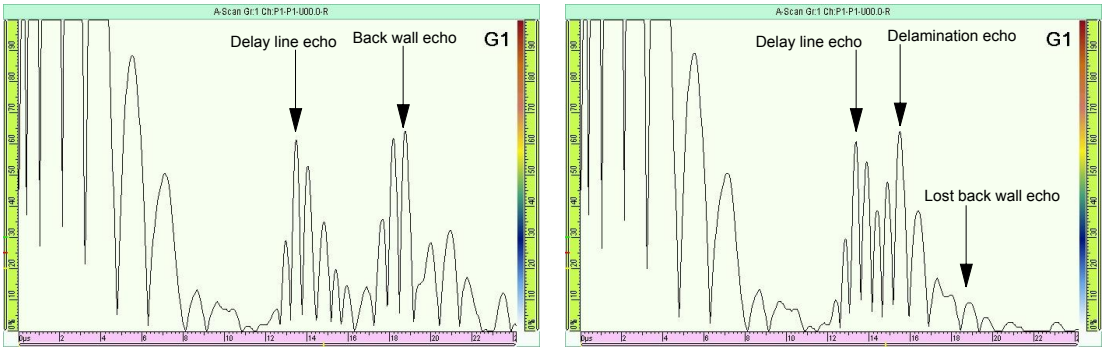

(a) Reference image next to the impact damage. (b) Delamination caused by an impact damage.

Figure D.4: ZIP UT of N_GRP_1. Impact damage.

Wall loss, impact damage and delamination in U_GRP_2 are shown in Figure D.5.

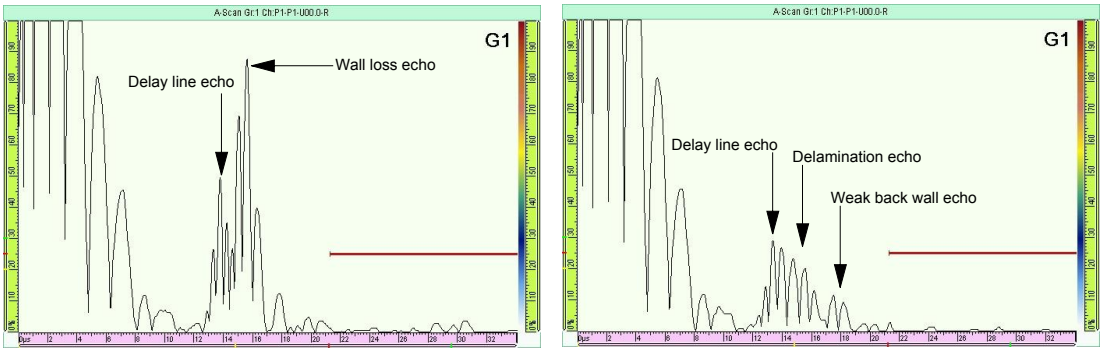

(a) Wall loss. (b) Impact damage.

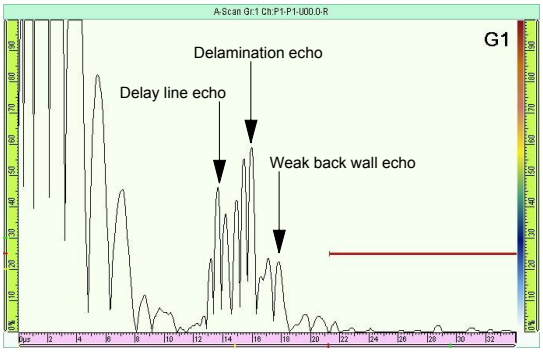

(c) Delamination.

Figure D.5: ZIP UT of U_GRP_2.

D.4 Pipes Filled with Water

A portion of ultrasonic energy is transferred to water in the GRP–water -interface because the acoustic impedance of water is non-zero. Therefore, the back wall echo is weaker but detectable when the pipes are filled with water (see Figures D.6 and D.7).

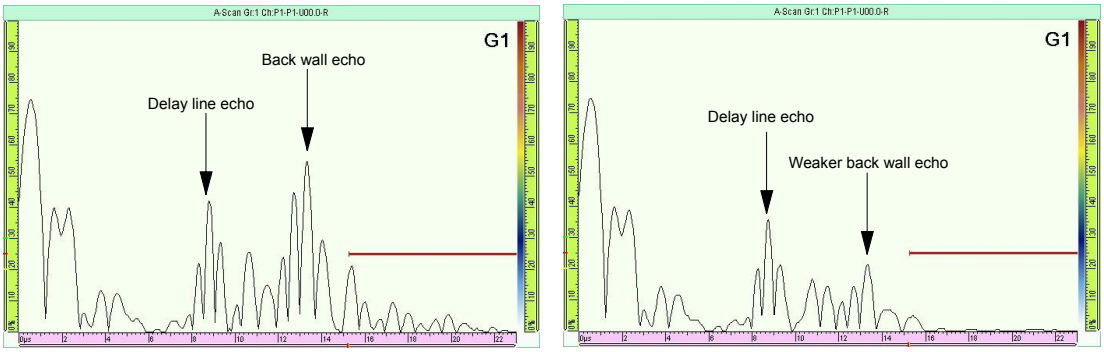

(a) Reference image from the empty pipe.

(b) Pipe filled with water.

Figure D.6: ZIP UT of N_GRP_2 filled with water.

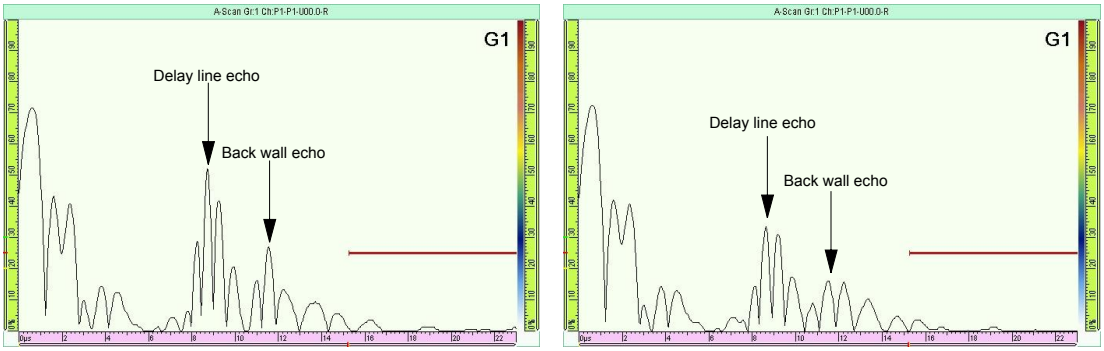

(a) Wall loss.

(b) Impact damage.

Figure D.7: ZIP UT of U_GRP_2 filled with water.

E Digital Radiographic Testing Image Bank

As stated in Chapter 7, digital image processing offers special features for digital radiographic testing. DRT is the best technique to visualize the fiber orientation which can be seen from the Figures of this Appendix.

E.1 Calibration Plates

Figure E.1a (see p. 108) is an unprocessed DRT image. Thinner flat-bottom bores are seen as lighter areas. Figure E.1b (see p. 108) is the countour analysis of the surface. In special cases contour analysis can give valuable information about the type and orientation of the defect.

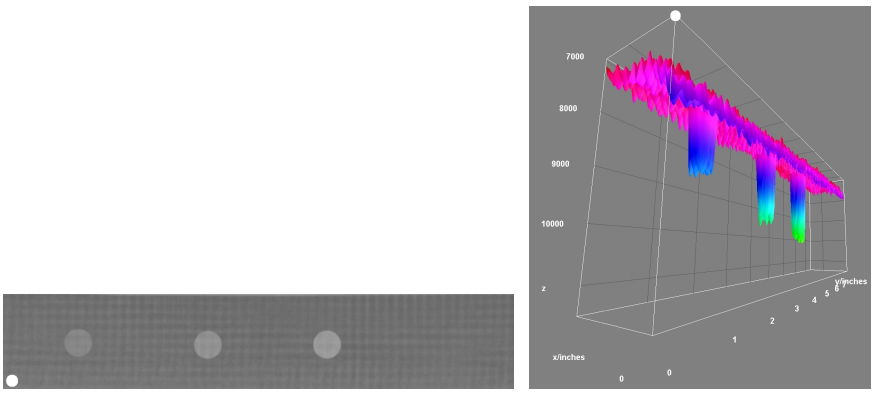

(a) Calibration plate 1. (b) Contour analysis.

Figure E.1: DRT of R_GRP_1_S1. The white spot marks the origin in the (x,y)-plane.

Advantages of image processing are clear when comparing Figures E.2a and E.2b. Flat-bottom bores and fiber orientations are more visible in darker and sharper Figure E.2b. The smallest bore of 1 mm in diameter and 1 mm in depth is still visible. Thus, it is considered the resolution for the DRT.

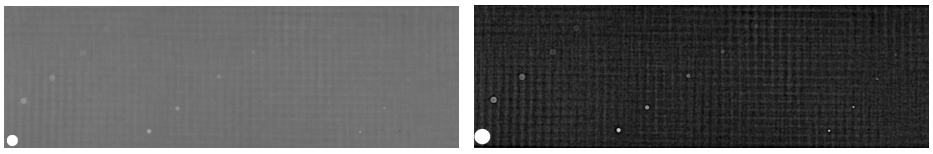

(a) Calibration plate 2. (b) Darker and sharpener DRT calibration plate 2 in order to get flat bottom bores more visible.

Figure E.2: DRT of R_GRP_1_S2.

The step plate and its contour analysis are shown in Figure E.3. The plate is thinning in 1 mm steps toward lighter and greener areas.

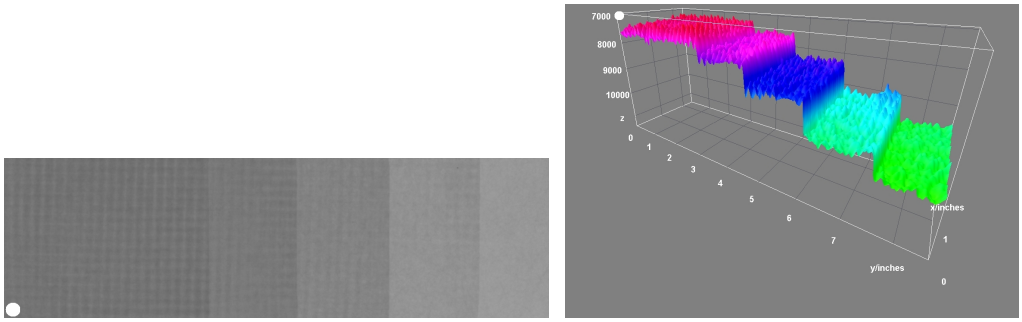

(a) DRT calibration plate 4. (b) Contour analysis.

Figure E.3: DRT of R_GRP_1_S4. The white spot marks the origin in the (x,y)-plane.

E.2 Plates

Major cracks, wall losses and fiber orientation are shown from in Figure E.4 but impact damages are not detected. Even the smallest scratches are detected.

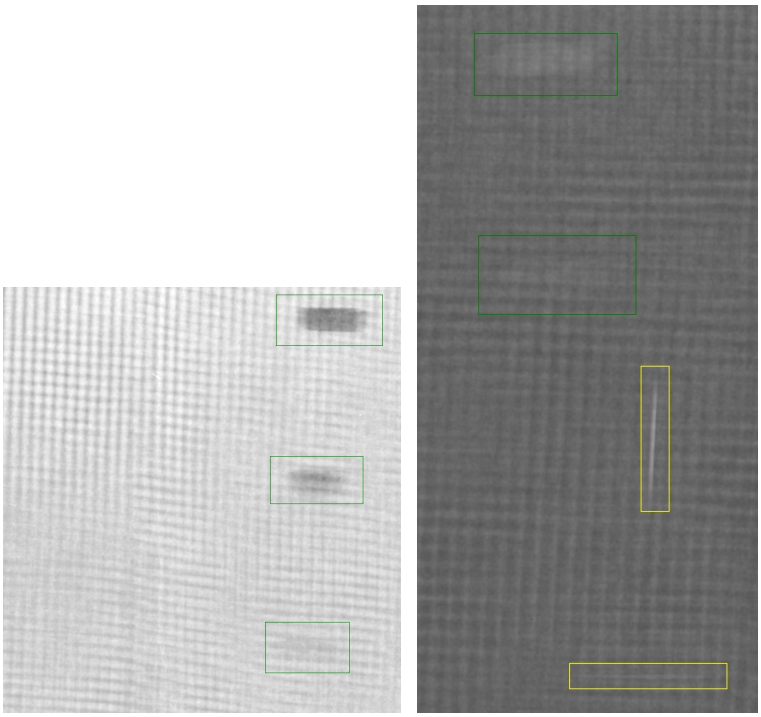

(a) Wall losses. (b) Wall losses and cracks.

Figure E.4: DRT of P_N_GRP_1.

E.3 Empty Pipes

The figure E.5 deals with delamination and wall loss. As stated in Section 9.5 (see p. 63) delamination is only visible in profile figure. Subfigures E.5a and E.5b illustrates the position of the defects. Subfigures E.5c and E.5d are zoomed images of the defects for more illustrative example data. Also, zoomed image about defectless profile is presented in Subfigure E.5e for reference.

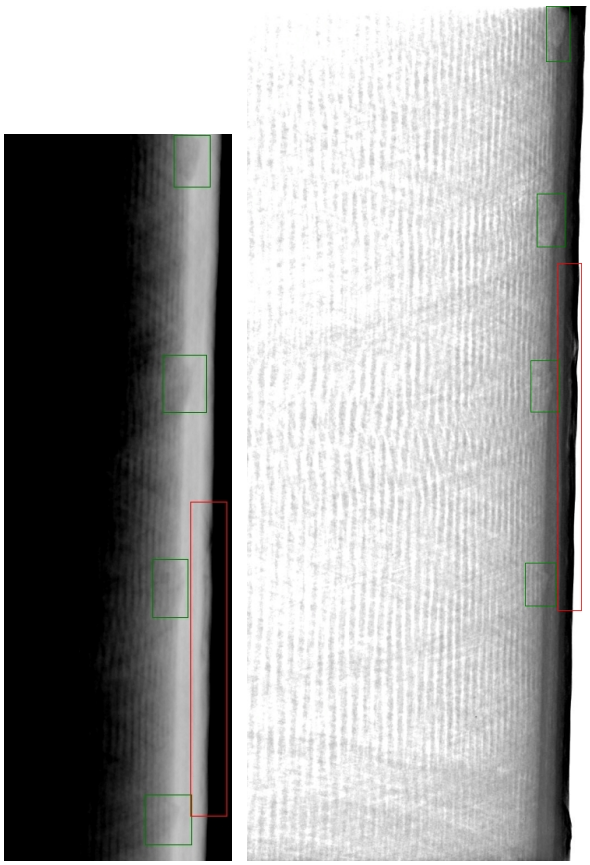

(a) Wall loss and delamination.

(b) Wall loss and delamination.

Figure E.5: DRT of N_GRP_1. Wall loss and delamination (*continued on the next page*).

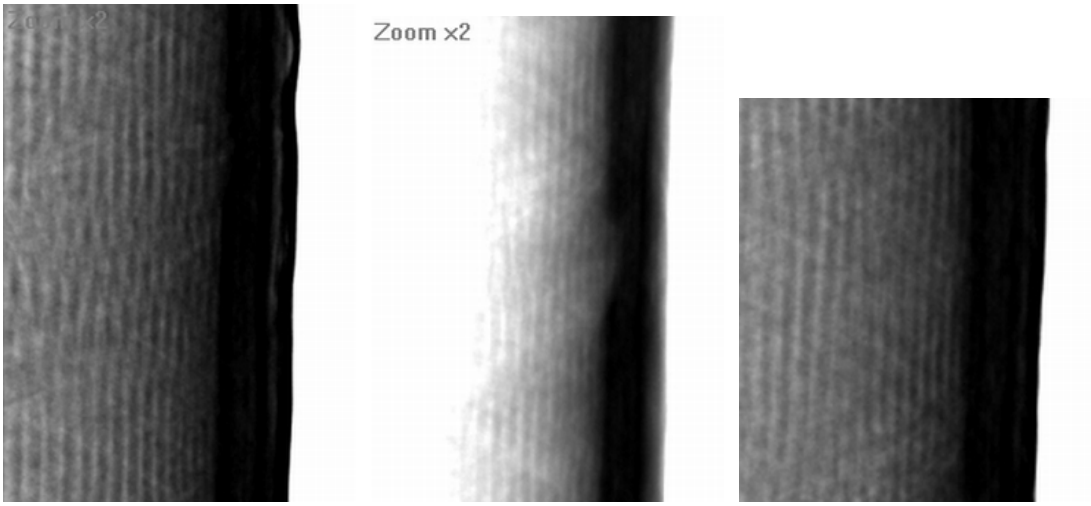

(c) Zoomed delamination. (d) Zoomed wall loss in the profile. (e) Zoomed defectless profile.

Figure E.5: DRT of N_GRP_1. Wall loss and delamination.

Figure E.6 illustrates a major crack and minor delamination.

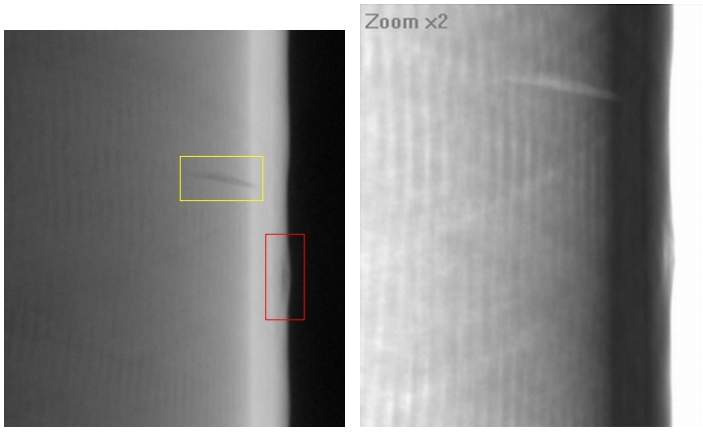

(a) Major crack and minor delamination. (b) Zoomed defects.

Figure E.6: DRT of N_GRP_1. Major crack and minor delamination.

Figure E.7 deals with delamination and wall loss in shell figure.

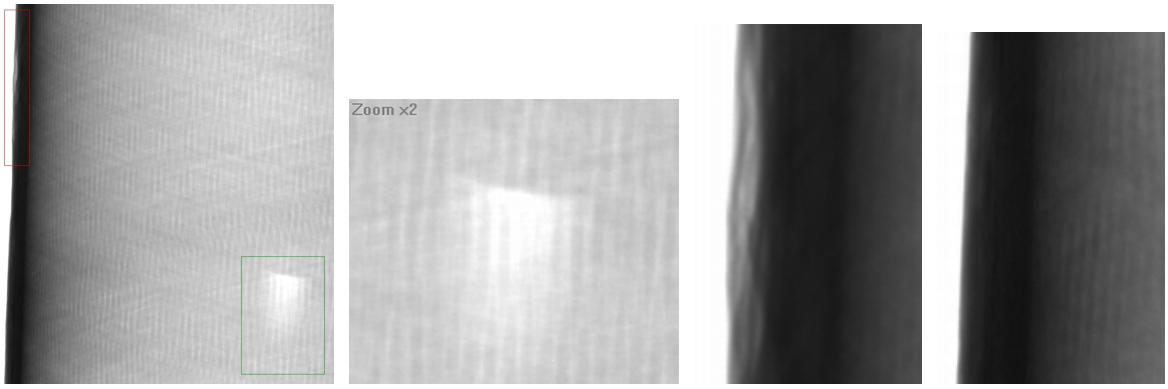

(a) Wall loss and delamination.

(b) Zoomed wall loss in the shell figure.

(c) Zoomed delamination.

(d) Zoomed defectless profile.

Figure E.7: DRT of N_GRP_1. Wall loss in shell and delamination. Defectless profile is presented for reference.

Gradual wall loss, major cracks and fiber orientation are shown in Figure E.8. 2 mm of tin do not disturb the visibility. However, usually it is better to test pipes without tin.

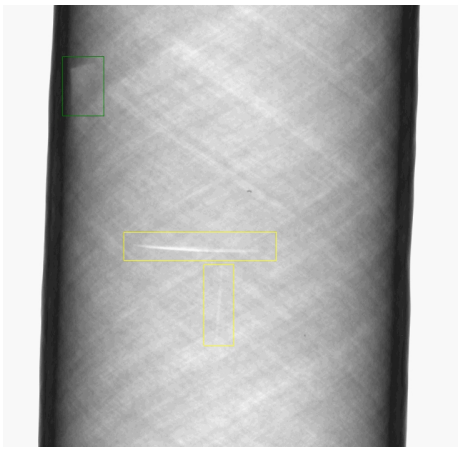

Figure E.8: DRT of N_GRP_2 pipe. Gradual wall loss and major cracks. 2 mm of tin.

Digital radiographic testing procedure is similar to pipes removed from service. Major cracks and wall loss are shown in Subfigures E.9a and E.9b. Delamination is shown in Subfigure E.9c (see p. 113).

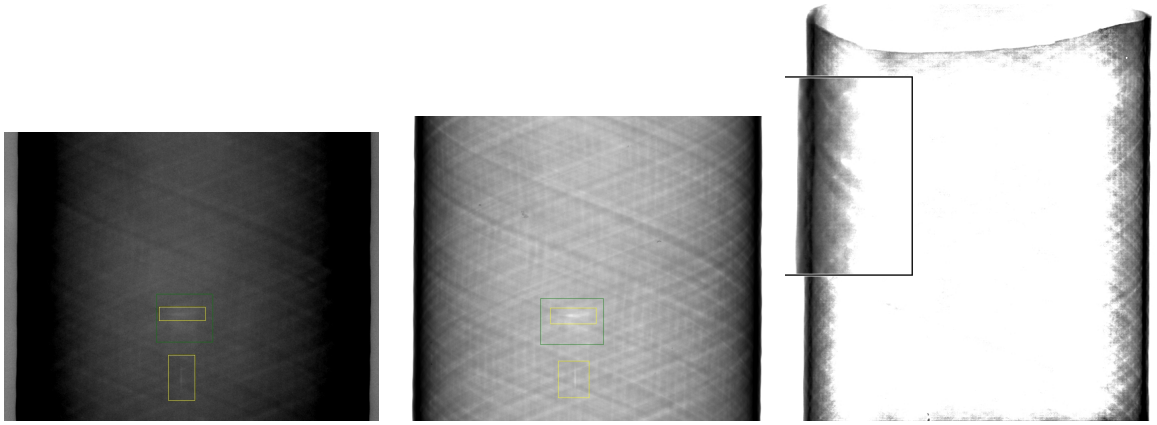

(a) Wall loss and major cracks when using 2 mm of tin.

(b) Wall loss and major cracks.

(c) Delamination in the zoomed pipe profile.

Figure E.9: DRT of U_GRP_2 pipe. Wall loss, major cracks and delamination.

Major cracks and wall loss of a small diameter pipe are shown in Figure E.10.

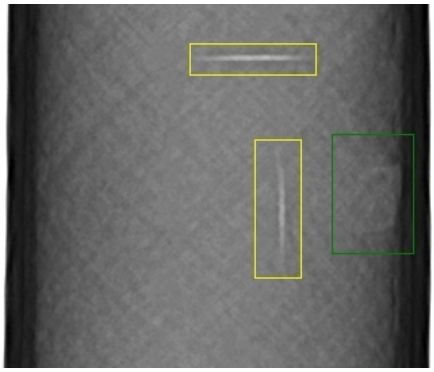

Figure E.10: DRT of U_GRP_4 pipe. Wall loss and major cracks.

E.4 Pipes Filled with Water

Wall losses are not detected in the shell of the pipe in Subfigure E.11a. Wall loss is not visible even in the pipe profile in Subfigure E.11b.

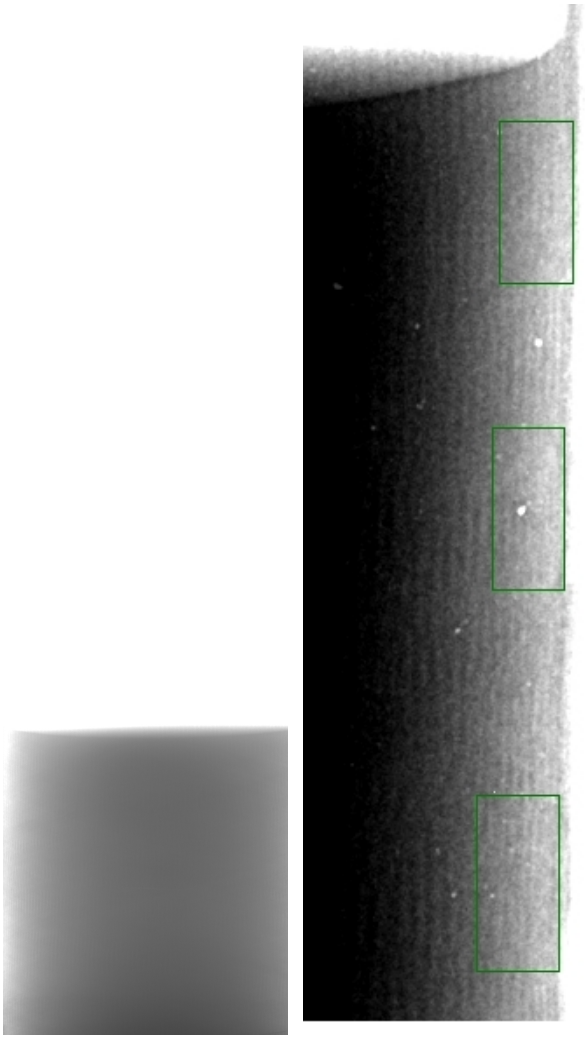

(a) No visible wall loss in the pipe shell when filled with water.

(b) Wall loss is barely visible in the pipe profile.

Figure E.11: N_GRP_1 pipe filled with water. Wall losses are not detected.

Figure E.12 offers an insight to the effect of tin to the test results. Subfigure E.12a is clearly the best of the three figures.

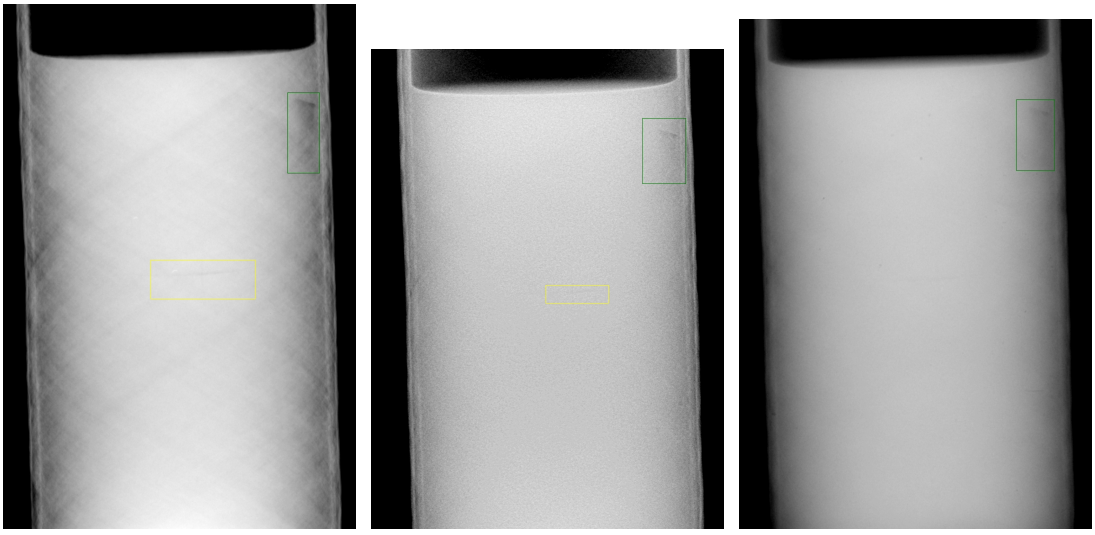

(a) Crack and wall loss.

(b) 2 mm of tin. Crack and wall loss.

(c) 4 mm of tin. Wall loss. Crack is not visible.

Figure E.12: N_GRP_2 pipe filled with water. Tin desturbs the testing.

Wall loss can be detected from the profile in U_GRP_2 pipe. See Figure E.13.

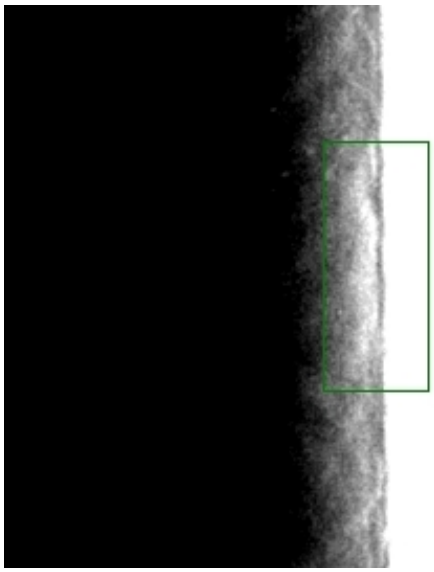

Figure E.13: U_GRP_2. Wall loss in the profile image.

E.5 Testing Parameters

Reference Plates – Testing parameters of reference plates are listed in Table E.1

Table E.1: Reference plates

Thickness T	Exposure time t	Voltage V	Current I
mm	s	kV	mA
6	0,45	65	0,5
6,5	0,45	65	0,5

Plates – Testing parameters of plates are listed in Table E.2

Table E.2: Reference plates

Thickness T	Exposure time t	Voltage V	Current I
mm	s	kV	mA
5,5	0,85	65	0,5

Empty Pipes – Testing parameters of an empty GRP pipes are listed in Table E.3.

Table E.3: Empty GRP pipes

Diameter D	Thickness T	Exposure time t	Voltage V	Current I
mm	mm	s	kV	mA
60	5,5	1,3	75	0,5
80	12	1,3	85	0,5
100	5,5	1,5	70	0,5
150	4,3	1,5	65	0,5
200	6,5	1,25	80	0,5

Pipes Filled with Water – Testing parameters of GRP pipes filled with water are listed in Table E.4.

Table E.4: GRP pipes filled with water

Diameter D	Thickness T	Exposure time t	Voltage V	Current I
mm	mm	s	kV	mA
100	5,5	3,15	90	0,5
200	6,5	2,3	120	0,5

E.6 Intensity Profiles

Software can be used to solve the depth and the length of the defects with digital radiographic testing. For this purpose the intensity curve should settle approximately between 30 % and 80 %.

Figure E.14 illustrates how intensity of Figure E.1a (see p. 108) can be used to measure the diameter of the flat-bottom bores.

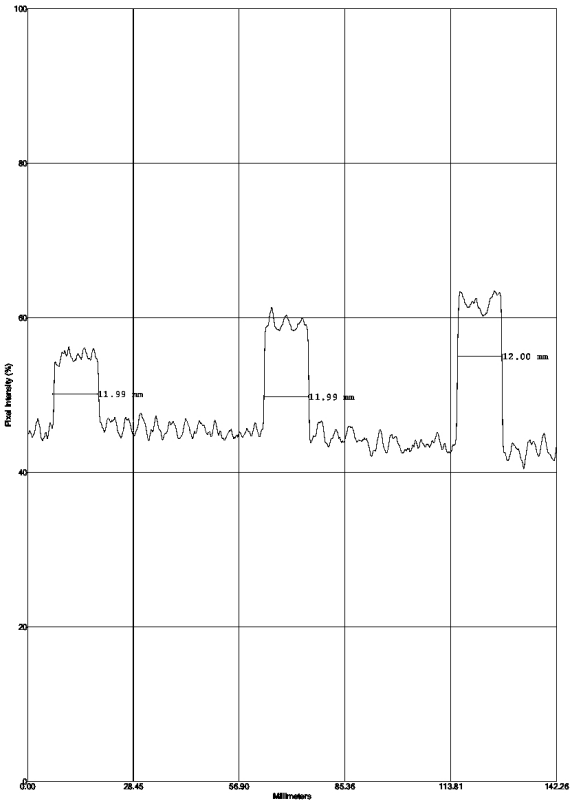

Figure E.14: Measuring the diameter of flat-bottom bores in R_GRP_1S.

The intensity profile gives information of the depth of the defect. The measurement of the change in thickness is shown in Figure E.15.

(a) Change in depth.

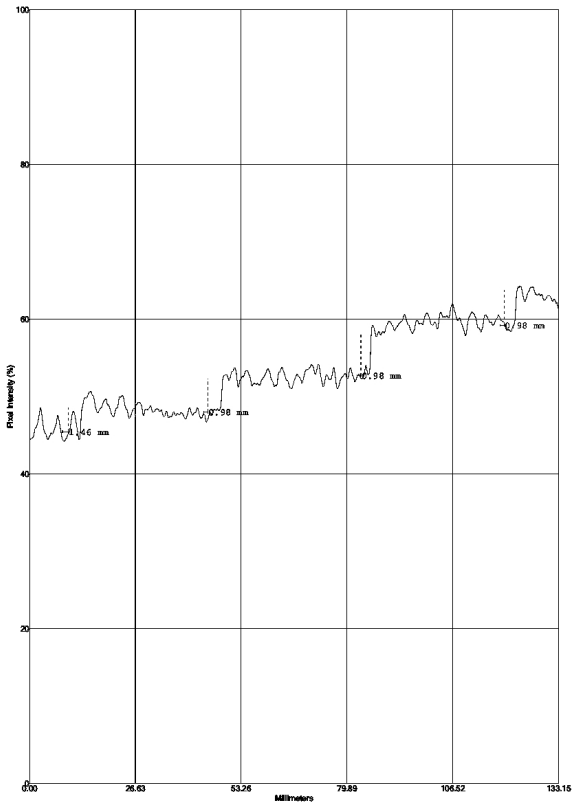

(b) Intensity profile analysis.

Figure E.15: R_GRP_S4.

F Overview

This Appendix summarizes all the inspection results. First, defectless reference images images are presented in Section F.1 in order to demonstrate how the defectless areas are supposed to appear during the analysis of the inspection data. Later on, every Section demonstrates the inspection results of used NDT techniques for certain defect type. Considered defect types are wall loss, delamination, impact damage, major crack and air bubble. They are presented in Sections F.2, F.3, **??**, F.4 and F.5, respectively. Certain NDT techniques cannot detect certain defect types. That emplanes the absence of certain inspection images when considering certain defect types. For example, Section F.4 concerning major crack, presents only the VT and the DRT because with the other NDT techniques the major cracks were not detected or the inspection was not reliable.

F.1 Reference Images

Defectless reference images for all used NDT techniques used are shown in Figure F.1.

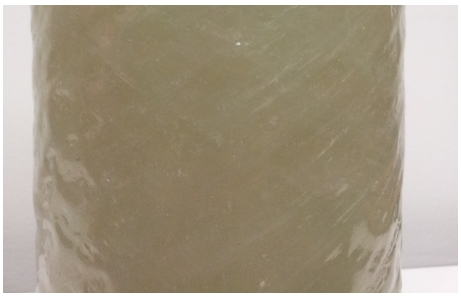

(a) VT. Defectless pipe area.

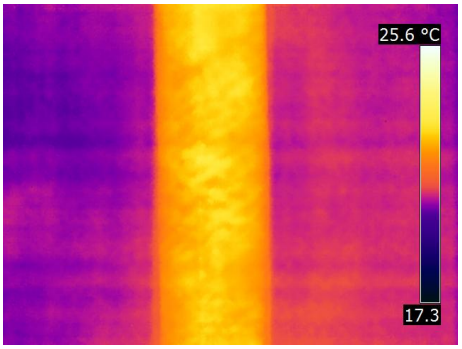

(b) IRT. Reference heating for defectless pipe area.

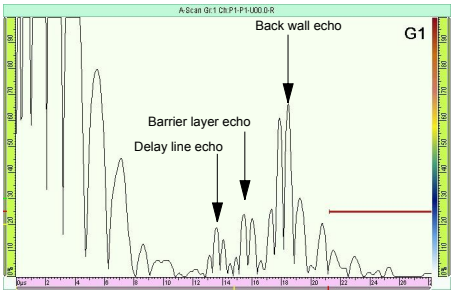

(c) ZIP UT. Nominal thickness.

Figure F.1: Reference images (*continued on the next page*).

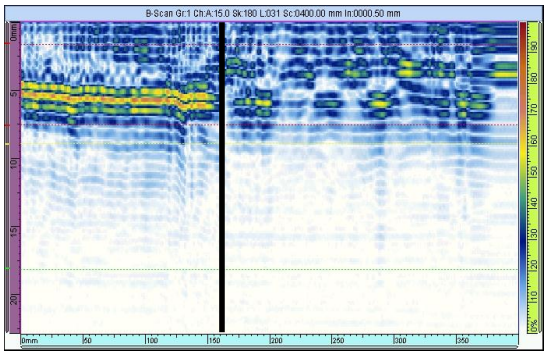

(d) PAUT B-scan. Defectless area are is on the left side of the black line and delaminated area is on the right side.

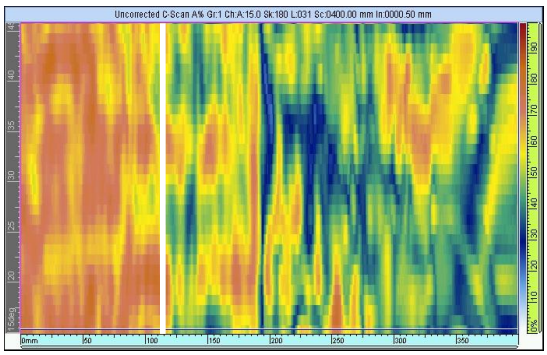

(e) PAUT C-scan. Defectless area are is on the left side of the white line and delaminated area is on the right side.

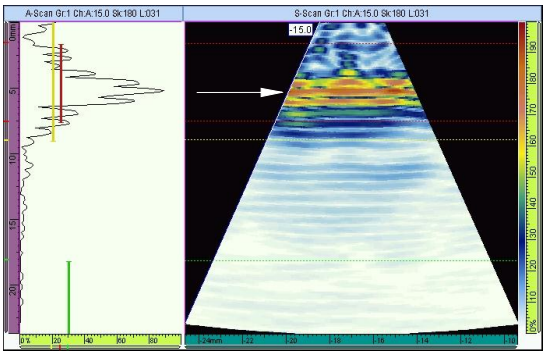

(f) PAUT S-scan. Reference back wall echo from the defectless area.

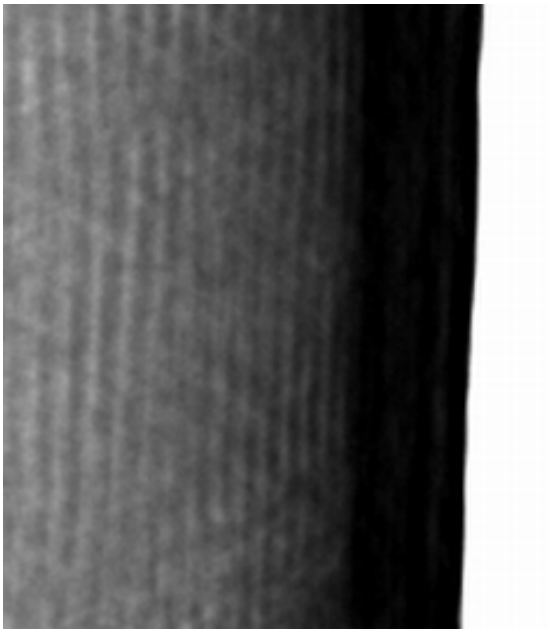

(g) DRT. Zoomed defectless profile.

Figure F.1: Reference images.

F.2 Wall Loss

Wall loss images for all used NDT techniques are shown in Figure F.2.

(a) VT of U_GRPs. Loose fiber in the inner surface.

(b) VT. Even major wall losses are usually very hard to detect from the outer surface.

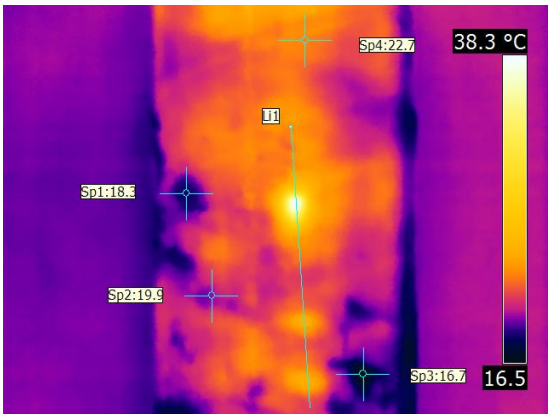

(c) IRT. Li1 is the infrared profile measurement over wall losses.

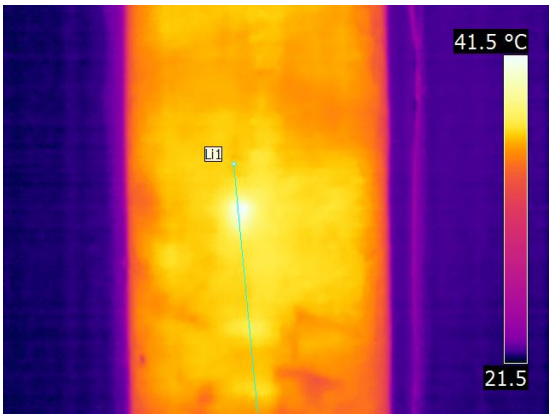

(d) IRT. Three visible wall losses along infrared profile measurement line Li1

Figure F.2: Wall loss (*continued on the next page*).

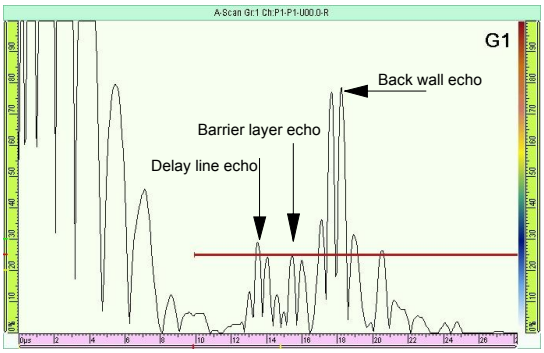

(e) ZIP UT. The smallest thinning and the smallest displacement of the back wall echo towards delay line echo.

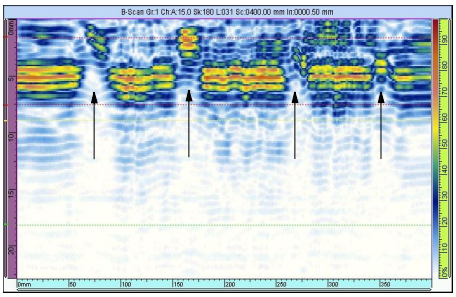

(f) PAUT B-scan. Gradual wall loss.

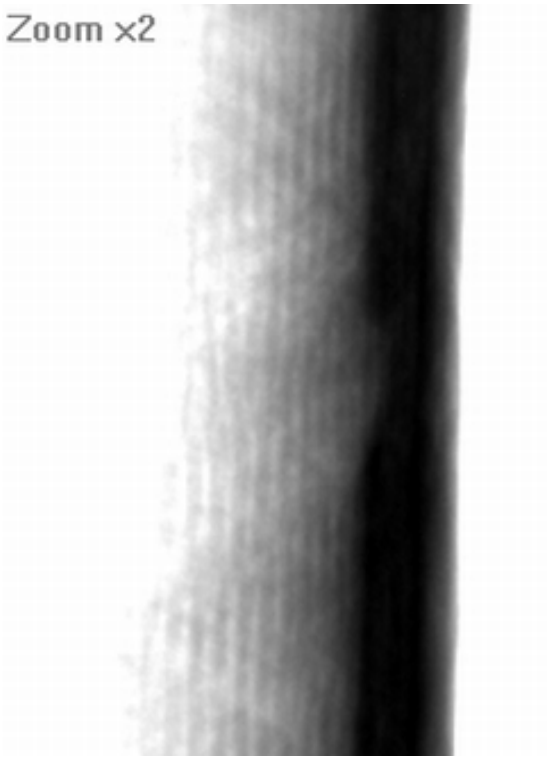

(g) DRT. Zoomed wall loss in the profile.

Figure F.2: Wall loss.

F.3 Delamination

Delamination images for all used NDT techniques used are shown in Figure F.3.

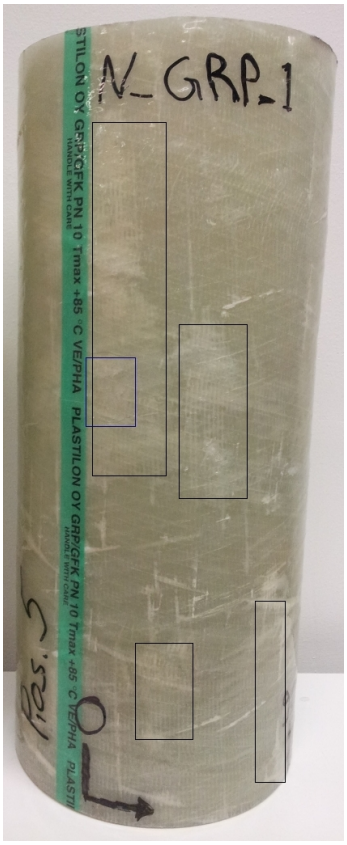

(a) VT. Delamination is seen as the whiter areas inside the black rectancles.

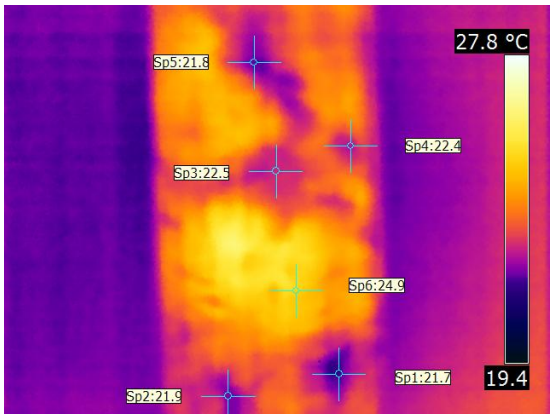

(b) IRT. Delaminations are detected as colder areas Sp1-Sp5. Sp6 is the temperature of the defectless area.

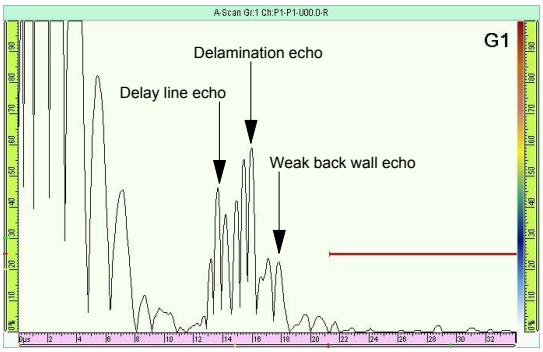

(c) ZIP UT. Delamination.

Figure F.3: Delamination (*continued on the next page*).

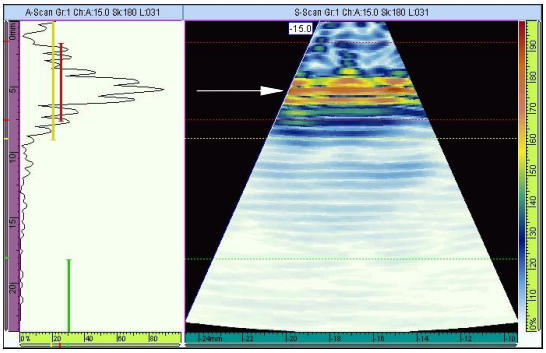

(d) PAUT S-scan. Reference back wall echo from the defectless area.

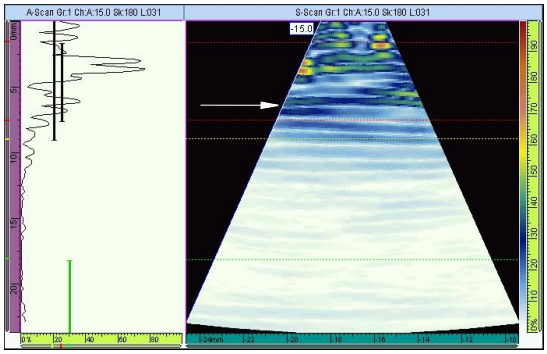

(e) PAUT S-scan. Loss of back wall echo energy due to delamination.

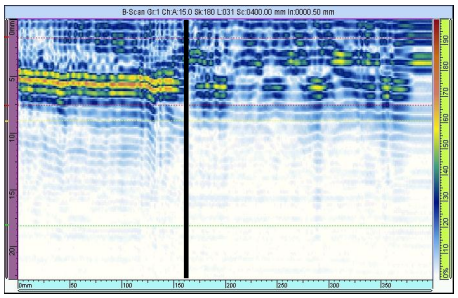

(f) PAUT B-scan. Defectless area are is on the left side of the black line and delaminated area is on the right side.

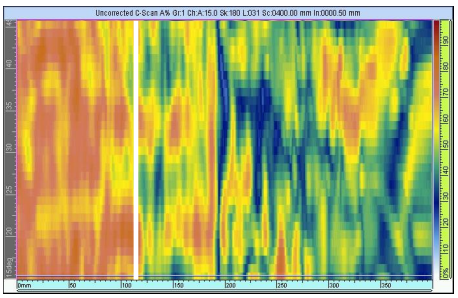

(g) PAUT C-scan. Defectless area are is on the left side of the white line and delaminated area is on the right side.

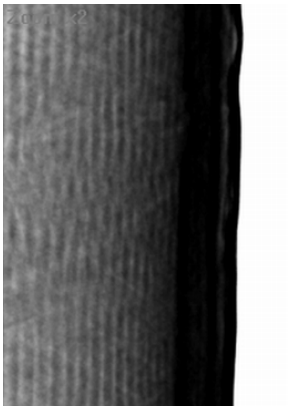

(h) DRT. Zoomed delamination.

(i) DRT. Zoomed delamination.

Figure F.3: Delamination.

F.4 Major Crack

Major crack images for VT and DRT are shown in Figure F.4.

(a) VT. Major crack near the surface.

(b) VT. Cracks are usually very hard to detect from the outer surface.

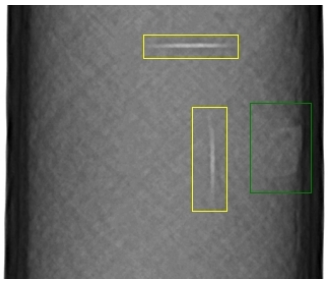

(c) DRT. Wall loss and major cracks.

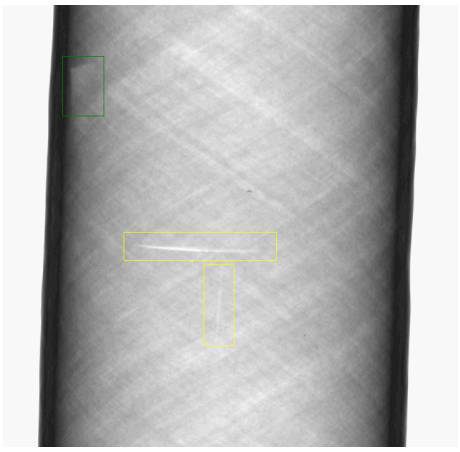

(d) DRT. Gradual wall loss and major cracks.

Figure F.4: Major crack.

F.5 Air Bubble

Air bubbles were not part of the fabricated defects but IRT revealed these manufacturing defect. Air bubble images for VT and IRT techniques are shown in Figure F.5.

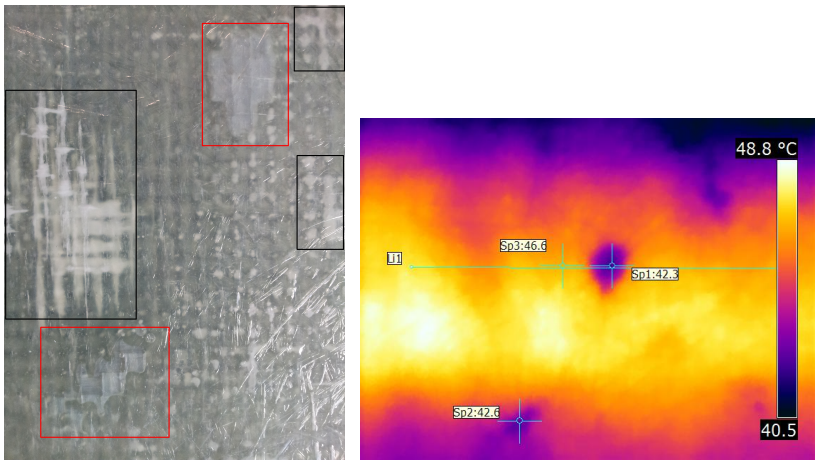

(a) VT. Zoomed air bubbles inside red rectangles and delamination inside black rectangles.

(b) IRT. Air bubbles Sp1 and Sp2. Temperature of a defectless structure is shown in Sp3.

Figure F.5: Air bubbles.